Advancing Assessments on Aerosol Radiative Effect by Measurement-based Direct Effect Estimation and through Developing an Explicit Climatological Convective Boundary Layer Model

A Thesis
Presented to
The Academic Faculty

by

Mi Zhou

In Partial Fulfillment
of the Requirements for the Degree
Doctor of Philosophy in the
School of Earth and Atmospheric Sciences

Georgia Institute of Technology
December 2006

Advancing Assessments on Aerosol Radiative Effect by Measurement-based Direct Effect Estimation and through Developing an Explicit Climatological Convective Boundary Layer Model

Approved by:

Dr. Robert E. Dickinson, Advisor
School of Earth & Atmospheric Sciences
Georgia Institute of Technology

Dr. Rong Fu
School of Earth & Atmospheric Sciences
Georgia Institute of Technology

Dr. Judith A. Curry
School of Earth & Atmospheric Sciences
Georgia Institute of Technology

Dr. Peter J. Webster
School of Civil & Environmental Engineering
and Earth & Atmospheric Sciences
Georgia Institute of Technology

Dr. Athanasios Nenes
School of Earth & Atmospheric Sciences
and Chemical & Biomolecular Engineering
Georgia Institute of Technology

Date Approved: September 25, 2006

ACKNOWLEDGEMENTS

My deepest gratitude goes to my advisor, Dr. Robert E. Dickinson, for his guidance, encouragement, and support throughout my Ph.D. studies. His scientific knowledge and perspective inspired my research and helped me overcome many challenges and frustrations during all the years. I had an invaluable and enjoyable experience to work with and learn from him, which will be a treasure for the rest of my career.

I would like to acknowledge Drs. Judith Curry, Peter Webster, Rong Fu, and Athanasios Nenes for serving on my thesis committee, for their interest in my work and insightful comments and suggestions.

Special thanks go to Dr. Hongbin Yu for his longtime assistance, collaboration, and friendship. My research has also benefited from insightful conversations with Drs. Yoram Kaufman, Mian Chin, Oleg Dubovik, and Brent Holben on normalization of aerosol direct radiative effects, with Dr. Chin-Hoh Moeng on large eddy simulations, and with Dr. Keng-Kwee Chiam on numerical implementation of Navier-Stokes equations.

Appreciation goes to my friends and colleagues who enriched my study and life here at Georgia Tech: Qian Tan, Qing Liu, Ping Jing, Qing Yang, Tao Zeng, Yan Zhang, Yuhong Tian, Liming Zhou, Janet Mcgraw, Khara Lombardi, Yanping He, Yan Huang, Huiling Gao, and many others.

Above all, I would like to thank my family, especially my husband, my parents and my sister, for their constant love, support and understanding.

TABLE OF CONTENTS

ACKNOWLEDGEMENTS iii

LIST OF TABLES vii

LIST OF FIGURES viii

SUMMARY xiii

CHAPTER 1 INTRODUCTION 1

1.1 Atmospheric Aerosol and Its Radiative Effects 1

1.2 Description of Research Objectives and Approach 2

1.2.1 Measurements Improve Assessing Aerosol Direct Radiative Effect 2

1.2.2 The Role of an Explicit Convective Boundary Layer in Estimating Aerosol Radiative Effects 5

1.3 Thesis Outline 9

CHAPTER 2 MEASUREMENT-BASED ASSESSMENTS OF THE AEROSOL DIRECT RADIATIVE EFFECT 11

2.1 Introduction and Background 11

2.1.1 Key Optical Parameters 12

2.1.2 Radiative Transfer Model 13

2.1.3 Numerical Tests of Surface Albedo on Aerosol Direct Radiative Effect 14

2.2 Description of Measurement Data 20

2.2.1 AERONET Aerosol Climatology for Distinct Aerosol Regimes 20

2.2.2 Integrated MODIS and GOCART Aerosol Optical Properties over North Africa and the Arabian Peninsula 25

2.2.3 MODIS Land Surface Albedo and Cloud Properties 32

2.3 A Normalized Description of the Aerosol Direct Radiative Effect for Distinct Aerosol Regimes 36

2.3.1 Introduction to Normalized Aerosol Direct Radiative Effect (NADRE) 36

2.3.2 Cloud-free NADRE by All-mode Aerosol 40

2.3.2.1 Biomass Burning Aerosols 40
2.3.2.2 Mineral Dust 47
2.3.2.3 Pollution Aerosols 53
2.3.3 Cloud-free NADRE by Fine-mode Aerosol 55
2.3.4 Cloudy-sky and All-sky NADRE by All-mode Aerosol 58
2.3.5 Conclusion and Discussion for NADRE 63
2.4 Application of High-resolution MODIS Land Albedo to Estimate Aerosol Direct Radiative Effect over North Africa and the Arabian Peninsula 67
2.4.1 Introduction to the Spatial Variation of MODIS Land Albedo 67
2.4.2 MODIS and CLM-CCM3 Land Surface Albedo 68
2.4.3 Results and Discussion 72
2.4.3.1 Spatial Variability of Aerosol Direct Radiative Effect 72
2.4.3.2 Regional Mean Aerosol Direct Radiative Effect 75
2.4.4 Conclusion 78
CHAPTER 3 A CONCEPTUAL MODEL OF A DRY CLIMATOLOGICAL CONVECTIVE BOUNDARY LAYER 81
3.1 Introduction 81
3.2 Conceptual Formulation 85
3.2.1 Thermal Balance 87
3.2.2 The 2-D Vortex Structure Described by Fluid Dynamics 90
3.2.3 Closures 92
3.2.4 Initial and Boundary Conditions 94
3.3 Numerical Methods 97
3.3.1 Time Integration Method 98
3.3.2 Space Discretization Method 99
3.4 Model Validation 101
3.4.1 Validation by Analytical Solution for a Reduced Problem 101
3.4.2 Validation by Large-Eddy Simulation 106
3.4.2.1 Reference Case Description 106
3.4.2.2 Mean Profiles 107
3.4.2.3 2-D Structure 115
3.5 Climatological Convective Boundary Layer Simulation 119

3.5.1 2-D Spatial Structure 119
3.5.2 Mean Vertical Profile 127
3.5.3 Sensitivity to External and Model Parameters 134
3.6 Summary and Conclusions 137
CHAPTER 4 CONCLUSIONS 140
4.1 Research Review and Major Results 140
4.2 Future Research 144
REFERENCES 147

LIST OF TABLES

Table 2.1 Solar spectral division used in Fu-Liou radiation model 13

Table 2.2 Selected AERONET stations for stratifying the data into different aerosol types and geographical regions. 23

Table 2.3 AERONET aerosol and ADRE climatology. Top panel: seasonal and zone averages of AOD (upper lines) and SSA (lower lines) at 550nm; Middle panel: seasonal and zone averages of clear-sky aerosol direct radiative effect (ADRE, Wm^{-2} at the TOA (upper lines) and the surface (lower lines). Bottom panel: blue dots indicate AEROENT stations. Light blue shadows the continents (Yu et al., 2006). 64

Table 2.4 Regional mean aerosol direct radiative effect (ADRE) derived from MODIS land surface albedo for seven spectral bands and at various spatial resolutions 77

Table 2.5 Regional mean aerosol direct radiative effect (ADRE) derived from MODIS and CLM-CCM3 surface albedos for two broadband (visible, near-infrared) at a T42 grid resolution..... 77

Table 3.1 Sensitivity experiments for the external parameters of surface heat flux H_s, cooling coefficient C_θ, and free atmosphere stratification $d\theta_0/dz$, where w_* is convective velocity scale. Bold characters refer to the reference simulation. 136

Table 3.2 Sensitivity experiments for the model parameters of eddy diffusivities K (including both K_m and K_h) and time step Δt. Bold characters refer to the reference simulation..... 136

LIST OF FIGURES

Figure 2.1 Aerosol direct radiative effect (ADRE) for surface albedo 0.0 (solid line) and 0.4 (dotted line) with solar zenith angle 30˚ (red) and 60˚ (blue) and for different aerosol single-scattering albedo (SSA) and optical depth (AOD)..... 18

Figure 2.2 Direct aerosol radiative effect with solar zenith angle for surface albedo of 0.2 and different aerosol optical depths (AODs) for single-scattering albedo (SSA) 1.0 (left panel) and different SSAs for AOD 0.5 (right panel). 19

Figure 2.3 Global distribution of AEROsol Robotic Network (AERONET) stations (red dots) and six aggregated geographical regions (blue boxes) including North America, South America, west Europe, North Africa, South Africa and east Asia (from left to right, from above to below). 23

Figure 2.4 Mean values and standard deviations of aerosol optical depth (AOD), single-scattering albedo (SSA) and asymmetry factor (g) at 550 nm for typical aerosol types and over different geographical regions, where α is surface albedo. Standard deviation is shown as the error bar. 24

Figure 2.5 Comparisons of the annual cycle of the MODIS (blue line), GOCART (green line) and assimilated (red line) aerosol optical depths with the AERONET aerosol climatology (black dots) at 6 selected sites over North Africa and the Arabian Peninsula. 26

Figure 2.6 Scatterplots of MODIS, GOCART and assimilated aerosol optical depth versus AERONET measurements with correlation coefficients of 0.73, 0.69 and 0.78 respectively. Blue cross and red triangle represents winter and summer respectively. Solid line is 1:1 relationship. 29

Figure 2.7 Linear regression of binned aerosol optical depth of MODIS, GOCART and assimilated data versus AERONET measurements with bin size of 0.04. Red solid/dotted line represents a linear fit of average/standard deviation. Solid black line is 1:1 relationship..... 30

Figure 2.8 Aerosol optical properties over Northern Africa and the Arabian Peninsula (20˚W ~ 50˚E, 10˚N ~ 40˚N) for summer 2001: a) Optical depth, b) Angstrom exponent, c) Single-scattering albedo..... 31

Figure 2.9 Oklahoma spectral albedo for grass at solar zenith angle of 60˚ (from *http://www-surf.larc.nasa.gov/surf/pages/explan.html*). 35

Figure 2.10 Global distribution of spectrally integrated monthly average MODIS land surface albedo (a) April and (b) October (Yu et al., 2004). 35

Figure 2.11 Solar-zenith-angle-averaged clear-sky normalized aerosol direct radiative effect (NADRE, unit: $Wm^{-2}\tau^{-1}$) changes with aerosol optical depth at the TOA for single-scattering albedo of 0.95 (blue) and 0.8 (red) respectively, and over different solar zenith angle distributions of 0˚-90˚ (solid line), 30˚-90˚ (dotted line) and 60˚-90˚ (dashed line). 38

Figure 2.12 South America biomass burning aerosol climatology at 550nm, aerosol direct radiative effect (ADRE) and its normalized form (NADRE) for all-mode (blue) and fine-mode (red) at site Alta_Floresta. Numbers in each panel are mean values. Green lines refer to left axis for fine-mode fraction and surface albedo..... 41

Figure 2.13 South Africa biomass burning aerosol climatology at 550nm, aerosol direct radiative effect (ADRE) and its normalized form (NADRE) for all-mode (blue) and fine-mode (red) at site Mongu. Numbers in each panel are mean values. Green lines refer to left axis for fine-mode fraction and surface albedo. 42

Figure 2.14 Mean values and standard deviations of clear-sky normalized aerosol direct radiative effect (NADRE) at the TOA and surface (unit: $Wm^{-2}\tau^{-1}$) for typical aerosol types and over different geographical regions, where standard deviations represent monthly and spatial variations in NADRE and α is surface albedo..... 45

Figure 2.15 The ratio of TOA NADRE to surface (SFC) NADRE decreases with deceasing aerosol single-scattering albedo (SSA) for biomass burning smoke over South America (blue) and over South Africa (red), respectively..... 46

Figure 2.16 Dust aerosol climatology at 550nm, aerosol direct radiative effect (ADRE) and its normalized form (NADRE) for all-mode (blue) and fine-mode (red) at site Capo_verde for surface albedo < 0.1. Numbers in each panel are mean values. Green lines refer to left axis for fine-mode fraction and surface albedo. 48

Figure 2.17 Dust aerosol climatology at 550nm, aerosol direct radiative effect (ADRE) and its normalized form (NADRE) for all-mode (blue) and fine-mode (red) at site Ilorin for surface albedo ~ 0.2. Numbers in each panel are mean values. Green lines refer to left axis for fine-mode fraction and surface albedo..... 49

Figure 2.18 Dust aerosol climatology at 550nm, aerosol direct radiative effect (ADRE) and its normalized form (NADRE) for all-mode (blue) and fine-mode (red) at site SEDE_BOKER for surface albedo ~ 0.3-0.35. Numbers in each panel are mean values. Green lines refer to left axis for fine-mode fraction and surface albedo. 50

Figure 2.19 The ratio of TOA NADRE to surface (SFC) NADRE decreases with deceasing aerosol single-scattering albedo (SSA) for mineral dust. The data are stratified with the solar-spectrum surface albedo, with blue, green, and red denoting the surface albedo α of <0.1, ~0.2, and 0.3~0.35, respectively..... 52

Figure 2.20 Pollution aerosol climatology at 550nm, aerosol direct radiative effect (ADRE) and its normalized form (NADRE) for all-mode (blue) and fine-mode (red) at

site GSFC in North America. Numbers in each panel are mean values. Green lines refer to left axis for fine-mode fraction and surface albedo. 54

Figure 2.21 Comparisons of fine-mode and all-mode aerosol NADRE (unit: $Wm^{-2}\tau^{-1}$) at the TOA (dots) and surface (triangles) for (a) biomass burning aerosol, with blue and red representing South America and South Africa respectively; and (b) mineral dust, with blue, green and red representing the surface albedo α <0.1, ~0.2, ~0.3-0.35 respectively. 56

Figure 2.22 Ratio of average cloudy-sky NADRE (NADRE_cld) to clear-sky NADRE (NADRE_clr) at the TOA and surface for typical aerosol types and over different geographical regions, where α is surface albedo. TOD and WOD denote respectively the average total and water cloud optical depth from MODIS/Terra observations. 59

Figure 2.23 Correlation between the ratio of all-sky to clear-sky forcing efficiency and clear-sky fraction for all AERONET sites, for below-cloud (upper panel) and within-cloud (lower panel) cases. The data are stratified by cloud optical depth (COD), with blue, green, and red representing COD <10; COD ~ 10-20; and COD > 20, respectively. 62

Figure 2.24 White-sky (0.3-4.0μm) land surface albedo at T42 grid over Northern Africa and the Arabian Peninsular (20˚W ~ 50˚E, 10˚N ~ 40˚N) in summer 2001 for a) CLM-CCM3 and b) MODIS retrieval (grids including both ocean and land are eliminated).... 71

Figure 2.25 Aerosol direct radiative effect (ADRE, unit: Wm^{-2}) over Northern Africa and the Arabian Peninsula (20˚W ~ 50˚E, 10˚N ~ 40˚N) for summer 2001 using MODIS land surface albedo for seven spectral bands and on 0.2˚ × 0.2˚ resolution, and aerosol optical properties on T42 grid: a) 0.3-4.0μm broadband white-sky surface albedo; b) TOA ADRE c) surface ADRE; d) atmosphere ADRE. 74

Figure 3.1 Comparison in temperature profiles between numerically modeled (solid line) and analytical solved (dotted line) 1-D heat diffusion equation for constant boundary flux condition of 0.5 K m s^{-1} at height zero and constant thermal diffusivity of 1000 m^2 s^{-1}. 104

Figure 3.2 Temperature profiles of numerically modeled (solid line) 1-D heat convection-diffusion equation and analytical solved (dotted line) 1-D heat diffusion equation for constant boundary flux condition of 0.5 K m s^{-1} at height zero and constant thermal diffusivity of 100 m^2 s^{-1}. 105

Figure 3.3 Time evolution of PBL height from a) LES with thick line for 3-D, dotted line for 2-D-A and thin solid lines for 2-D-B (Meong et al., 2004); b) our model with solid line for Experiment A and dotted line for Experiment B..... 110

Figure 3.4 Vertical profiles of the mean heat flux from a) 3-D LES (Meong et al., 2004); b) 2-D-A LES (Meong et al., 2004); c) Experiment A of our model; d) Experiment B of our model (total as solid line, resolved scale as dotted line and small scale as dashed line). 111

Figure 3.5 Vertical profiles of the mean potential temperature averaged over between hour 3 – 6 for initial profile as the dotted line in b from a) LES with thick line for 3-D and thin solid lines for 2D-B (Meong et al., 2004); b) our model with dashed line for Experiment A and solid line for Experiment B. 113

Figure 3.6 Vertical profiles of the resolved-scale velocity variance from a) 3-D LES and b) 2-D-A LES for $\overline{u^2}$ as solid line, $\overline{v^2}$ as dotted line and $\overline{w^2}$ as dotted-dashed line (Meong et al., 2004); c) Experiment A of our model and d) Experiment B of our model ($\overline{u^2}$ as solid line and $\overline{w^2}$ as dotted-dashed line). 114

Figure 3.7 Contours of u (top) and w (bottom) velocity in an x-z cross section at hour 4 of 3-D LES with contour interval of 1 m s^{-1} and the gray area for positive values **(**Meong et al., 2004). 117

Figure 3.8 Contours of u (top) and w (bottom) velocity in an x-z cross section at hour 4 of 2-D-A LES with contour interval of 1 m s^{-1} and the gray area for positive values **(**Meong et al., 2004). 117

Figure 3.9 Contours of u (top) and w (bottom) velocity in x-z cross section at hour 4 for Experiment A of our model with contour interval of 0.1 m s^{-1}, where the solid line for positive values and dotted line for negative values. 118

Figure 3.10 Stream function contours for the 2-D reference climatological convective boundary layer with starting value of ±5 and contour interval of 20, i.e. contours of ±5, ±25, ±45…, where the solid line for positive values and dotted line for negative values (units: m^2s^{-1}). 122

Figure 3.11 Vector plot of convective velocity for the 2-D reference climatological convective boundary layer with the directed arrows showing the direction and relative magnitude. 122

Figure 3.12 Vorticity contours for the 2-D reference climatological convective boundary layer with starting value of $\pm 1.0\times10^{-4}$ and contour interval of 3.0×10^{-4}, i.e. contours of $\pm 1.0\times10^{-4}$, $\pm 4.0\times10^{-4}$, $\pm 7.0\times10^{-4}$…, where the solid line for positive values and dotted line for negative values (units: ms^{-2}). 123

Figure 3.13 Contour plot of convective vertical velocity for the 2-D reference climatological convective boundary layer with starting value of ±0.05 and contour interval of 0.05, i.e. contours of ±0.05, ±0.1, ±0.15…, where the solid line for positive values and dotted line for negative values (units: ms^{-1}). 125

Figure 3.14 Contour plots of convective temperature fluctuation for the 2-D reference climatological convective boundary layer with starting value of ±0.1 and contour interval of 0.3, i.e. contours of ±0.1, ±0.4, ±0.7…, where the solid line for positive values and dotted line for negative values (units: K). 125

Figure 3.15 Contour plot of convective horizontal velocity for the 2-D reference climatological convective boundary layer with starting value of ±0.05 and contour interval of 0.05, i.e. contours of ±0.05, ±0.1, ±0.15…, where the solid line for positive values and dotted line for negative values (units: ms^{-1})..... 126

Figure 3.16 Vertical profiles of mean potential temperature for the 2-D climatological convective boundary layer for a) convective scale perturbation; b) ensemble mean state with initial profile as the dotted line in b (units: K)..... 129

Figure 3.17: Vertical profiles of mean heat flux versus normalized height for the 2-D reference climatological convective boundary layer, where solid, dotted and dashed lines represent total, resolved scale and small scale respectively (units: K m/s), where z_i is the PBL height. 130

Figure 3.18 Vertical profiles of velocity moments statistics versus normalized height for the 2-D reference climatological convective boundary layer for a) velocity component variance ($\overline{u^2}$ as solid line and $\overline{w^2}$ as dotted-dashed line); b) vertical velocity skewness. 133

SUMMARY

The first part of the thesis assesses the aerosol direct radiative effect (ADRE) with a focus on ground-based AERONET and satellite MODIS measurements. The AERONET aerosol climatology is used, in conjunction with surface albedo and cloud products from MODIS, to calculate the ADRE and its normalized form (NADRE) for distinct aerosol regimes. The NADRE is defined as the ADRE normalized by optical depth at 550 nm and is mainly determined by internal aerosol optical properties and geographical parameters. These terms are evaluated for cloud-free and cloudy conditions and for all-mode and fine-mode aerosols. Because of stronger absorption (smaller single-scattering albedo) by the smoke over South Africa, the average NADRE over South America is ~35% larger at the TOA but ~38% smaller at the surface than that over South Africa. As the surface albedo varies from ~0.1 to ~0.35, it is observed that the dust NADRE ranges from -44 to -17 $Wm^{-2}\tau^{-1}$ at the TOA and from -80 to -48 $Wm^{-2}\tau^{-1}$ at the surface over the Saharan deserts, Arabian Peninsula, and their surrounding oceans. We find that the NADRE of fine-mode aerosol is larger at the TOA but smaller at the surface in comparison to that of all-mode aerosol because of its larger single-scattering albedo and smaller asymmetry factor. Cloudy-sky ADRE is usually not negligible for the observed cloud optical thickness but the TOA ADRE with clouds is sensitive to the relative location of aerosols and cloud layer. The high-resolution MODIS land surface albedo is applied, together with aerosol optical properties from an integrated MODIS retrieval and a chemical transport model simulation, to study the clear-sky ADRE over North Africa and the Arabian Peninsula for summer 2001, where surface is highly

reflective with considerable spatial variability but poorly described by modeling. TOA ADRE shows the high spatial variability with close similarity to that of surface albedo. The albedos derived from the Common Land Model changes the regionally averaged positive TOA ADRE (3 ~ 4 Wm^{-2}) based on MODIS albedo to negative (~ -2 Wm^{-2}).

The second part of the thesis is to develop a 2-D conceptual model for a climatological convective boundary layer over land as a persistent and distinct component in climate models, where the convective-scale motion is explicitly described by fluid dynamics and thermodynamics while the smaller scale effect is parameterized for a neutral stratification. Our conceptual model reasonably reproduces essential statistics of a convective boundary layer in comparison to large eddy simulations. The major difference is that our model produces a better organized and more constrained spatial distribution with coherent convective cells. The simulations for a climatological convective boundary layer are conducted for a prescribed constant and homogenous surface heat flux and a specified cooling term representing the background large scale thermal balance. The results show: the 2-D coherent structures of convective cells with horizontal and vertical characteristic scales comparable with PBL height; downward maximum velocities being 70-80% of the accompanying upward maxima; vertical profiles of a constant potential temperature and linear decreasing heat fluxes; a nearly proportional increase in the mixed-layer temperature and square-root increase in the velocity magnitude with increasing surface heat flux.

CHAPTER 1

INTRODUCTION

1.1 Atmospheric Aerosol and Its Radiative Effects

Atmospheric aerosols (or particulate matter) are solid and/or liquid particles suspended in the air. Aerosols vary in size (from a few nanometers to tens of micrometers in diameter), chemical composition (sulfate, nitrate, organic carbon, soot, dust, sea salt etc.), and shape (spherical or non-spherical). Primary aerosols are emitted directly into the atmosphere and secondary aerosols are formed by gas-to-particles conversion processes of nucleation, condensation and coagulation. Particles arise from natural sources or anthropogenic activities, belonging to the natural and anthropogenic aerosols respectively. Aerosols can be divided into fine-mode ($d < 1$ μm) and coarse-mode ($d > 1$ μm) particles according to size in diameter.

The earth-atmosphere system is in radiative equilibrium between incident solar radiation, emitted thermal infrared and reflected solar radiation. Aerosols modify earth-atmosphere energy budget through several ways. They scatter and absorb solar and thermal infrared radiation (the so-called direct effect) [Bohren and Huffman, 1983; Coakley et al., 1983; Charlson et al., 1992]; change atmospheric thermodynamics and cloud formation (the so-called semi-direct effect) [Hansen et al., 1997; Ackerman et al., 2000; Koren et al., 2004]; also serve as cloud condensation nuclei, increasing the number concentration while decreasing the size of cloud droplets to change cloud optical properties and cloud life time (the so-called indirect effects) [Twomey, 1977; Albretch, 1989; Rosenfeld and Lensky, 1998]. When the radiative equilibrium is perturbed, the

earth-atmosphere system will adjust subsequently to reach a new radiative equilibrium state. Consequently, aerosols can influence land surface process and the atmospheric boundary layer [Yu, et al., 2002], global surface temperature [Coakley et al., 1983; Charlson et al., 1992; Ramanathan et al., 2001], climate and hydrological cycle [Ramanathan et al., 2001], and ecosystems [Chameides et al., 1999].

The radiative effects of aerosols are a critical component of the global and regional climate. IPCC [2001] estimated that the cooling by anthropogenic aerosols may be comparable in magnitude to greenhouse gas warming on a global scale but can be much larger on a regional scale. In the past decades, a great deal of effort has been made to study aerosol raditive effects. However, uncertainties remain substantial for the direct effect and are even much larger for the indirect effect [IPCC, 2001; Anderson et al., 2003a].

1.2 Description of Research Objectives and Approach

1.2.1 Measurements Improve Assessing Aerosol Direct Radiative Effect

The aerosol direct effect is determined by the temporal and spatial aerosol distribution and aerosol optical properties. However, the high spatial and temporal variability due to localization of sources and short lifetime makes the characterization extremely difficult. Until recently, estimates of the global impact of aerosols on climate were primarily based on model results that were evaluated using local aerosol measurements [see summary given by Haywood and Boucher, 2000]. Recently, significant progress has been achieved in measurement-based aerosol characterization from satellite remote sensing, surface networks, aircraft and in situ measurements.

Ground-based Observations can provide detailed aerosol characterizations but for limited spatial scales only. The AEROsol Robotic Network (AERONET), a ground-based remote sensing network equipped with well-calibrated sunphotometers over more than 100 sites throughout the world, measures and derives quality-assured aerosol optical properties for a wide variety of aerosol regimes, for up to the last 10 years, including spectral variations of aerosol optical depth, single-scattering albedo, the phase function/asymmetry factor for both fine-mode and coarse-mode aerosols [Holben et al., 1998; 2001; Dubovik et al., 2002]. These high quality data have been widely used for aerosol process studies and evaluation and validation of model simulation and satellite remote sensing of aerosols [Chin et al., 2002; Yu et al., 2003; Remer et al., 2005]. The separation of fine-mode from coarse-mode aerosol properties as done by AERONET provides a possible way to estimate the anthropogenic aerosol direct forcing because anthropogenic aerosols are overwhelmingly concentrated in the fine-mode [Kaufman et al., 2002]. However, most fine-mode particles are not necessarily anthropogenic. How to derive anthropogenic aerosol direct forcing by making use of fine-mode aerosol information needs further study [Anderson et al., 2005].

Aerosols can be characterized on a regional or global scale by satellite remote sensing or Chemical Transport Model (CTM) simulations. The MODerate resolution Imaging Spectroradiometer (MODIS) aboard NASA Terra spacecraft measures radiance in multiple wavelengths from in the UV through the IR at high spatial resolution. Seven channels between 0.47 and 2.13 μm are used to retrieve aerosol properties over cloud and surface-screened areas [Martins et al., 2002; Li et al., 2004]. It is sampling aerosol optical depths over the ocean and vegetated land with nearly global coverage [Kaufman et al.,

1997; Tanré et al., 1997; Remer et al., 2005]. Over vegetated land, MODIS is capable of retrieving aerosol optical depth at high accuracy of $\pm 0.05 \pm 0.2\tau$ [Chu et al., 2002; Remer et al., 2005]. Satellite remote sensing can provide global scale but only for a limited set of aerosol properties, such as optical depth and its wavelength dependence. CTM can simulate spatial and temporal aerosol distribution and optical parameters, however, as a model it suffers from large uncertainties in describing various aerosol processes, such as source, sink and mixing. The Georgia Tech/Goddard Global Ozone Chemistry Aerosol Radiation and Transport (GOCART) model simulates major aerosol components, including sulfate, organic carbon, black carbon, mineral dust, and sea-salt [Chin et al., 2002]. An integrated description of MODIS and GOCART aerosol optical depth by data assimilation [Yu et al., 2003] compares to AERONET measurement better than does either MODIS retrieval or GOCART simulation alone.

How aerosols modify solar radiation is strongly influenced by surface albedo [Coakley et al., 1983; Haywood and Shine, 1995; 1997]; this interaction leads to complicating multiple reflections. Therefore, an inadequate specification of the highly heterogeneous land surface albedos [Dickinson, 1983] may thus introduce additional uncertainties in aerosol direct forcing [Collins et al., 2002]. Surface albedos for climate radiation studies have usually been calculated from land models based on empirical parameterizations of vegetation and soils [Dickinson et al., 1993; Sellers et al., 1996]. MODIS is now providing high quality spectral land surface albedo for direct and diffuse radiation. The multispectral capability of MODIS allows for better atmospheric correction [Vermote et al., 2002] and improves the quality of the retrieved land albedo data [Schaaf et al., 2002]. Such a better knowledge of land albedo improves the accuracy

of aerosol radiative effect calculations to avoid the significant error that land models may entail.

It is thus feasible and important to generate a measurement-based climatology of the aerosol direct radiative effect that will serve for evaluating both satellite-based and model-based forcing and provide observational constraints [Zhou et al., 2005; Yu et al., 2006]. The first part of this thesis work was attempted to utilize the high quality measurements of aerosol optical properties and geographic parameters to improve the assessments of aerosol direct radiative effect.

1.2.2 The Role of an Explicit Convective Boundary Layer in Estimating Aerosol Radiative Effects

The aerosol direct and semi-direct effects warm the atmosphere but cool the surface and hence increase atmospheric stability, suppress convection and decrease cloud cover [Hansen et al., 1997]. Such coupling suggests the need for a more physically transparent convective boundary layer model to explore the fundamental basis of dry or moist convection in response to atmospheric temperature profile and radiative balance changes by aerosols. Moreover, the aerosol indirect effect acts through the role of aerosols as cloud condensation nuclei and involves cloud generation. Quantitative characterization of such aerosol effects requires a dynamically more realistic representation of the circulation system of aerosol producing clouds within a climate model [Nenes and Seinfeld, 2003]. The aerosol influence on convective systems is of particular interest in regard to the induced change in precipitation and hydrological cycle.

The studies that attempt to assess the impact of aerosol direct, semi-direct and indirect effects on convection and hence precipitation use a regional [Huang et al, 2006] or global climate models [Menoe et al., 2002; Giorgi et al., 2002; Takemure et al., 2005].

However, in current climate models, standard conceptual descriptions in the literature view convection as transient structure in 1-D terms, involving bubbles, plumes, and mixing lengths etc. One reason is that some of the basic ideas have been derived from laboratory experimentation that takes this form [e.g., Willis and Deardroff, 1974]. Convection in terms of such 1-D descriptions are parameterized by local or non-local formulations through the mean fields. Eddy diffusivity [Mellor and Yamada, 1974; Toren and Mahrt, 1986] and mass flux approaches [Arakawa and Schubert, 1974; Zhang and Anthes, 1982; Wang and Albrecht, 1990; Lappen and Randall, 2001] are representative of local and non-local schemes, respectively. Eddy diffusivity can be supplemented by a non-local term to account for counter-gradient transport. In mass-flux schemes, the updraft mass flux and properties are modified by lateral entrainment and detrainment, which is specified by parameterization. These terms should not be confused with "entrainment" used to describe the incorporation of nonboundary layer air into the boundary layer air. This latter "entrainment" can occur in either the entrainment or detrainment region of the convection.

Unfortunately, such simple models of convection do not seem to have progressed very far and may not be able to respond well to the change of atmosphere temperature profile and surface radiative energy budget. On the other hand, the details of convective boundary layer have been studied by large eddy simulations [Deardroff ,1972; Moeng, 1984; Moeng and Sullivan 2002] or cloud resolving models [Krueger, 1988; Grabowski et al., 1996; Xu and Randall 1996] with high computational efforts. The apparent failure of all current approaches to represent convection and hence clouds in climate models has led Randall et al. [2003] to propose the inclusion of a "super parameterization", i.e.

inclusion of a 2-D cloud resolving model within a global model. This concept appears to provide major improvements but increases the computational cost of the climate model by orders of magnitude. So, is there a more efficient approach to achieve the same objective?

The second part of this thesis contributes to an effort to improve the quantitative estimation of aerosol radiative effects by developing a convective boundary layer model in the framework of computational fluid dynamics and thermodynamics. A convective boundary layer is clearly a chaotic system. Indeed, the concept of chaos was discovered by a meteorologist named Lorenz [1963] when he was running simple models of atmospheric convection. Chaos means that solutions are never the same in detail but they may have "attractors" that are places in its solution space where they like to hang around. The underlying concept is that of "coherent" structures. It has been noticed for a few decades that turbulence organizes itself into large eddies that provide much of the large scale effect of the turbulence [Deardroff, 1972; Webb, 1977; Schmidt and Schumann, 1989; Moeng and Rotunno, 1990; Holstslag and Moeng, 1991].

What appears to be the most important attractors of boundary layer convection? These appear to be the PBL convective rolls or bubbles and these "coherent" structures generally have the appearance of vortices, hence it is intuitive to model them with simple vorticity models. It has been recognized that turbulence is better addressed with vorticity concepts. These concepts live on in complex LES simulations but have been lost in the simple conceptual descriptions in the atmospheric sciences literature. Eddies on the scale of the boundary layer are responsible for much of the structure and function of the convective boundary layer [e.g. Williams and Hacker, 1993; Taconet and Weill, 1983]

and therefore are of primary importance. Such strong thermals mix air throughout the CBL and uniformly distribute conserved scalars such as potential temperature and trace gases.

From a global perspective, it is generally agreed that the first kilometer or two of the earth's atmosphere is most strongly controlled by vertical convective processes that for dry conditions maintain a lapse rate of near dry adiabatic. Although over land, this structure only strictly holds during the day, at night it is only seriously modified within a shallow nighttime boundary layer. Above that is maintained a close to adiabatic "residual" layer over the depth to which the daytime boundary layer extended the previous day. Therefore, convection exists on a climatological basis over much of the world and should be describable as an average condition of the atmosphere. Betts [2000] has emphasized the need to better clarify the role of time averaged boundary layers over land as a component of the climate system. The long term equilibrium convection system instead of a transient response is necessary to assess the climatic response to aerosol radiative effects and associated feedbacks. Such has only been formulated in terms of 1-D radiative-convective equilibrium models intended to approximate the global average of atmosphere thermodynamic structure and its sensitivity to climate changes, such as CO2 increases [Renno, 1994 and references therein]. However, little is known about the underlying physical processes that are responsible for convection to adjust an unstable atmosphere from a pure radiative equilibrium [Renno, 1996].

Our methodology is to simulate the climatological convection as 2-D vortices based on fluid dynamics and thermodynamics to better clarify the distinct climatological role of convection within the boundary layer. Convective motion is composed of strong

and narrow upward and compensating weak and broad downward legs with velocity w, which lead to convergence source region and divergence sink region with velocity u near the bottom and top of the updraughts with strong lateral entrainment [Crum et al., 1987; Schmidt and Schumann 1989]. Such a circulation clearly has a 2-D structure. The source region u is commonly referred to as the entrainment and the sink region as the detrainment. The emphasis of our approach is the role and structure of large scale convection as distinct from the smaller scale turbulence. The objective is to generate a model of the convective boundary layer where the vertical transport of heat, momentum, and moisture on the convective scale is explicitly modeled but in simpler (fewer degrees of freedom than full system) multidimensional eddies, while the small scale turbulent effects are parameterized. Our target is to make models that are physically plausible and only one step more complicated than the ideas currently used in climate models. The next level of climate model parameterizations will have to be built from such characterizations of boundary layer and convective atmospheric systems.

1.3 Thesis Outline

The aforementioned two research topics are addressed in Chapter 2 and Chapter 3 respectively organized as follows.

Chapter 2 assesses the measurement-based aerosol direct radiative effects. After the background introduction and measurement data description, Section 2.3 presented normalized aerosol direct radiative effects for distinct aerosol regimes by making use of the AERONET aerosol climatology and MODIS retrieved land surface albedo and clouds. Such can be flexibly used to evaluate estimates of aerosol direct radiative forcing using satellite observations, model simulations, and their combinations. The spatial and spectral

high-resolution MODIS land surface albedo is applied in Section 2.4, in combination with the assimilated MODIS-GOCART aerosol information, to study the aerosol direct radiative effect over Northern Africa and the Arabian Peninsula, where the suface albedo is relatively large and demonstrates considerable spatial variability.

Chapter 3 describes our conceptual model for a climatological convective boundary layer, where the 2-D coherent structures are explicitly resolved. An introduction is given in Section 3.1. The development of the model includes conceptual formulations (Section 3.2) and numerical methods (Section 3.3). Section 3.4 validates the model by analytical solution for a reduced problem and large eddy simulation for a dry convection case. Then the model is applied to simulate a climatological convective boundary layer in Section 3.5.

Chapter 4 summarizes the major conclusions and implications of this thesis, and discusses future investigation plans.

CHAPTER 2

MEASUREMENT-BASED ASSESSMENTS OF THE AEROSOL DIRECT RADIATIVE EFFECT

2.1 Introduction and Background

Aerosols have a direct radiative effect by scattering and absorbing solar and thermal infrared radiation, hence they influence the earth-atmosphere energy budget and climate. Herein, we designate a perturbation of net radiant flux (i.e. irradiance) by the total aerosol (natural plus anthropogenic) as aerosol radiative effect. The aerosol direct radiative effect and its potential influence on climate can be traced back to the late 1960s [e.g. McCormick and Ludwig, 1967; Charlson and Pilat 1969].

The aerosol effect on the thermal infrared radiation will not be considered in this section since it is generally negligible [Coakley et al., 1983], because 1) most aerosols are small compared to thermal wavelengths, which leads to a rapid decrease of optical depth with wavelength; 2) they are usually concentrated near the surface due to short lifetime, where the temperature is close to that of the surface. An exception is lofted dust aerosols with large size, which can have a significant positive thermal forcings and introduce relatively large uncertainties on aerosol direct forcing estimation [Sokolik et al., 1998].

The interactions between aerosols and solar radiation are determined by a combination of aerosol optical properties and geographic parameters. These determining factors vary for different regions. Recent advances in observations provide a good opportunity to improve the estimate of the aerosol direct radiative effect. Observations (ground-based, airborne, and shipborne) can provide detailed aerosol optical properties

including aerosol optical depth, single-scattering albedo, and phase function. Satellite remote sensing can provide optical depth and geographical parameters on nearly global coverage. With a full set of aerosol information and geographical parameters available, a radiative transfer model is run with and without aerosols to derive the aerosol direct effect as the difference of solar radiative fluxes at the top of atmosphere (TOA), in the atmosphere and at the surface.

2.1.1 Key Optical Parameters

The important optical parameters that govern aerosol absorption and scattering in the radiation equations are optical depth, single-scattering albedo and phase function. These parameters vary with the wavelength of radiation.

1) Optical depth is a measure of e-folding loss of incident direct solar radiation at zenith after passing through aerosol layer due to aerosol scattering and absorption. Optical depth is also an indicator of aerosol loading in the atmosphere. Its wavelength (λ) dependence is usually described as $\propto \lambda^{-\alpha}$, where α is Angstrom exponent. Large/small values of Angstrom exponent indicate small/large particles respectively.

2) Single-scattering albedo is the fraction of scattered light with respect to the sum of scattered and absorbed light. It is a measure of aerosol absorption. Single-scattering albedo is 1.0 for transparent aerosols such as pure sulfates and sea salt and decreases with increasing aerosol absorption. Black carbon is the most important light-absorbing material in particles.

3) Phase function is the angular distribution of light scattering, i.e., a ratio of the scattered intensity at a specific direction to the integral of the scattering density at all directions. It is usually parameterized using an asymmetry factor (g) in radiative transfer models. The

asymmetry factor is a measure of the asymmetry of aerosol forward and backward scattering, g =1 for complete forward scattering, g =-1 for complete backward scattering. The smaller the particles, the smaller the magnitude of g is. For air molecules, the scattering (Rayleigh) is symmetric in forward and backward hemisphere and g =0. For aerosols, the typical values of g is 0.5 ~ 0.8. The amount of upscattered radiation relative to the local horizon determines the cooling effect for the whole earth-atmosphere system.

2.1.2 Radiative Transfer Model

We use the Fu-Liou radiative transfer model [Fu and Liou, 1992, 1993], which is a four-stream broadband model with a delta-function adjustment accounting for the strong forward scattering of large particles for the solar radiation. The model has 6 bands (Table 1) in the solar spectrum, and the first solar band (0.2-0.7μm) is further divided into 10 intervals. This allows us to explicitly incorporate the spectral dependence of aerosol optical properties and land surface properties. In the solar spectrum, Rayleigh scattering and absorption of O_3, H_2O, O_2 and CO_2 have been taken into consideration. The Fu-Liou model shows reasonable accuracy against a number of other radiative schemes [Boucher et al., 1998; Yu, 2002].

Table 2.1 Solar spectral division used in Fu-Liou radiation model

Band number	1	2	3	4	5	6
Band range (μm)	0.2-0.7	0.7-1.3	1.3-1.9	1.9-2.5	2.5-3.5	3.5-4.0
Central λ	0.55	1.0	1.6	2.2	3.0	3.7

The radiative transfer model is employed to calculate the aerosol direct radiative effect (ADRE), which is defined as the difference of solar radiative flux with and without

aerosols for the top of atmosphere (TOA) and surface. The residual of TOA and surface ADRE is the atmosphere ADRE. The aerosol radiative effect on change of TOA albedo, i.e. planetary albedo, is also a useful parameter. TOA albedo is the ratio of the upward solar radiation to the downward solar insolation at top of atmosphere. The change of TOA albedo tells us the sign of the radiative forcing at the TOA, which represents cooling or warming effect on the earth-atmosphere system.

The climatology from McClatchey et al. [1972] is taken for average atmospheric conditions in our calculation. This choice of temperature, water vapor and ozone profiles has a small influence on the calculation of aerosol solar radiative effect [*Boucher et al.*, 1998; *Yu et al.*, 2004]. A time-step of 30 min is applied to adequately capture the solar zenith angle dependence of the aerosol radiative effects.

2.1.3 Numerical Tests of Surface Albedo on Aerosol Direct Radiative Effect

Aerosols directly scatter and absorb solar radiation, leading to concurrent surface cooling and atmosphere heating. Part of surface cooling is offset by atmosphere heating, and the remainder is TOA forcing with relatively small absolute values. Surface albedo plays an important role in ADRE in two steps. First, as a primary parameter controlling earth-atmosphere solar energy budget, it modifies the aerosol solar perturbation as sunlight reaches the surface. Let's assume the solar radiation just reaching the surface is F_0 for clean atmosphere and surface albedo is α, so the surface-reflected solar flux is $F_0(1-\alpha)$. When an aerosol is present, part of solar radiation is upscattered back into the space by scattering and part is trapped in the atmosphere by absorption, and then the solar radiation reaching the surface is reduced to $F_0(1-\alpha_a)$, where α_a is the fraction of solar radiation attenuated by aerosols, so the instantaneous surface-reflected solar flux

is $F_0(1-\alpha_a)(1-\alpha)$. The aerosol forcing at the surface for single scattering process is then $-\alpha_a F_0(1-\alpha)$, where minus sign means negative forcing. Obviously the surface cooling is increased with decreasing surface albedo. Second is the effect on the surface-reflected solar energy. Through multiple scattering and absorption between surface and aerosol layers, aerosols absorb and scatter back surface-reflected solar energy, leading to a nonlinear atmosphere heating increase as well as a surface cooling decrease, eventually increasing solar energy in the earth-atmosphere system.

We conduct extensive numerical tests to examine the effect of each factor on the aerosol radiative effect. Results show that Angstrom exponent (α) and asymmetry factor (g) have smaller effects on ADRE than optical depth and single-scattering albedo. For conditions of solar zenith angle = 60˚, broadband surface albedo = 0.1, optical depth = 0.5, single-scattering albedo = 0.9, g = 0.7 and α = 1, the change in TOA and surface ADREs due to ± 0.05 change in g or ± 0.5 change in α are within 10% or 7%, respectively. The change in corresponding atmosphere ADREs due to either change of g or α are also within 10%. Therefore, the following discussion will focus on the dependence of ADREs on aerosol optical depth, single-scattering albedo, surface albedo and solar zenith angle (i.e. Sun position). The asymmetry factor is taken as 0.7 and Angstrom exponent as 0, which means no wavelength dependence for optical depth.

Figure 2.1 illuminates how surface albedo affects aerosol-radiation interaction for different aerosol optical depth (AOD), single-scattering albedo (SSA) and solar zenith angle (SZA). Similar trends of aerosol direct radiative effect (ADRE) at TOA and surface are observed for AOD =0.5 and AOD =0.25, suggesting that different AODs primarily affect the magnitude of ADRE. For the extreme surface albedo of 0, there is always

cooling at the TOA. An increase in SSA increases the TOA ADRE (negative) while decreases the air ADRE (positive) and surface ADRE (negative). With increasing surface albedo, the aerosol ADRE changes with increasing SSA more rapidly. The TOA and surface cooling decreases and atmospheric heating by absorbing aerosol increases with increasing surface albedo, due to multiple scattering between the surface and aerosol. Surface ADRE is always negative and increases with increasing AOD and decreasing SSA. A positive TOA ADRE can result from small SSA and large surface albedo, and the change of sign from cooling to warming also depends on SZA.

The interaction of surface albedo and aerosol on ADRE also depends on SZA. Figure 2.2 illustrates the change of ADRE as a function of SZA at different AOD and different SSA for surface albedo of 0.2. The change of the TOA albedo generally increases with increasing solar zenith angle, optical depth and single-scattering albedo due to increased aerosol upscattering. For non-absorbing aerosols, the TOA albedo always increases, hence exerting a cooling effect. The strongest cooling at the TOA happens at SZA of 60˚~80˚, with a shift to higher SZA when scattered radiation decreases from decreasing AOD or SSA, because there is more contribution of upscatter fraction from forward scattering but less solar insolation at higher SZA. This is consistent with other studies [Nemesure et al., 1995; Boucher et al., 1998]. For absorbing aerosols, the TOA albedo can decrease at smaller SZA, i.e. provide a warming effect for the whole earth-atmospheric system, and increase at larger SZA. Note that at SZA range of 0˚~30˚, the air ADRE changes little with SZA for absorbing aerosol, because the decreased insolation as SZA increasing is cancelled out by the increase of the light path through the aerosol layer.

In summary, ADRE increases with aerosol optical depth at the TOA, atmosphere and surface, respectively. With an increase of single-scattering albedo, ADRE increases at the TOA, but decreases for the atmosphere and surface. With increasing surface albedo, the surface cooling decreases while atmosphere heating increases as expected. Both move TOA forcing in the same direction, therefore TOA cooling is reduced considerably, even changed to TOA warming. The ADRE is nearly linear with aerosol single-scattering albedo. With increasing surface albedo, the slope change of TOA ADRE with respect to single-scattering albedo is sharper than that of surface ADRE, indicating TOA forcing is sensitive to surface albedo. The strongest TOA cooling happens at SZA of 60˚~80˚, accompanied by a decreasing atmospheric heating with increasing SZA.

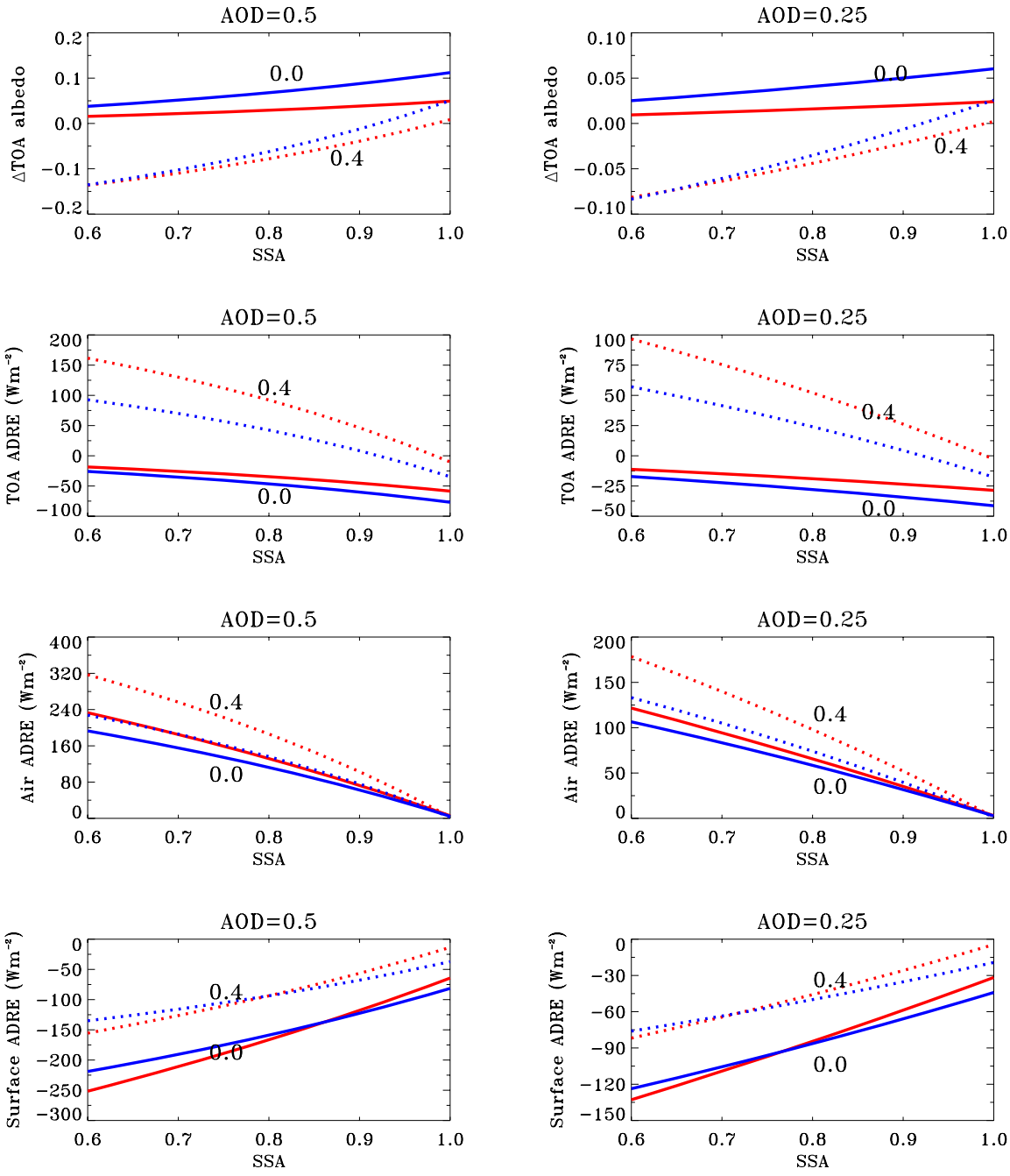

Figure 2.1 Aerosol direct radiative effect (ADRE) for surface albedo 0.0 (solid line) and 0.4 (dotted line) with solar zenith angle 30˚ (red) and 60˚ (blue) and for different aerosol single-scattering albedo (SSA) and optical depth (AOD).

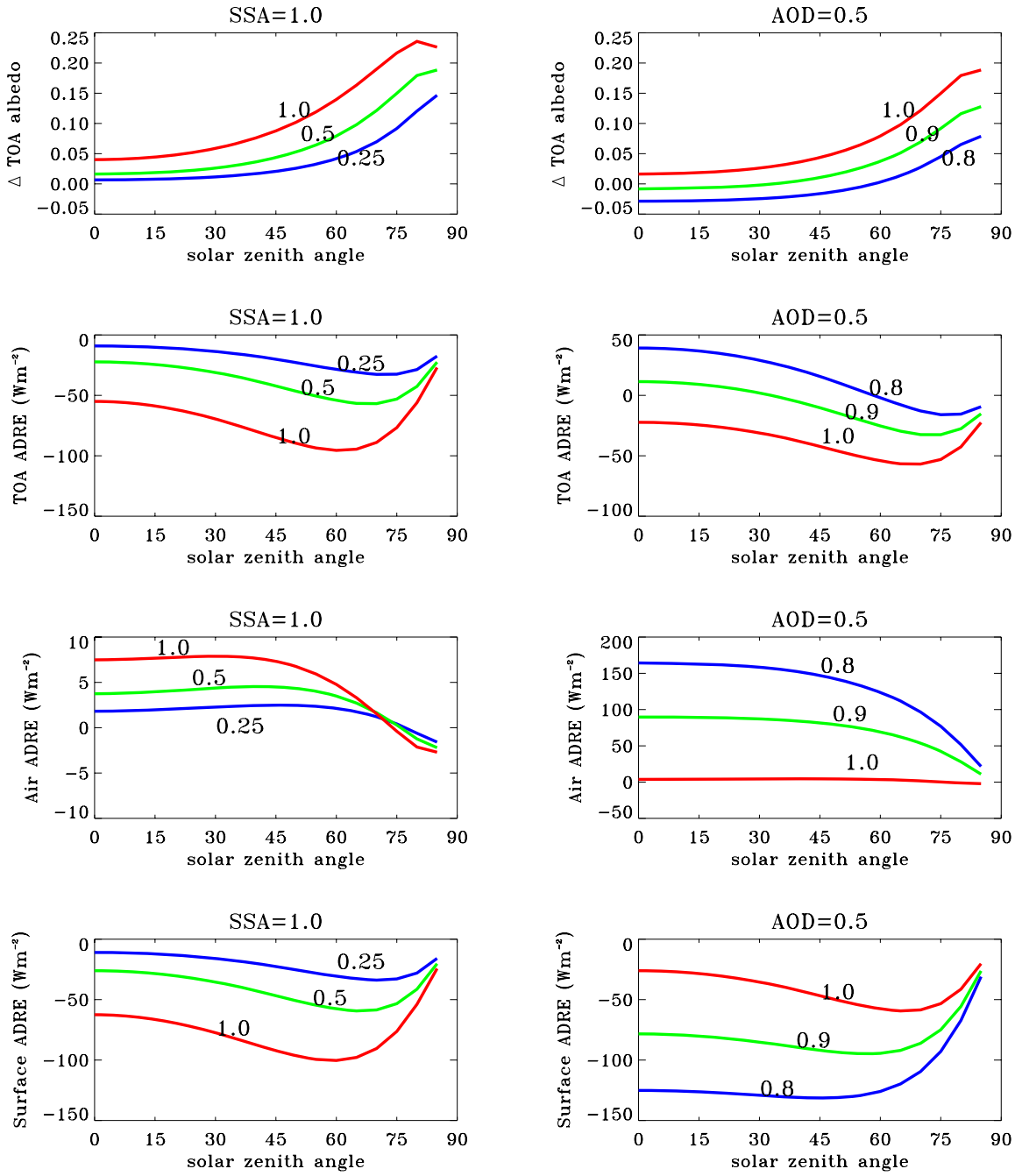

Figure 2.2 Direct aerosol radiative effect with solar zenith angle for surface albedo of 0.2 and different aerosol optical depths (AODs) for single-scattering albedo (SSA) 1.0 (left panel) and different SSAs for AOD 0.5 (right panel).

2.2 Description of Measurement Data

2.2.1 AERONET Aerosol Climatology for Distinct Aerosol Regimes

The AERONET program is an inclusive network of ground-based aerosol remote sensing sites with more than 100 around the world measuring for up to 10 years [Holben et al., 1998; 2001]. Spectral measurements from sunphotometers and sky radiance radiometers are calibrated and screened for cloud-free conditions [Smirnov et al., 2000]. Flexible algorithms have been developed to derive the columnar integrated and spectral-resolved aerosol optical properties in distinct aerosol regimes [Holben et al., 1998; 2001; Dubovik et al., 2000a; 2000b; 2002]. The data used in this study are cloud-screened and quality-assured (Level 2.0) monthly aerosol climatology, including optical depth, single-scattering albedo, and the asymmetry factor at 440, 670, 870, 1020 nm for both fine-mode aerosol and all-mode (including fine-mode and coarse-mode) aerosol. The wavelength dependence of optical depth is described by an Angstrom exponent, which is calculated as the linear regression slope $-\ln\tau/\ln\lambda$, where τ is optical depth and λ is wavelength.

It should be noted that the inversion-based retrievals of single-scattering albedo and asymmetry factor have yet to be systematically validated by in situ measurements. We simply take the standard deviations of single-scattering albedo and asymmetry factors as uncertainties [Dubovik et al.; 2002] to study the associated uncertainties in aerosol forcing estimation. The variability in single-scattering albedo can lead to uncertainty in aerosol absorption, i.e. $1-\omega$, where ω is single-scattering albedo. Biomass burning aerosols have relatively small single-scattering albedo due to the large fraction of black carbon emitted from incomplete combustion. The standard deviations of single-

scattering albedo for urban-industrial aerosol and mineral dust are also important. For all major types, uncertainties for single-scattering albedo are ±0.01 ~ ±0.03. For asymmetry factor, uncertainties are ±0.03 ~ ±0.08 for pollution and biomass burning aerosol and ±0.04 for dust. These uncertainties generally transform to aerosol forcing uncertainties of ~15-20% at the TOA and ~10% at the surface. Uncertainties are larger for a dust single-scattering albedo over a highly reflective surface (albedo ~ 0.3-0.35). The interaction of dust absorption with high surface reflection magnifies the aerosol forcing uncertainties to ~ 60% at the TOA and ~20% at the surface. However, the magnitude of TOA forcing in this case is relatively small and so the absolute uncertainty may not be large.

AERONET aerosol optical properties at the four wavelengths are linearly interpolated or extrapolated to the radiation model spectral divisions. The single-scattering albedo, asymmetry factor and Angstrom exponent at wavelengths longer than 1020 nm are taken as the observed values at 1020 nm. The spectral single-scattering albedo of polluted aerosol with a certain amount of soot drops rapidly at around 2000 nm [Hess et al., 1998]. We conducted a sensitivity study that decreased single-scattering albedo to 0.2 at 1900 nm and beyond, and found that the introduced uncertainty in solar radiative effect is within 8% at the TOA and 3% at the surface. A factor 2 of change in the Angstrom exponent at wavelengths beyond 1020 nm would lead to an uncertainty less than 5%. The radiation model [Fu and Liou, 1993] simplifies the phase function by use of an asymmetry factor. Such simplification might introduce large errors (up to 20%) in aerosol forcing calculation, depending on solar zenith angle, aerosol size distribution and refractive index [Boucher, 1998]. However, it is problematic to estimate the overall uncertainty because of a lack of knowledge about possible correlations between

individual uncertainties. We might take 20% as a rough estimate in that this term is expected to dominate over the 5% and 8% terms. Our sensitivity tests also show that using aerosol properties in the visible only would overestimate the aerosol solar radiative effect by about 20% at the TOA and 10% at the surface.

We analyze the AERONET annual aerosol climatology for each of total 203 sites for distinct aerosol regimes (Figure 2.3). The major types distinguished here include biomass burning, dust, industrial pollution as listed in Table 2. Table 2 also lists the selected AERONET sites with a complete and reasonable annual cycle that we could use to represent regions influenced by those distinct aerosol types. Figure 2.4 shows the corresponding optical properties, including mean values, which is the average over time and selected sites for each category, and standard deviations.

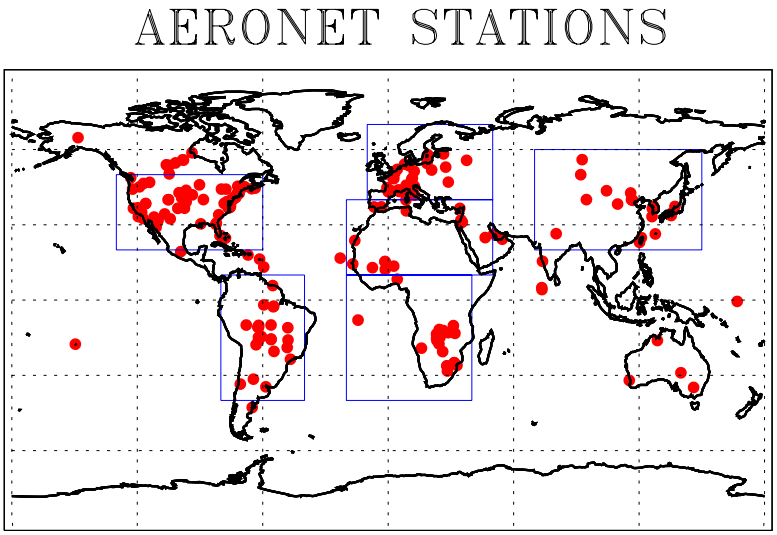

Figure 2.3 Global distribution of AEROsol Robotic Network (AERONET) stations (red dots) and six aggregated geographical regions (blue boxes) including North America, South America, west Europe, North Africa, South Africa and east Asia (from left to right, from above to below).

Table 2.2 Selected AERONET stations for stratifying the data into different aerosol types and geographical regions.

Aerosol types	Regions	AERONET stations
Biomass burning	South America	Alta_Floresta
	South Africa	Mongu and Skukuza
Mineral dust	Albedo < 0.1	Capo_verde and Baharain
	Albedo ~ 0.2	Ilorin and Nes_Ziona
	Albedo 0.3 ~ 0.35	Banizoumbou, SEDE_BOKER, Solar_Village
Pollution	North America	COVE, GSFC, MD_Science_Center, Oyster, SERC, Stennis, Wallops
	West Europe	Ispra, Lille, Moldova and Venise
	East Asia	Anmyon, NCU_Taiwan, Shirahama

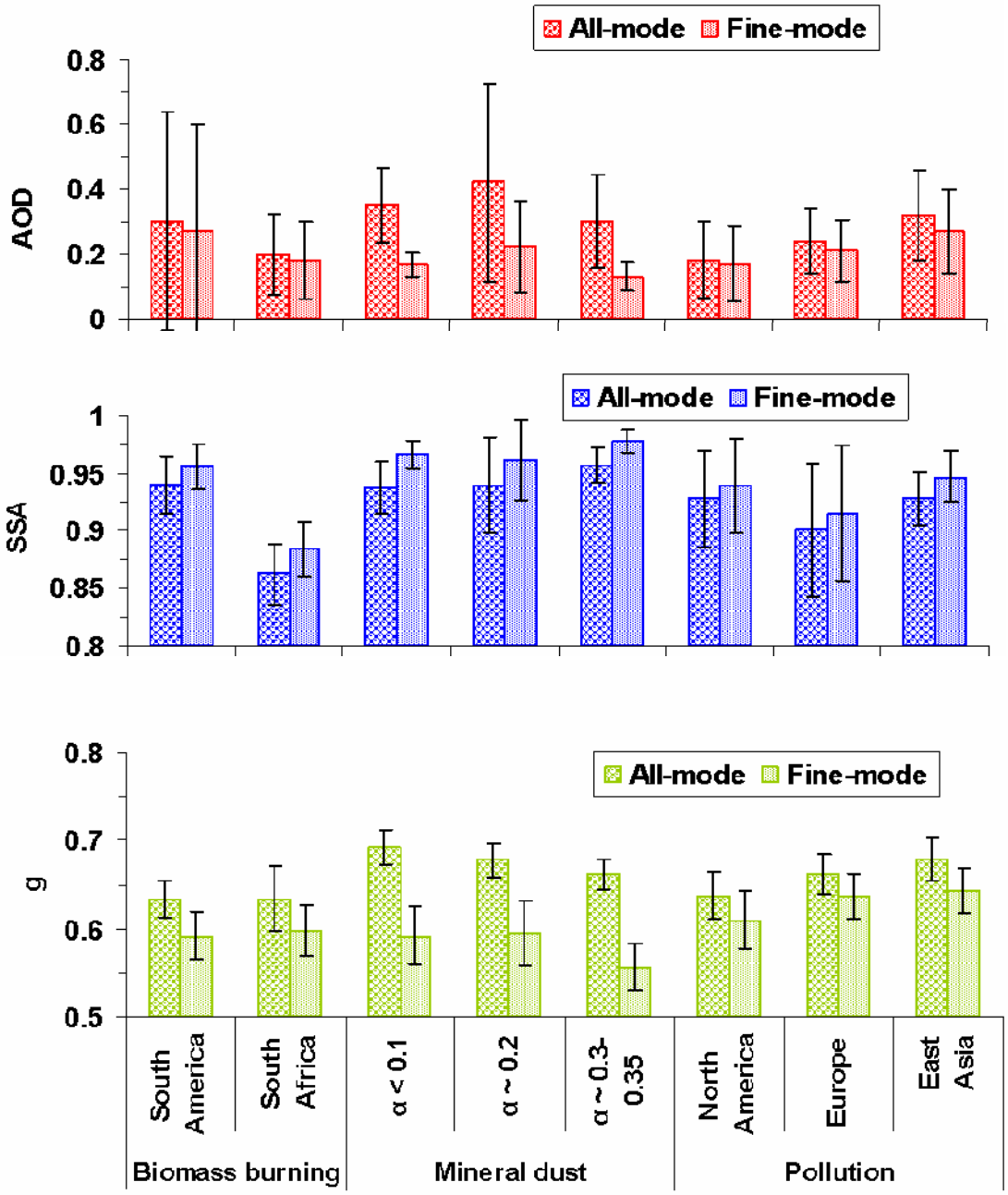

Figure 2.4 Mean values and standard deviations of aerosol optical depth (AOD), single-scattering albedo (SSA) and asymmetry factor (g) at 550 nm for typical aerosol types and over different geographical regions, where α is surface albedo. Standard deviation is shown as the error bar.

2.2.2 Integrated MODIS and GOCART Aerosol Optical Properties over North Africa and the Arabian Peninsula

MODIS is acquiring aerosol optical depths with nearly global coverage; however, MODIS retrievals are not appropriate over the high reflective land surfaces. Models remain a powerful tool to simulate aerosol optical properties. The GOCART model is a three-dimensional chemical transport model. It accounts for major aerosol components, including sulfate, organic carbon, black carbon, mineral dust, and sea-salt based on the prescribed size distribution, refractive index, and hygroscopic growth [Chin et al., 2002]. It can provide a spatial and temporal distribution of aerosol information and fill the gaps of the satellite retrieval, but it has uncertainties in describing various processes of source, sink and mixing. Data assimilation provides an optimal estimate of aerosol distributions by combining different datasets with weights inversely proportional to the square of their errors based on the assumption that the errors are Gaussian and unbiased. An integrated description of MODIS and GOCART aerosol optical depth [Yu et al., 2003] generates a global distribution of aerosols and compares to in-situ measurements better than does either MODIS retrieval or GOCART simulation alone.

Specifically, the following discussion focuses on the region of North Africa and the Arabian Peninsula (20˚W ~ 50˚E and 10˚N ~ 40˚N). The aerosol optical depth at wavelength of 550nm is obtained from integrating MODIS retrieval and GOGART model simulation. Figure 2.5 compares the annual cycle of MODIS, GOCAT and assimilated aerosol optical depth with the AERONET aerosol climatology at selected sites with a complete annual cycle and over our study region. The AERONET aerosol climatology is used for comparison in place of that for year 2001 because of the

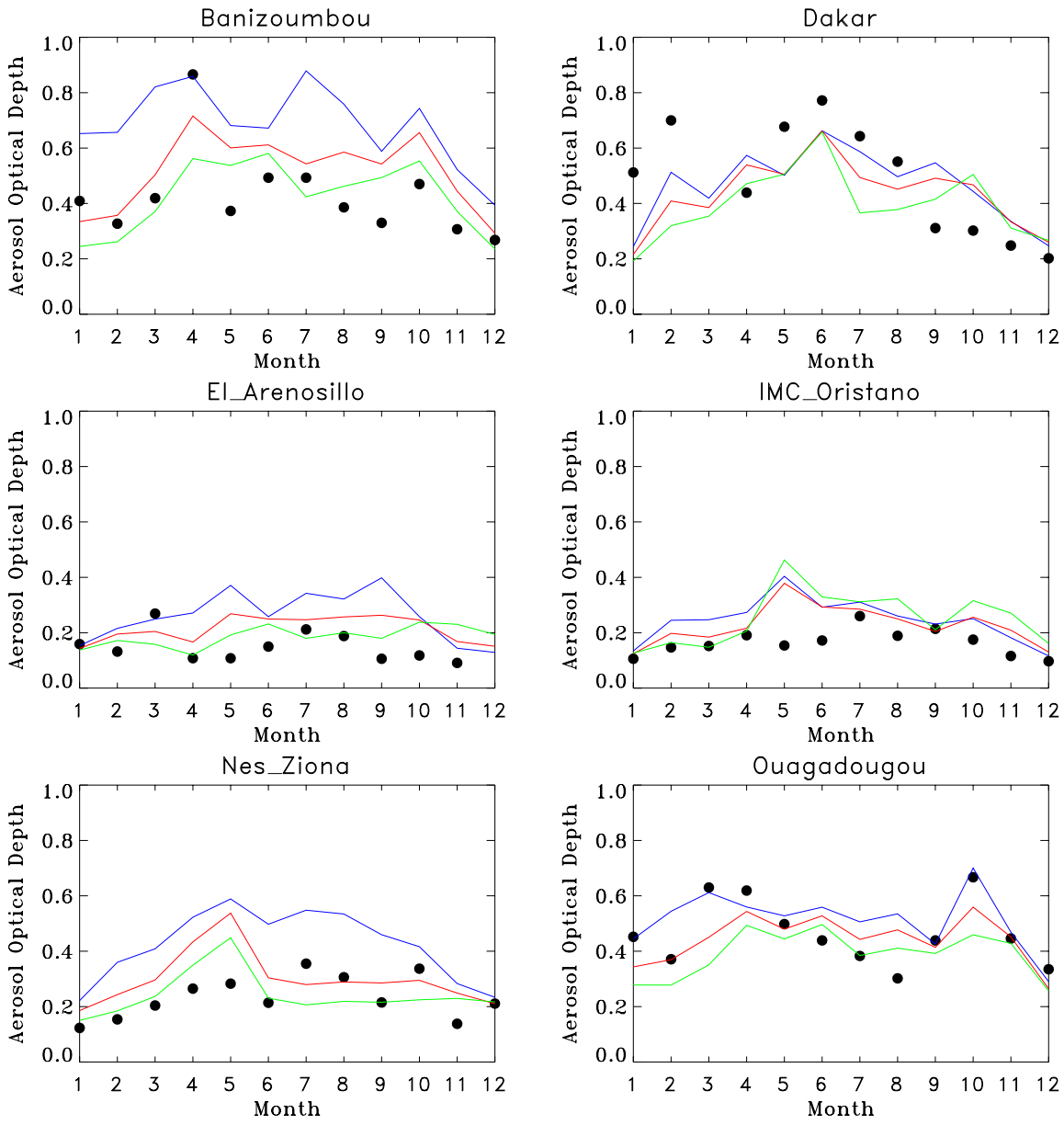

Figure 2.5 Comparisons of the annual cycle of the MODIS (blue line), GOCART (green line) and assimilated (red line) aerosol optical depths with the AERONET aerosol climatology (black dots) at 6 selected sites over North Africa and the Arabian Peninsula.

incomplete annual cycle during 2001. GOCART modeling is the primary contributor to the aerosol estimation in our study region since the MODIS retrieval has difficulties over reflective arid surfaces. Generally, MODIS tends to overestimate and GOCART to underestimate the aerosol optical depth in comparison with the AERONET measurements. The assimilated MODIS and GOCART aerosol optical depths lie in between the individual estimates and agrees better with AERONET measurements than either alone. On the other hand, the assimilated data have larger values for small aerosol optical depths but smaller values for large aerosol optical depths than those in the AERONET measurements.

Figure 2.6 shows the scatterplots of MODIS, GOCART and assimilated aerosol optical depth versus AERONET aerosol climatology corresponding to those in Figure 2.5. The combined data are better correlated with the AERONET measurements (a correlation coefficient of 0.78) than with MODIS (correlation coefficient ~0.73) or GOCART (correlation coefficient ~0.69). The correlation is further analyzed by linear regressions of binned aerosol optical depth of MODIS, GOCART and assimilated data based on that of AERONET aerosol climatology (Figure 2.7). A bin size of 0.04 is chosen. The red lines represent the linear fits of averages (solid) and standard deviations (dotted). The data assimilation reduces the offset of linear fit and the standard deviation. However, there still exist high bias at low optical depth level and low bias at high optical depth level. Possible explanations include interannual variability of aerosol optical depth and scaling problems between site-to-grid comparisons.

The other spectral optical parameters, including Angstrom exponent, single-scattering albedo and asymmetry factor, are derived from GOCART simulations, and an

external mixing is assumed to derive single-scattering albedo [Chin et al., 2002, Yu et al., 2003]. The aerosol optical parameters are mapped to a T42 climate model grid. Figure 2.8 illustrates the optical depth and Angstrom exponent at 550nm wavelength in summer (average of June-August). The optical depth is always larger than 0.3 with highest value of about 0.8 in the west of the Sahara desert. The small Angstrom exponent suggests dust dominates over most areas. The Northeast sector of the domain is likely influenced by Eurasian pollution, as inferred from the Angstrom exponent that is larger than 1. The single-scattering albedo at 550nm is ~ 0.9 over the dust-dominant area and ~ 0.88 in the northeastern region. Note that the GOCART modeled dust absorption is substantially stronger than that of the AERONET measurement with a mean single-scattering albedo of 0.94 ~ 0.95 shown in Figure 2.4. The discrepancy probably results from a lack of consideration of the mixing mechanism of hematite (iron oxide) in the model dust absorption computations [Dubovik et al., 2002].

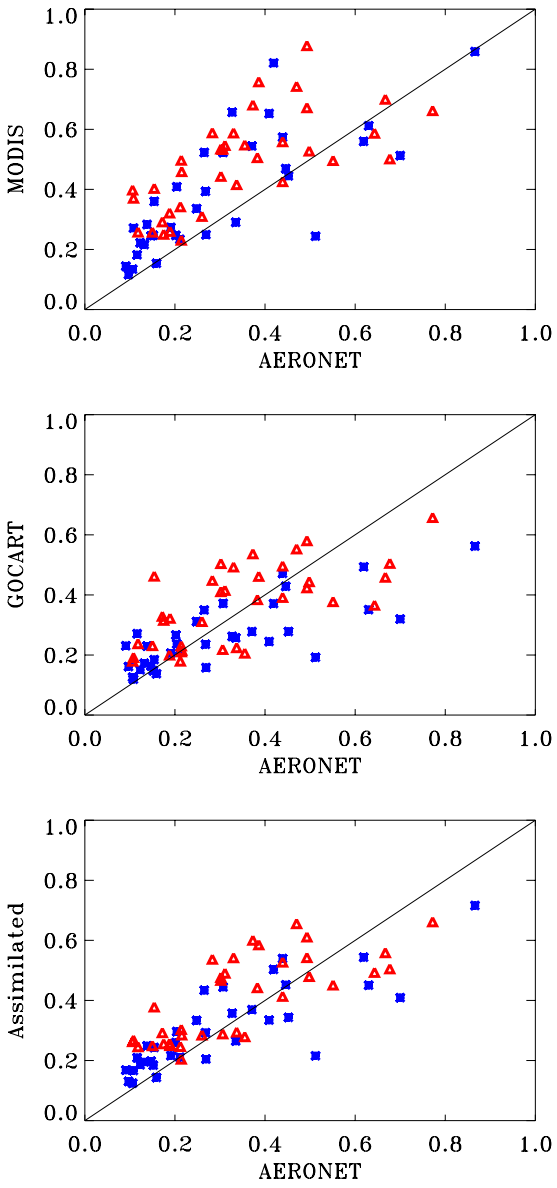

Figure 2.6 Scatterplots of MODIS, GOCART and assimilated aerosol optical depth versus AERONET measurements with correlation coefficients of 0.73, 0.69 and 0.78 respectively. Blue cross and red triangle represents winter and summer respectively. Solid line is 1:1 relationship.

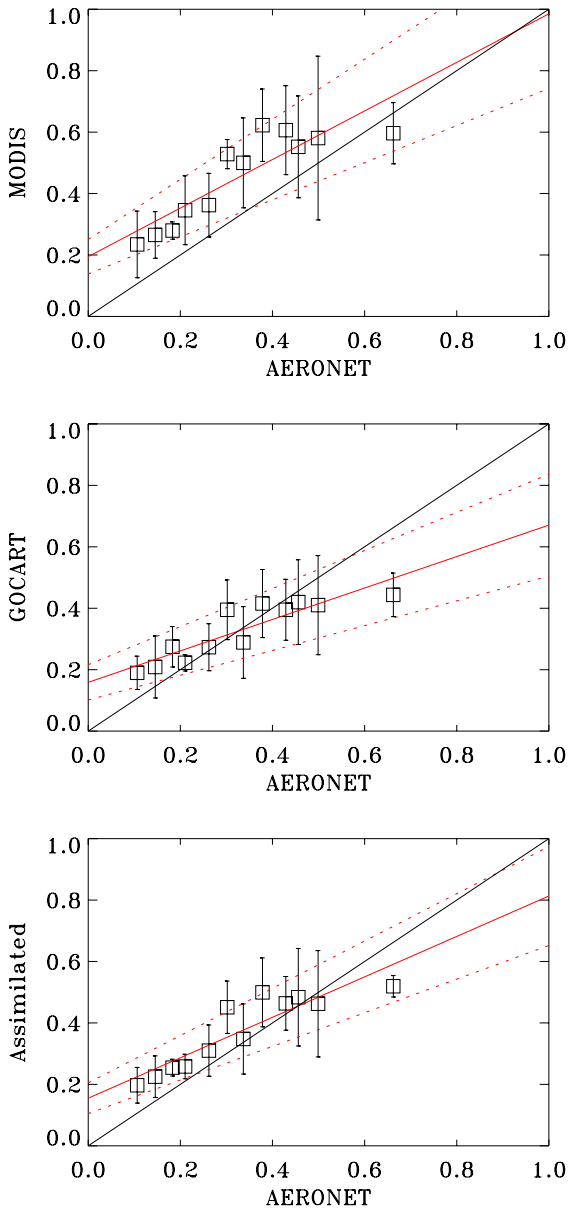

Figure 2.7 Linear regression of binned aerosol optical depth of MODIS, GOCART and assimilated data versus AERONET measurements with bin size of 0.04. Red solid/dotted line represents a linear fit of average/standard deviation. Solid black line is 1:1 relationship.

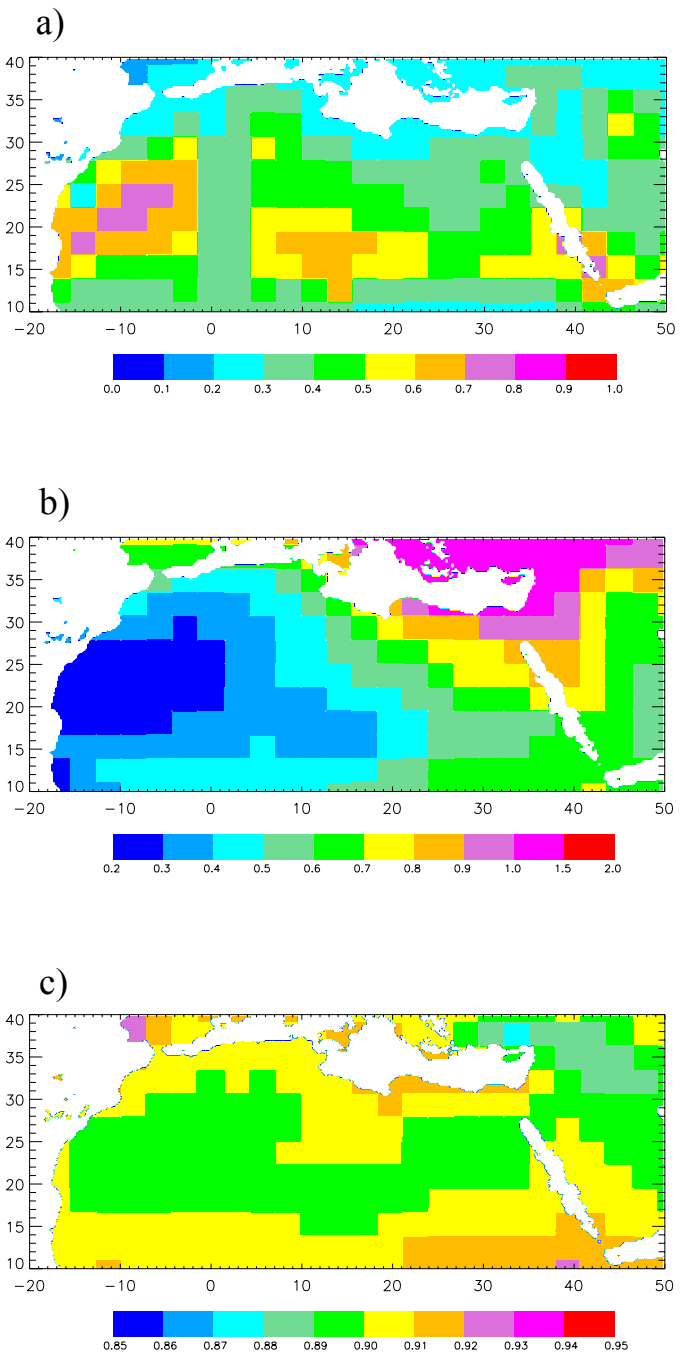

Figure 2.8 Aerosol optical properties over Northern Africa and the Arabian Peninsula (20˚W ~ 50˚E, 10˚N ~ 40˚N) for summer 2001: a) Optical depth, b) Angstrom exponent, c) Single-scattering albedo.

2.2.3 MODIS Land Surface Albedo and Cloud Properties

A calculation of the aerosol direct radiative effect requires information on surface albedo and clouds such as those obtained from MODIS retrievals. MODIS provides the remotely sensed cloud-free land surface albedo for both direct (black-sky) and diffuse (white-sky) radiation at 1-km resolution for every 16-day period. We use the version 4 MOD43C1 MODIS white-sky albedo data for year 2001 and for seven MODIS spectral bands and three broadbands (0.3~0.7, 0.7~4.0 and 0.3~4.0μm) [Schaaf et al., 2002]. The solar zenith angle dependence of land albedo are thus not considered. Yu et al. [2004] accounts for the angular dependence of surface albedo by black-sky and white-sky albedo simply weighted with the direct-beam fraction and diffuse-light fraction, respectively. Because of change of the direct beam fraction by aerosols, the calculated surface reflection with the presence of aerosol is different from that without aerosol, contributing to the aerosol direct effect at the TOA. They concluded that the neglect of angular dependence of surface albedo will introduce an uncertainty that is small (i.e., less than 5%) for monthly and global average but can be more significant for the diurnal cycle of aerosol TOA forcing.

MODIS land albedo shows good agreement and reasonable consistency compared with the available field measurements, Clouds and Earth's Radiant Energy System (CERES) TOA albedo and historical global albedos from advanced very high resolution radiometer (AVHRR) and Earth Radiation Budget Experiment (ERBE) experiment [Jin et al., 2003]. In comparison to ground-based albedometer measurements over semi-desert region, it is shown that MODIS albedo has accuracy of ±0.05 and mostly close to ±0.02 [Lucht et al., 2000]. Given the ±0.05 uncertainty in surface albedo, an uncertainty in dust

forcing is inferred of ~40% at the TOA and ~10% at the surface over a semi-desert region with albedo ~0.3-0.35. Please note again that the TOA forcing in this case is relatively small in magnitude and so the absolute uncertainty may not be large. The uncertainties in aerosol forcing associated with MODIS albedo are expected to be much smaller for most other regions because semi-desert regions have relatively large albedo values. For example, a ±0.05 change in albedo from ~0.2 only introduces a dust forcing change of ~ 15% at the TOA and ~5% at the surface. The near-infrared broadband albedo is an adequate specification for soil. However, it underestimates average grass albedo over 0.7-1.3 μm by about 10% due to a sharp drop in albedo at around 1.3 μm as shown in Figure 2.9. The associated overestimation in aerosol direct effect is <7% at the TOA and <2% at the surface for grassland but can be larger for a snow-covered surface. Therefore, a more detailed spectral surface albedo may be needed to better characterize the aerosol effect over vegetation and snow.

The global distribution of MODIS land surface albedo (Figure 2.10) shows extremely high visible broadband albedos, as large as 0.8, occur at snow-covered high latitudes. The next highest albedo is about 0.2-0.3 over the desert of the Saharan and Arabian Peninsula. The near-infrared broadband albedo has a similar distribution, with the highest of 0.4 over snow, and 0.3-0.4 over desert with dry soil. The seasonal variation of surface albedo is generally small except over snow-covered areas, where the surface albedo increases dramatically from summer to winter [Zhou et al., 2003].

The daytime file of MODIS/Terra level 3 monthly 1˚×1˚ cloud products (MOD08M3) is used in the study, including water cloud optical depth, ice cloud optical depth, and cloud fraction for year 2001 [King et al., 2003; Platnick et al., 2003]. It

represents the atmospheric state at local time 10:30am. There are also MODIS/Aqua cloud data (MYD08M3) representing the state at 1:30pm. Differences between these two may suggest part of diurnal variations. In our sensitivity tests, we don't account for such diurnal variations. An effective radius is assumed to be 10 μm for water cloud and 50 μm for ice cloud [Liao and Seinfeld, 1998; Fu and Liou, 1993]. The radiative effect of aerosol under cloudy skies is sensitive to the relative vertical distributions of aerosols and cloud layer; however no such information is provided from MODIS. Sensitivity studies are carried out and discussed in Section 2.3.4.

Over ocean, the increase of surface albedo with solar zenith angle is accounted for by a look-up table that is generated by a coupled atmosphere-ocean radiative transfer model [Jin et al., 2002; 2004]. The dependence of albedo on wind speed and chlorophyll concentration is not considered. This assumption introduces a relatively small uncertainty (less than 10%) in the diurnal average of aerosol solar effect because a change of chlorophyll concentration from 0 to 10 mg m^{-3} only changes the broadband ocean albedo by less than 0.005 and the increasing ocean albedo with wind speed depends on solar zenith angle [Yu et al., 2004].

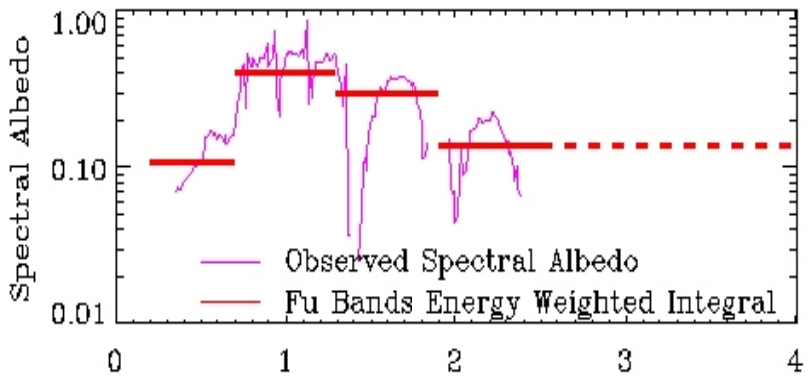

Figure 2.9 Oklahoma spectral albedo for grass at solar zenith angle of 60˚ (from *http://www-surf.larc.nasa.gov/surf/pages/explan.html*).

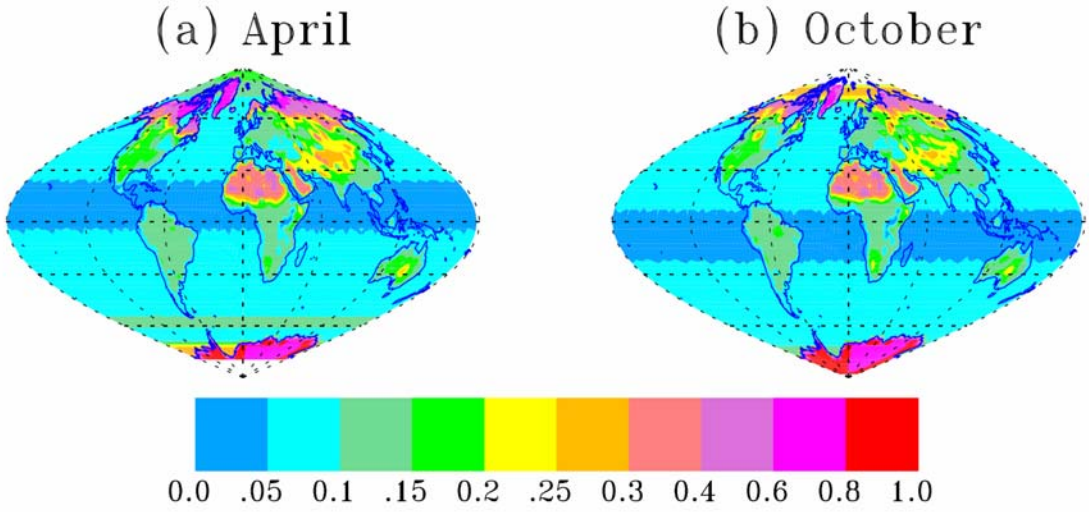

Figure 2.10 Global distribution of spectrally integrated monthly average MODIS land surface albedo (a) April and (b) October (Yu et al., 2004).

2.3 A Normalized Description of the Aerosol Direct Radiative Effect for Distinct Aerosol Regimes

2.3.1 Introduction to Normalized Aerosol Direct Radiative Effect (NADRE)

In this part, the AERONET aerosol climatology, visible (0.3~0.7 μm) and near-infrared (0.7~4.0 μm) broadband surface albedo and cloud properties derived from MODIS are used as inputs for the radiative transfer model to calculate the net solar fluxes at both the TOA and surface [Zhou et al., 2005]. The model is run over a 24-hour diurnal cycle with solar insolation of the 15th day of each month to provide a monthly average. To facilitate discussion, we define the NADRE as the normalized aerosol direct radiative effect divided by the optical depth at 550 nm (the average value of observed optical depth at 440 and 670 nm) at both the TOA and surface. By doing so, we remove much of the influence of aerosol loading and so see more clearly how the aerosol direct radiative effect (ADRE) can be impacted by the internal aerosol optical properties. For a specific type of aerosol, its particle size distribution, chemical composition and shape determine the internal aerosol optical properties, including the wavelength dependence of optical depth, single-scattering albedo, and asymmetry factor; however there can be large variability in aerosol radiative effect even under the same geographical conditions, because of large variations of aerosol optical depth with time [Anderson et al., 2003b]. The relatively large spread in optical depth shown in Figure 2.4 illustrates its large spatial and temporal variation. Thus, it is necessary to look at the NADRE to see dependences on other aerosol optical properties. Such can flexibly serve as a baseline to evaluate estimates of aerosol direct radiative forcing using satellite observations, model simulations, and their combinations [Boucher and Tanre, 2000; Chou et al., 2002; Yu et al., 2004; Zhang et al., 2005 ; Yu et al., 2006].

The calculated NADRE must be used with caution when extrapolating or comparing to other studies, because the ADRE is a nonlinear function of aerosol optical depth. The NADRE decreases with optical depth at high solar zenith angle and increases at low solar zenith angle, therefore its dependence on optical depth is partially canceled out when averaging over solar zenith angle. For a suface albedo of 0.15 and single-scattering albedo of 0.95, because of the nonlinearity, an increase of 0.25 in optical depth would decrease the 0˚-90˚ solar-zenith-angle-averaged clear-sky NADRE by 7% at the TOA and 3% at the surface. For a single-scattering albedo of 0.8, the 0˚-90˚ solar-zenith-angle-averaged clear-sky NADRE is changed by a very small value at the TOA and 5% at the surface (Figure 2.11). The distribution of solar zenith angle at a certain location depends on the latitude and season, hence the change in clear-sky NADRE with aerosol optical depth can be larger at high latitudes or in the winter season. The relative error in average aerosol direct effect derived from average NADRE and average optical depth is generally less than 7% for categories listed in Table 2 except for South America Biomass burning, which is limited by lack of data (only one selected site) and so has a much larger variation in optical depth than others. The relationship of aerosol direct effect with optical depth becomes more linear when clouds are present, probably resulting from in-cloud multi-scattering.

Under clear skies, the vertical distribution of absorbing aerosols is important for calculating backscattered UV. However, it becomes unimportant over the whole solar spectrum even for absorbing aerosols. Thus, we assume a well-mixed profile within the lowest 2 km layer. Under cloudy skies, on the other hand, the radiative effect of aerosol

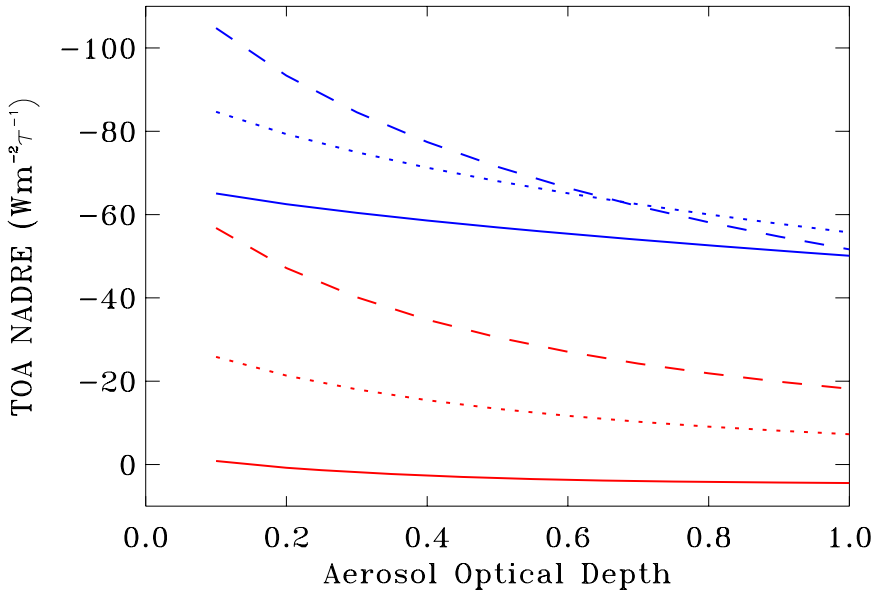

Figure 2.11 Solar-zenith-angle-averaged clear-sky normalized aerosol direct radiative effect (NADRE, unit: $Wm^{-2}\tau^{-1}$) changes with aerosol optical depth at the TOA for single-scattering albedo of 0.95 (blue) and 0.8 (red) respectively, and over different solar zenith angle distributions of 0˚-90˚ (solid line), 30˚-90˚ (dotted line) and 60˚-90˚ (dashed line).

depends highly on the relative distributions of aerosols and cloud layer in the vertical [Liao and Seinfeld, 1998; Keil and Haywood, 2003]. Because MODIS doesn't provide such information, sensitivity tests have been carried out by using two idealized aerosol-cloud profiles to examine the sensitivity of the aerosol direct effect to aerosol-cloud distributions. In either case, ice clouds are assumed to stay above the aerosol layer. In one test, denoted as the *below-cloud* case, we assume that the water cloud is completely above the aerosol layer. In the other test denoted as the *within-cloud* case, 50% of aerosol extinction is assumed below the water cloud and the remaining is above the water cloud. In two cases, the columnar optical depth of aerosol is the same. The MODIS cloud fraction (f_{cld}) is used to weigh aerosol cloudy-sky NADRE (NADRE_cld) and clear-sky NADRE (NADRE_clr) to generate all-sky NADRE (NADRE_all), as follows:

$$\text{NADRE\_all} = f_{cld} * \text{NADRE\_cld} + (1-f_{cld}) * \text{NADRE\_clr} \quad (2.1a)$$

or

$$\text{NADRE\_all} / \text{NADRE\_clr} = f_{cld} * \text{NADRE\_cld} / \text{NADRE\_clr} + (1-f_{cld}) \quad (2.1b)$$

Equation (2.1b) suggests that all-sky to clear-sky NADRE can be larger, equal to, or smaller than the clear-sky fraction ($1-f_{cld}$), depending on aerosol and cloud properties that determine the sign and value of cloudy-sky NADRE.

The radiative calculations have been conducted for each of the 203 AERONET sites with annual aerosol climatology. The so-derived climatology of monthly aerosol direct radiative effects can serve as a baseline product to evaluate the assessment of aerosol radiative effect based on satellite retrievals, model simulations or an integration of satellite and modeling [Boucher and Tanre, 2000; Chou et al., 2002; Yu et al., 2004; Zhang et al., 2005, Yu et al., 2006]. The following discussion will focus on comparisons

of aerosol radiative effects between different aerosol types (e.g., biomass burning, mineral dust, and pollution), geographical locations (South America, South Africa, North America, West Europe, and East Asia), and surface properties (e.g., large variations of surface albedo in Saharan deserts and Arabian peninsula), as listed in Table 2.

2.3.2 Cloud-free NADRE by All-mode Aerosol

Clear-sky aerosol forcing is determined by geographically varying aerosol optical properties and geophysical parameters, such as surface albedo. Such variations are illustrated in the following through discussion of major aerosol types using the categories listed in Table 2. Mean values with standard deviations for the NADRE at the TOA and surface are shown in Figure 2.14, where standard deviations represent monthly and spatial variations in NADRE. Also shown in Figure 2.14 is the NADRE for fine-mode aerosols, which will be discussed in Section 2.3.3.

2.3.2.1 Biomass Burning Aerosols

Biomass burning occurs mainly in South Africa and South America during the dry season (August-November), and in the Africa savanna region during January-March [Delmas et al., 1991], and occasionally in mid-high latitude boreal forest over July-August. The Alta_Floresta site is chosen as the representative of biomass burning aerosol, which is located in the Amazon basin of South America. Figure 2.12 shows the annual cycle of aerosol optical properties, surface albedo, aerosol direct radiative effect (ADRE) and its normalized form NADRE for all-mode in blue and fine-mode in red. The fine-mode part will be discussed in Section 2.3.3. For all-mode aerosol, optical depths at 550nm are lower than 0.2 except from August to November, corresponding to seasonality

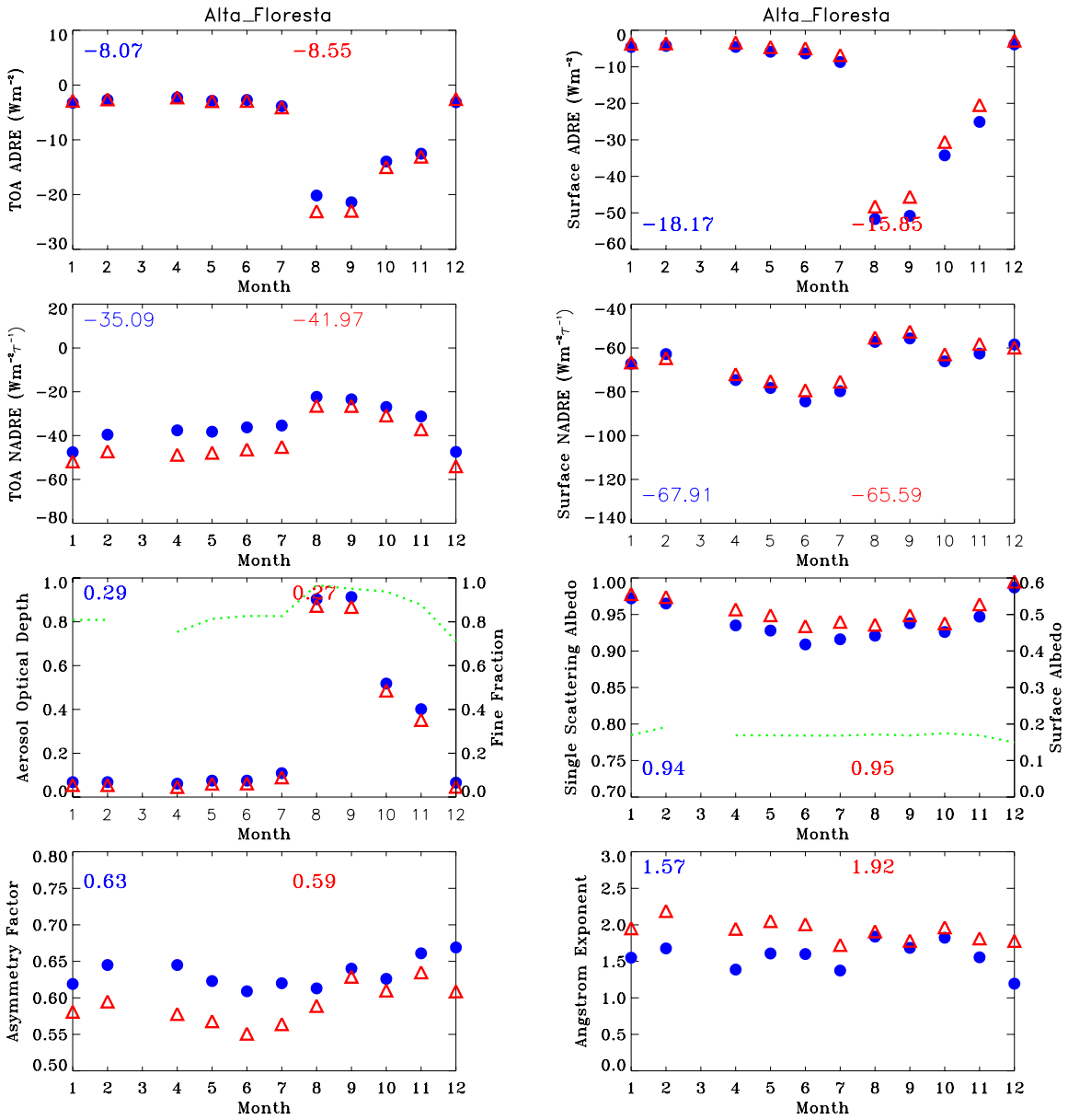

Figure 2.12 South America biomass burning aerosol climatology at 550nm, aerosol direct radiative effect (ADRE) and its normalized form (NADRE) for all-mode (blue) and fine-mode (red) at site Alta_Floresta. Numbers in each panel are mean values. Green lines refer to left axis for fine-mode fraction and surface albedo.

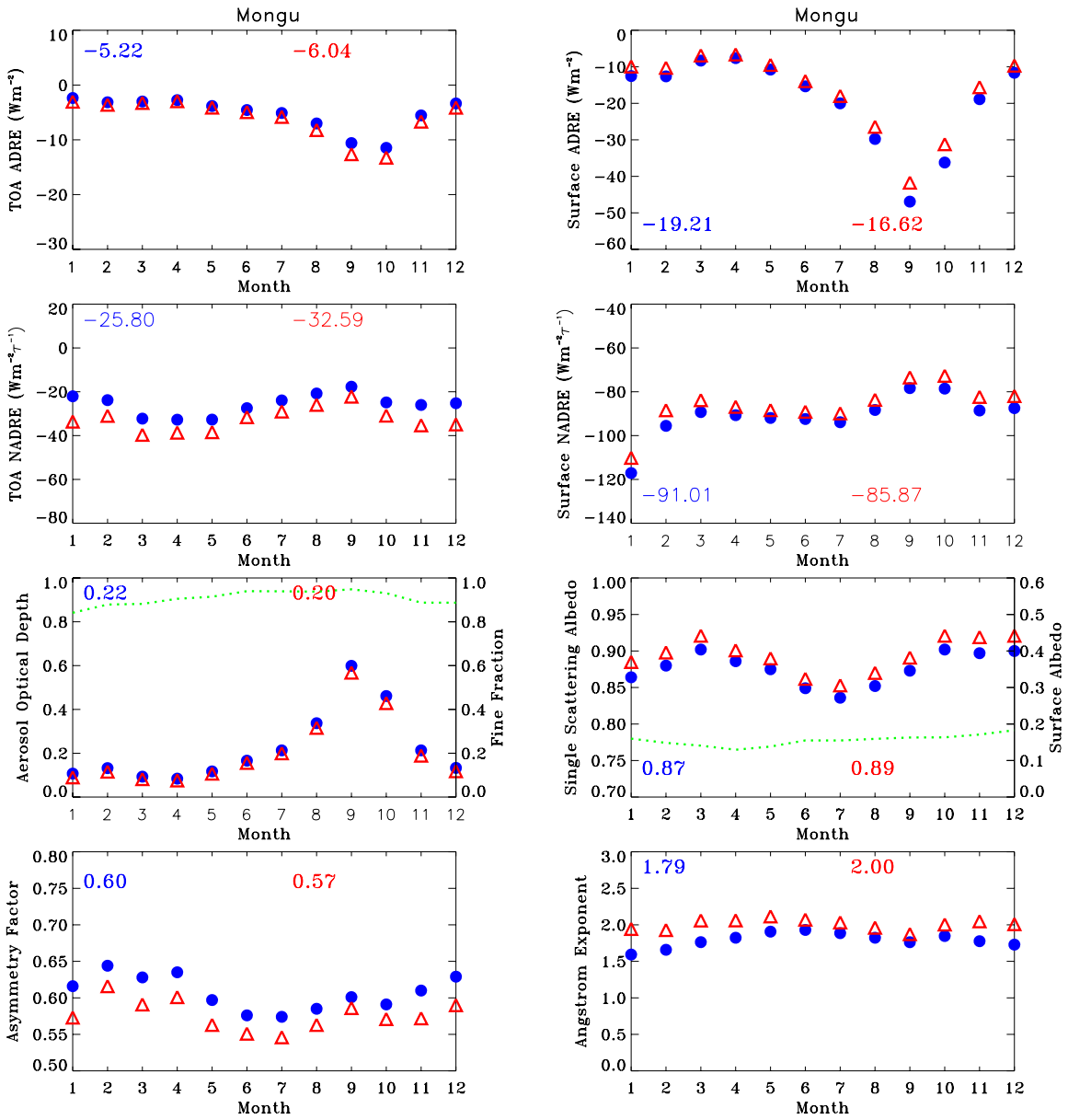

Figure 2.13 South Africa biomass burning aerosol climatology at 550nm, aerosol direct radiative effect (ADRE) and its normalized form (NADRE) for all-mode (blue) and fine-mode (red) at site Mongu. Numbers in each panel are mean values. Green lines refer to left axis for fine-mode fraction and surface albedo.

of biomass burning. The average single-scattering albedo, asymmetry factor and Angstrom exponent are about 0.94, 0.63 and 1.57 respectively. During the burning season, aerosols cool the TOA by 10 ~ 20 Wm^{-2} and the seasonality of TOA and surface ADRE is mainly caused by a seasonal variation of aerosol. Surface cooling is about double of TOA cooling due to the compensation of positive atmosphere heating and negative surface cooling

The Mongu site is chosen as the representative of South Africa biomass burning aerosol as shown in Figure 2.13. Again optical depths at 550nm are larger than 0.2 from July to November because of biomass burning. The main difference of biomass burning aerosol over South Africa from South America is the stronger absorption with lower single-scattering albedo. As seen in Figure 2.12 and 2.13, the average single-scattering albedos at Alta_Floresta and Mongu are 0.94 and 0.87, respectively. Such strong absorption makes the surface cooling to be about three times of TOA cooling resulting from the large atmosphere heating.

The statistics of NADRE under clear-sky are shown in Figure 2.14. Single-scattering albedo of biomass burning smoke varies significantly with different black carbon content due to different aging processes, source and meteorological characteristics [Dubovik et al., 2002; Eck et al., 2003]. A much stronger absorption is observed for African savanna fires than for Amazonian forest fires [Dubovik et al., 2002; Eck et al., 2004]. As shown in Figure 2.14, the average single-scattering albedo at 550 nm is 0.940±0.025 in South America, compared to 0.862±0.027 in South Africa, according to the data presented in this study. Such differences in smoke absorption result in different NADREs because aerosol absorption reduces the upscattering component at the TOA

(i.e., a smaller TOA cooling) and absorbs solar energy in the atmosphere that otherwise can reach the surface (i.e., a larger surface cooling). On average, the NADRE in South America is larger at the TOA by 35% (more negative) and smaller at the surface by 38% (less negative) than those in South Africa. As shown in Figure 2.15, the ratio of TOA to surface NADRE generally decreases with a decrease of aerosol single-scattering albedo, and so readily separates biomass burning aerosol in South Africa (red dots) from South America (blue dots); thus it provides an alternative to single-scattering albedo for such distinction. In South America, the TOA to surface NADRE ratio decreases from about 0.81 to 0.39 with single-scattering albedo ranging from 0.99 to 0.91. In South Africa, the single-scattering albedo ranges from 0.90 to 0.81 and the corresponding TOA to surface NADRE ratio ranges from 0.36 to 0.14.

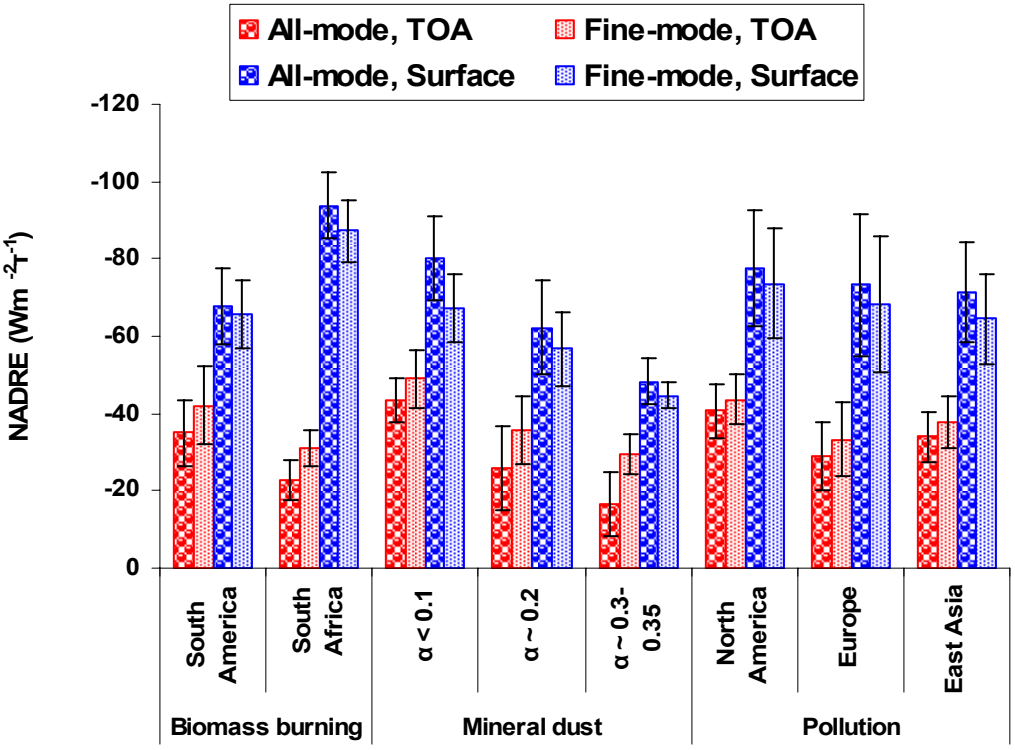

Figure 2.14 Mean values and standard deviations of clear-sky normalized aerosol direct radiative effect (NADRE) at the TOA and surface (unit: $Wm^{-2}\tau^{-1}$) for typical aerosol types and over different geographical regions, where standard deviations represent monthly and spatial variations in NADRE and α is surface albedo.

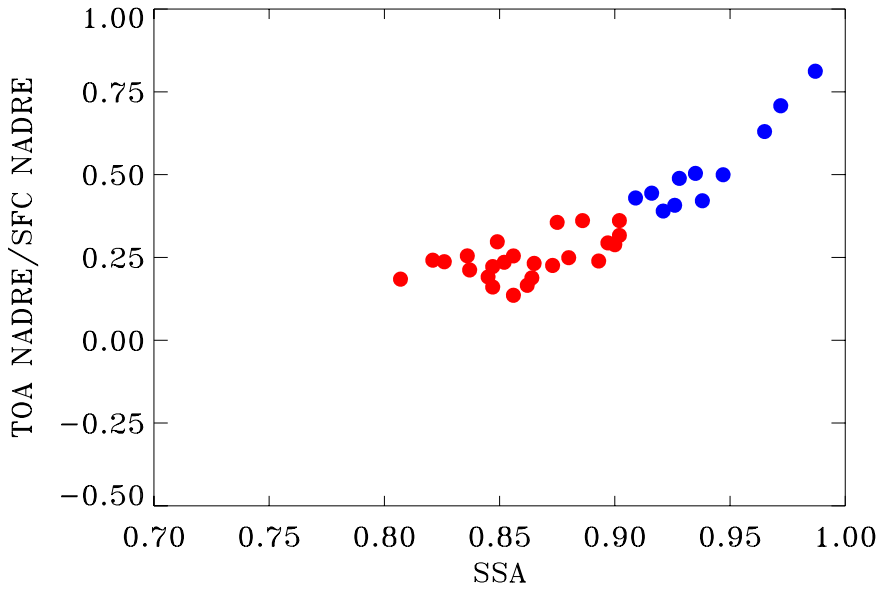

Figure 2.15 The ratio of TOA NADRE to surface (SFC) NADRE decreases with deceasing aerosol single-scattering albedo (SSA) for biomass burning smoke over South America (blue) and over South Africa (red), respectively.

2.3.2.2 Mineral Dust

Mineral dust dominates aerosol radiative effects over North Africa and the Arabian Peninsula where the surface reflectivity is high and has considerable spatial variability, ranging from about 0.2 to 0.4 for broadband albedo [Tsvetsinskaya et al.; 2002]. Dust outflows also substantially influence radiation absorbed by nearby oceans where the surface albedo is less than 0.1. The aerosol climatology at Capo_verde is chosen to represent Saharan dust for surface albedo < 0.1. The annual cycle of optical properties, surface albedo, ADREs and NADREs are shown in Figure 2.16. Again, the fine-mode part will be discussed in Section 2.3.3. The monthly average of optical depth is larger than 0.2 throughout the whole year, along with a typical Angstrom exponent that is below 0.5. The relatively high optical depth and small Angstrom exponent in the summer season suggest that dust from the Saharan deserts dominates over this region. Through the year, the surface albedo is smaller than 0.1. Dust for all-mode has a cooling effect of TOA ADRE by about 10 ~ 30 Wm^{-2} and surface ADRE by about 20 ~ 50 Wm^{-2} with a monthly variation consistent with that of optical depth and single-scattering albedo. The ratio of average values of surface to TOA NADRE is ~ 1.8, which indicates that about half of surface cooling is cancelled out by the atmosphere heating. Large uncertainty exists in dust single-scattering albedo. The average single-scattering albedo is 0.94 in Figure 2.16 but it can be as small as 0.85 [Koepke et al., 1997]. Figure 2.17 shows a site at Ilorin representative of dust and surface albedo ~ 0.2. The average single-scattering albedo of 0.93 is close to that at Capo_verde, but the ratio of average values of surface NADRE to TOA ADRE is ~ 2.5, which is about 44% larger than that at

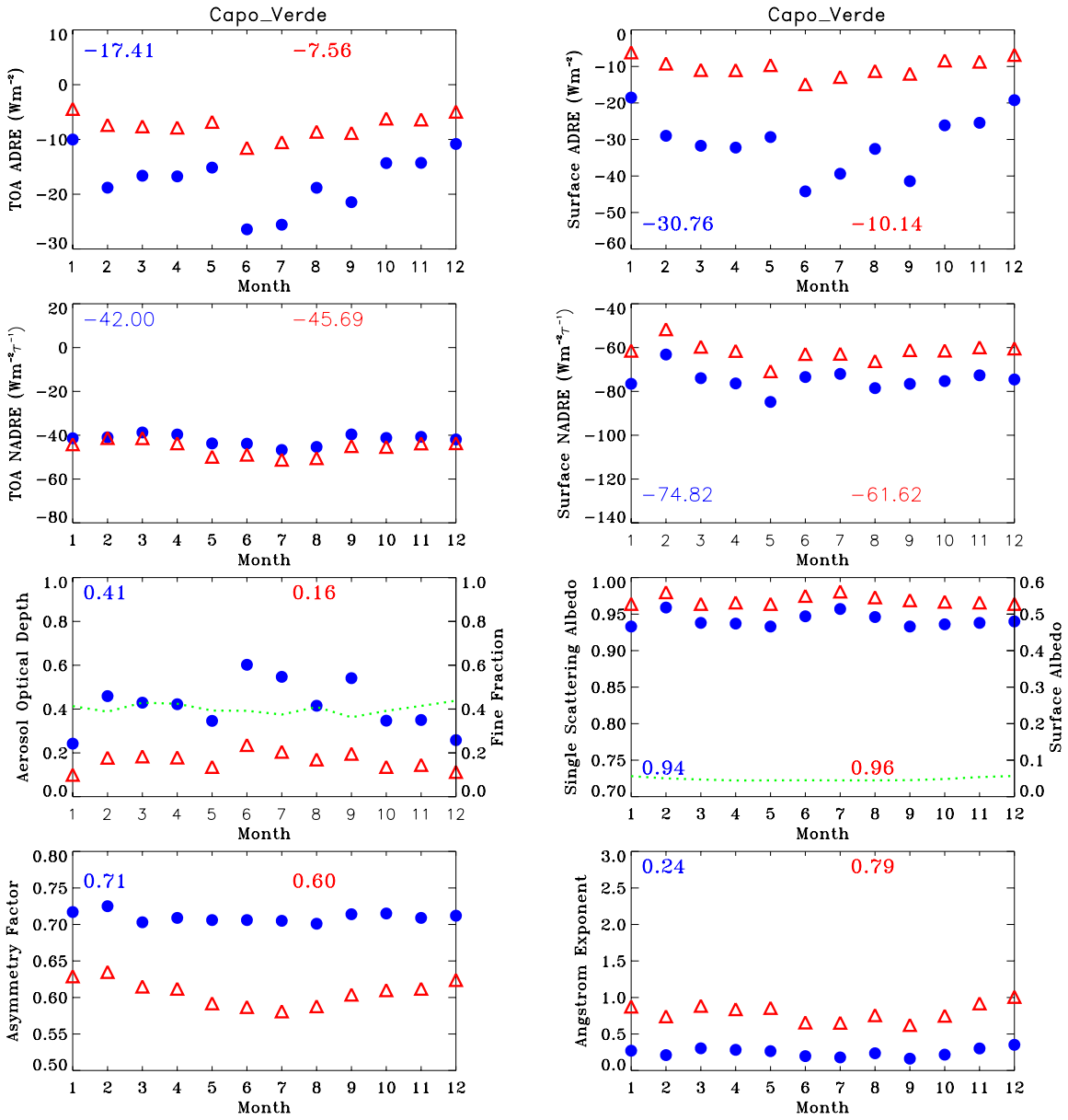

Figure 2.16 Dust aerosol climatology at 550nm, aerosol direct radiative effect (ADRE) and its normalized form (NADRE) for all-mode (blue) and fine-mode (red) at site Capo_verde for surface albedo < 0.1. Numbers in each panel are mean values. Green lines refer to left axis for fine-mode fraction and surface albedo.

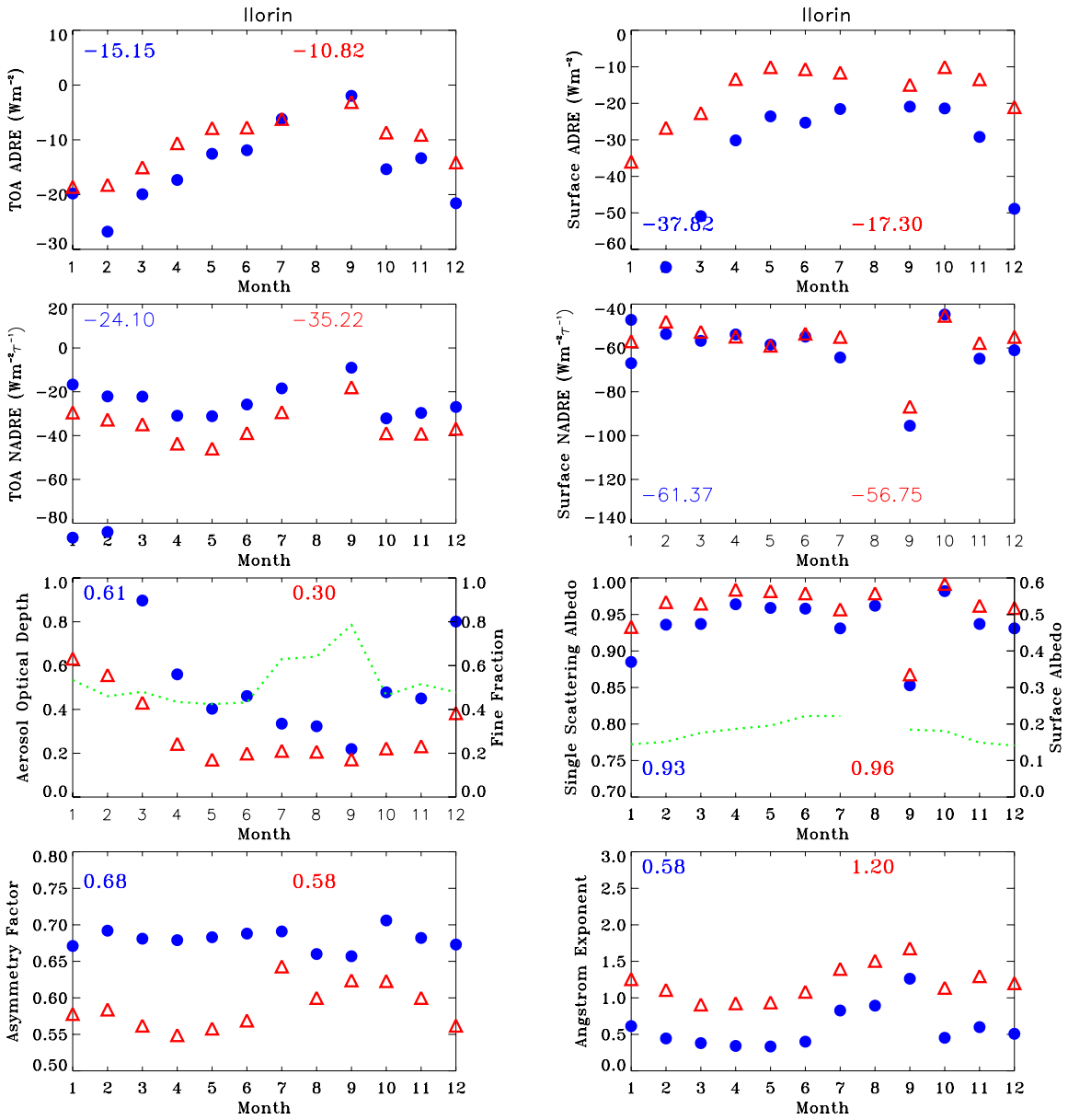

Figure 2.17 Dust aerosol climatology at 550nm, aerosol direct radiative effect (ADRE) and its normalized form (NADRE) for all-mode (blue) and fine-mode (red) at site Ilorin for surface albedo ~ 0.2. Numbers in each panel are mean values. Green lines refer to left axis for fine-mode fraction and surface albedo.

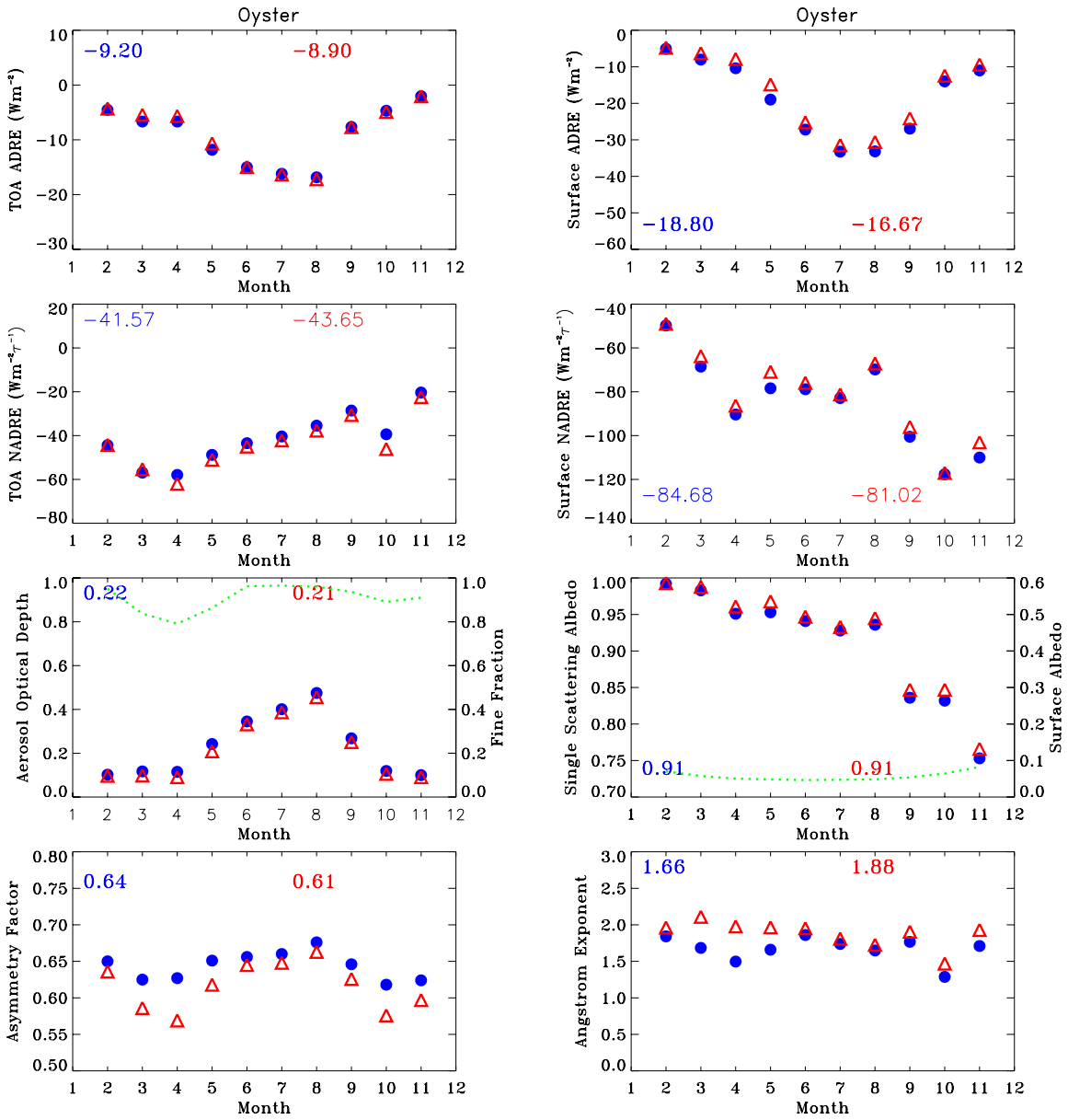

Figure 2.18 Dust aerosol climatology at 550nm, aerosol direct radiative effect (ADRE) and its normalized form (NADRE) for all-mode (blue) and fine-mode (red) at site SEDE_BOKER for surface albedo ~ 0.3-0.35. Numbers in each panel are mean values. Green lines refer to left axis for fine-mode fraction and surface albedo.

Capo_verde. As NADRE is normalized by optical depth, such a difference is mainly determined by the interaction of dust internal optical properties with surface albedo. Results for dust over a surface albedo of ~ 0.3-0.35 are shown in Figure 2.18 with site SEDE_BOKER. Again the increased ratio of average values of surface NADRE to TOA ADRE of 3.6 is a result of the interaction of large surface albedo with dust optical properties.

The large variability of surface albedo significantly influences the ADRE of mineral dust as discussed above, as also shown in Figure 2.14 and Figure 2.19. The net surface solar flux is a product of downward solar flux reaching the surface and (1-α), where α is the surface albedo. As such, with the same aerosol properties and hence the same changes of downward solar flux, the ADRE at the surface decreases with increasing surface albedo. Moreover, aerosols absorb as well as scatter back the surface-reflected solar radiation through multiple reflections between the surface and aerosol layer. As the surface albedo increases, the magnitudes of both TOA and surface NADRE decrease significantly. This trend can easily be seen from the average values in Figure 2.14. Note that climatological differences in aerosol properties over different surfaces also introduce differences in dust solar radiative effect as shown in Figure 2.4. Comparisons of single-scattering albedo and asymmetry factor suggest that aerosol over dark oceans is slightly more absorbing and larger in size than that over the brightest surfaces. Since these differences are relatively small and have compensating effects on aerosol solar radiative effect at the surface, they should not be major factors contributing to the differences illustrated in Figure 2.14. Therefore, we conclude that the much reduced aerosol TOA

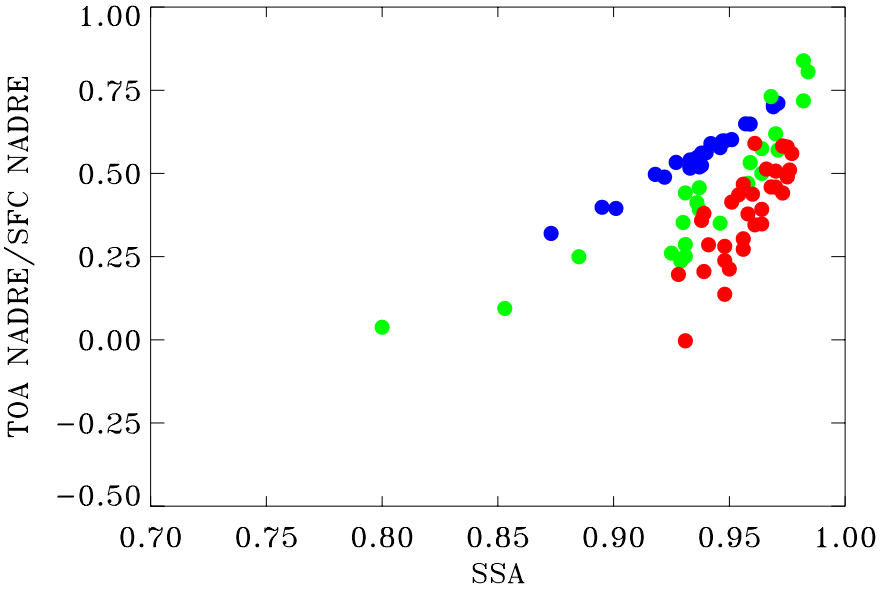

Figure 2.19 The ratio of TOA NADRE to surface (SFC) NADRE decreases with deceasing aerosol single-scattering albedo (SSA) for mineral dust. The data are stratified with the solar-spectrum surface albedo, with blue, green, and red denoting the surface albedo α of <0.1, ~0.2, and 0.3~0.35, respectively.

and surface radiative effects for high reflective surfaces (i.e., with the albedo of 0.3 to 0.35), about 38% and 60% respectively of that over ocean (i.e., albedo of less than 0.1), are mainly determined by the differences in surface albedo. This conclusion is further corroborated by the fact that the change of TOA to surface NADRE ratio with single-scattering albedo is well separated by the surface albedo, as shown in Figure 2.19. The ratio of TOA to surface NADRE decreases with the decreasing single-scattering albedo more rapidly over a high surface albedo than over a low surface albedo.

2.3.2.3 Pollution Aerosols

In North America, Europe, and East Asia, urban-industrial pollution perturbs the solar radiation appreciably, as shown in Figure 2.14. The aerosol climatology and radiative effect at the GSFC, representative of a pollution site in North America, is shown in Figure 2.20. The Angstrom exponent is over 1.7 and optical depth is highest during summer due to higher atmospheric relative humidity, consistent with other urban aerosols. In summer, aerosols impose the TOA ADRE of ~ 10 Wm^{-2} and surface ADRE exceeds 20 Wm^{-2}. The aerosol absorption in North America is close to that in East Asia, but smaller than Europe shown in Figure 2.4. The NADRE by industrial aerosol in Europe demonstrates a wider range and larger variation with larger standard deviation than that in North America and East Asia. On average, the TOA and surface NADRE is relatively large in North America.

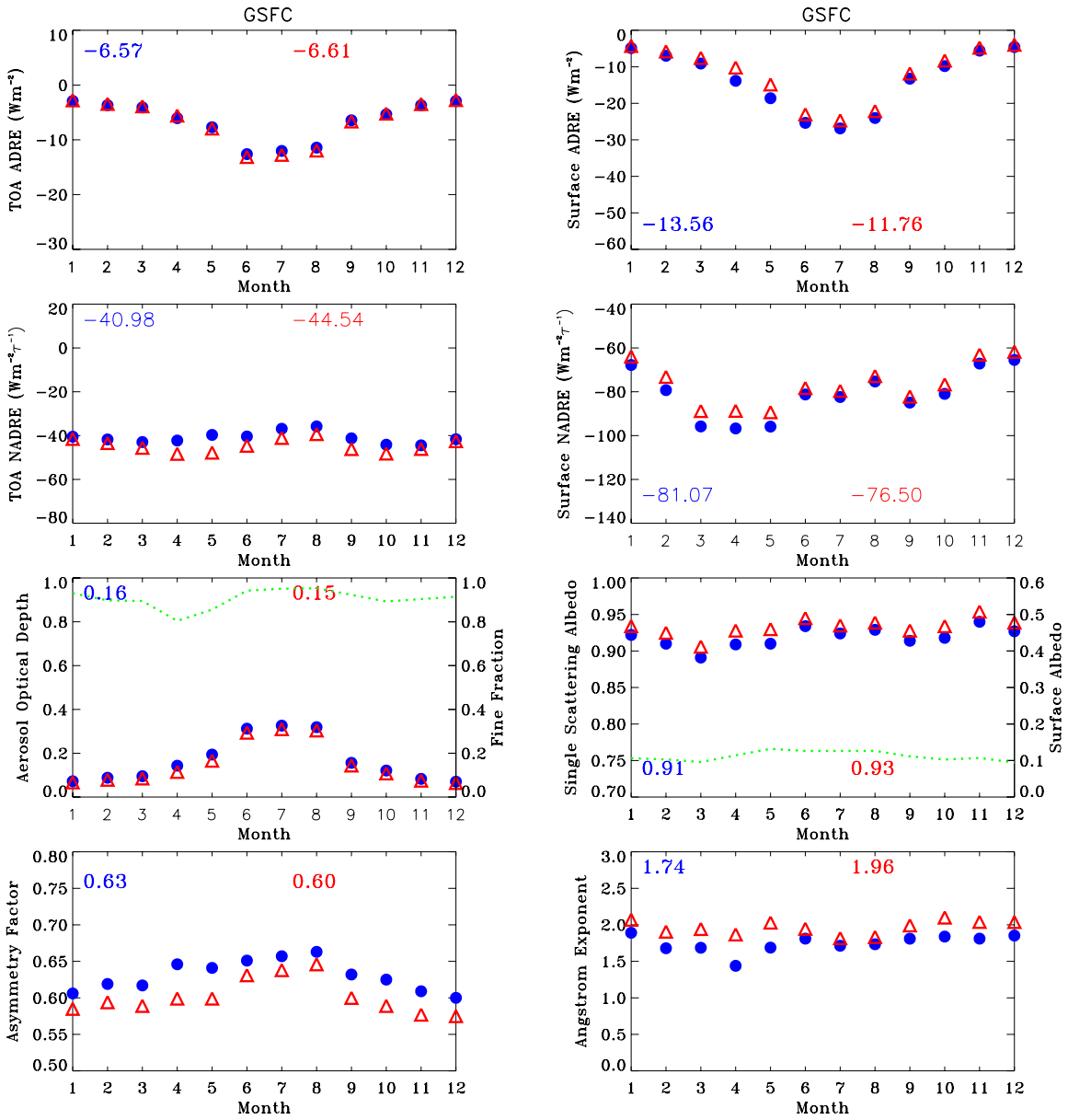

Figure 2.20 Pollution aerosol climatology at 550nm, aerosol direct radiative effect (ADRE) and its normalized form (NADRE) for all-mode (blue) and fine-mode (red) at site GSFC in North America. Numbers in each panel are mean values. Green lines refer to right axis for fine-mode fraction and surface albedo.

2.3.3 Cloud-free NADRE by Fine-mode Aerosol

In comparison to coarse-mode and all-mode aerosol, the fine-mode aerosol has a larger surface per unit volume and is closer in size to the wavelength of maximum solar energy. Thus, it should have a smaller absorption (i.e., larger single-scattering albedo) and a smaller forward-scattered fraction (i.e., smaller asymmetry factor) for the same chemical composition. The fine-mode aerosol also has a larger wavelength dependence (i.e., larger Angstrom exponent) than the all-mode aerosol does. Our calculations show that the Angstrom exponent has a relatively small effect (e.g., within 7%) on the aerosol direct effect, due to compensating effects at shorter and longer solar wavelength. As such, differences between fine-mode and all-mode NADRE are largely determined by differences in the single-scattering albedo and asymmetry factor as shown in Figure 2.4. The smaller absorption of the fine-mode aerosols increases the NADRE at the TOA but decreases it at the surface; the larger portion of backscattering or the smaller asymmetry factor increases the NADRE at both the TOA and surface. As such, distinctions between the fine-mode and all-mode aerosol NADRE should vary at the TOA and at the surface and should depend on aerosol types, as shown in Figure 2.21. The average values are shown in Figure 2.14.

Figure 2.21a shows that the biomass burning NADRE at the TOA for fine-mode aerosols is larger than that by all-mode aerosols, but they both are similar at the surface because more upscattering and less absorbing by fine particles are added at the TOA but offset at the surface. The ratio of average NADRE of fine-mode to all-mode aerosol is 1.20/1.36 at the TOA and 0.97/0.93 at the surface for South America/South Africa

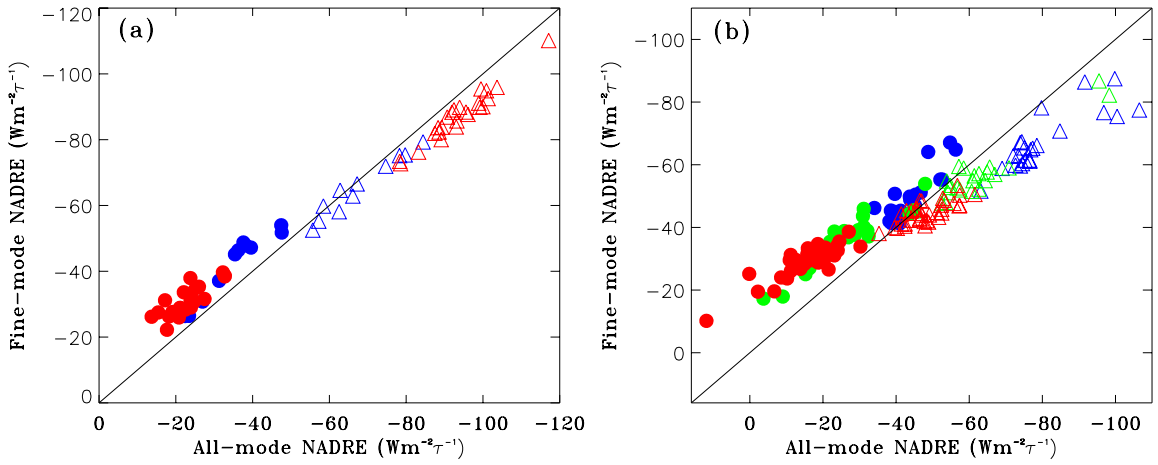

Figure 2.21 Comparisons of fine-mode and all-mode aerosol NADRE (unit**:** $Wm^{-2}\tau^{-1}$) at the TOA (dots) and surface (triangles) for (a) biomass burning aerosol, with blue and red representing South America and South Africa respectively; and (b) mineral dust, with blue, green and red representing the surface albedo α <0.1, ~0.2, ~0.3-0.35 respectively.

aerosols. The difference in asymmetry factor between fine-mode and all-mode aerosols is larger for mineral dusts than for biomass burning and industrial aerosols. The fine-mode dust NADRE is larger at the TOA and smaller at the surface (Figure 2.21b). According to Figure 2.4, the ratio of fine-mode to all-mode aerosol average NADRE increases at the TOA (1.2, 1.4, 1.8) and at the surface (0.83, 0.91, 0.93) as surface albedo increases (0.1, 0.2, 0.3-0.35) due to the radiative interactions of surface reflection with aerosols. Similar to biomass burning aerosol and mineral dust, the fine-mode NADRE for pollution aerosol is also larger at the TOA but smaller at the surface than the values for the all-mode NADRE. The NADRE difference between fine-mode and all-mode aerosol is relatively small, partially because of the high fine-mode fraction in industrial region.

Anthropogenic aerosols are generally fine particles and it has been proposed to use the fine-mode fraction derived from satellite observations and ground-based measurements to estimate the anthropogenic aerosol radiative forcing [Kaufman et al., 2002]. As discussed earlier, the NADRE differs substantially between fine-mode and all-mode aerosols. Note also that AERONET retrieval assumes one complex refractive index for particles of all sizes. If fine mode is dominating, then the retrieved refractive index is close to that of fine mode; if coarse mode is dominating then the retrieved refractive index is close to that of coarse mode. Sensitivity tests show measurements can be well reproduced with such an assumption [Dubovik et al, 2000b]. With the same refractive index, the retrieved single-scattering albedo will only reflect the wavelength dependence (related to particle size). As such, a fine-mode aerosol is less absorbing than an all-mode aerosol from AERONET retrievals and may not well represent the effects of

anthropogenic aerosols. Thus additional information besides the fine-mode fraction is needed to derive anthropogenic aerosol forcing [Anderson et al., 2005].

2.3.4 Cloudy-sky and All-sky NADRE by All-mode Aerosol

Clouds can modify the aerosol direct radiative effect, depending on cloud optical properties such as cloud fraction, cloud optical depth and the relative position of the cloud layer with aerosols. For each category in Table 2, Figure 2.22 shows the ratios of average cloudy-sky to clear-sky NADRE for below-cloud and within-cloud cases with the average total cloud optical depth (TCOD) and water cloud optical depth (WCOD). In the below-cloud case, the cloudy-sky NADRE is smaller than the corresponding value for clear-sky, depending mainly on the total optical depth of cloud. With an increase of cloud optical depth, the amount of solar flux transmitted through the aerosol layer decreases and so does its radiative effect. In the industrial regions examined in this study, the cloud optical depth is largest and values of cloudy-sky NADRE account for about 10% and 25% of clear-sky values at the TOA and surface respectively. Over the desert regions, the cloud is thinnest and the ratio of cloudy-sky to clear-sky NADRE is about 0.4 at the TOA and more than 0.5 at the surface. The overlying cloud layer reduces the TOA cooling by a larger percentage than the surface cooling, because the overlying cloud layer can efficiently reflect back the aerosol-upscattered solar radiation and hence increase the solar absorption in the atmosphere.

Because the aerosol optical depth is much smaller than the cloud optical depth, the surface NADRE under a cloudy sky is not sensitive to the position of the cloud layer. On the other hand, the TOA NADRE for a cloudy sky is quite different for the within-cloud versus the below-cloud cases, depending highly on the aerosol single-scatterig

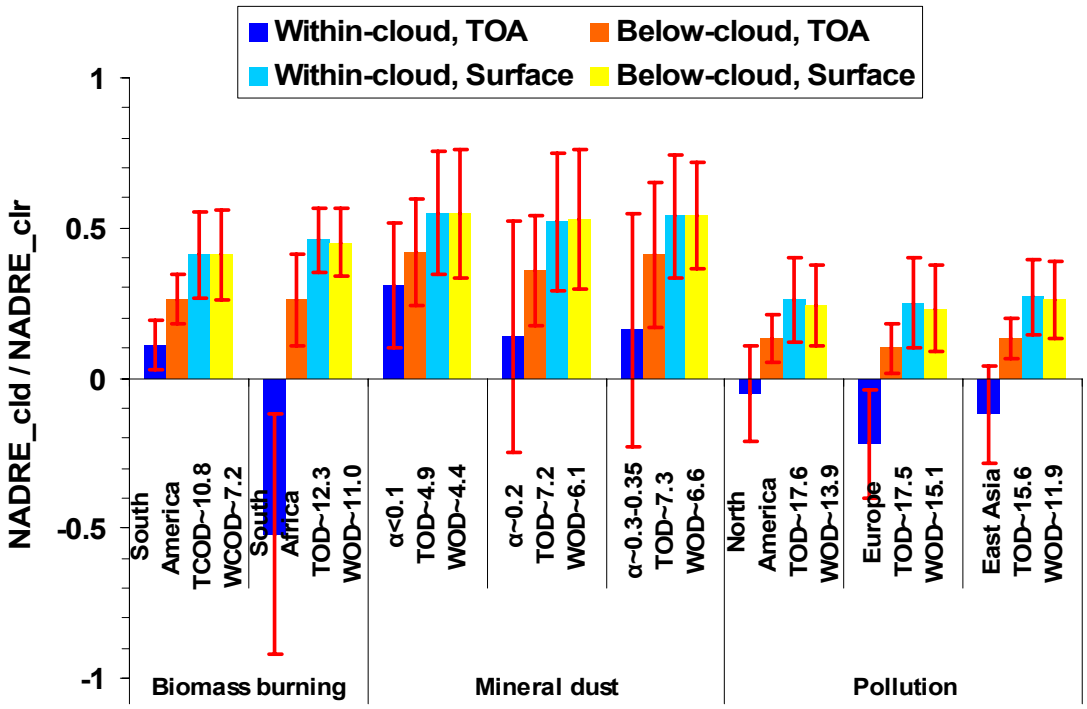

Figure 2.22 Ratio of average cloudy-sky NADRE (NADRE_cld) to clear-sky NADRE (NADRE_clr) at the TOA and surface for typical aerosol types and over different geographical regions, where α is surface albedo. TOD and WOD denote respectively the average total and water cloud optical depth from MODIS/Terra observations.

albedo. The stronger the aerosol absorption, the more efficient the aerosol layer absorbs the reflection from the underlying highly reflective cloud layer. Such absorption can be enhanced by multiple scattering between the cloud and aerosol layer [*Liao and Seinfeld*, 1998]. In comparison to the below-cloud case, this results in a much reduced negative TOA NADRE for weak absorbing aerosols such as dusts and South America biomass burning, and even reverses its sign to a positive TOA NADRE for stronger absorbing aerosols such as South Africa biomass burning aerosols and pollutions. In particular, for the assumed smoke-cloud profile in the within-cloud case, the South Africa biomass burning can cause a TOA heating for cloudy-sky, which is over 50% of the clear-sky TOA cooling. Such a strong TOA warming is consistent with a case study of South African biomass burning aerosol based on airborne aerosol and cloud measurements [Keil and Haywood, 2003].

Simple box models of global aerosol radiative forcing have assumed that [Charlson et al., 1992; Haywood and Shine, 1995] the aerosol direct forcing is negligible in a cloudy region and hence the ratio of all-sky to clear-sky NADRE is equal to clear-sky fraction. According to Equation (2.1b), if either the ratio of cloudy-sky to clear-sky NADRE or f_{cld} is close to 0, neglect of the cloudy sky cannot lead to serious error. However, as discussed above, the ratio of cloudy-sky to clear-sky NADRE cannot be neglected in the regions considered in this study and it increases with decreasing cloud optical depth. That is, the largest bias will occur for thinner cloud and larger cloud fraction. Any estimate of all-sky aerosol radiative effect is more complicated than that of clear-sky because of its dependence on cloud optical depth, cloud fraction, the relative position of cloud and aerosol layer, and aerosol optical properties. As shown in Figure

2.23 for all AERONET sites, for below-cloud cases, the all-sky to clear-sky NADRE ratio is generally larger than clear-sky fraction, and therefore the bias by zero-order assumption in simple box models is negative and it increases with decreasing cloud optical depth and clear-sky fraction at the TOA and surface. The ratio of cloudy-sky to clear-sky NADRE at the TOA follows the same pattern as that at the surface, but occasionally the ratio could be somewhat smaller than the clear-sky fraction ($1-f_{cld}$) because of a positive clear sky NADRE associated with large aerosol absorption and high surface albedo over land. For the within-cloud case, however, the cloudy-sky to clear-sky NADRE ratio at the TOA is more scattered with a number of cases smaller than ($1-f_{cld}$) due to the positive cloudy-sky ADRE, resulting from the strong absorbing aerosols when positioned above the cloud layer, and the positive bias increases with increasing cloud optical depth and aerosol absorption.

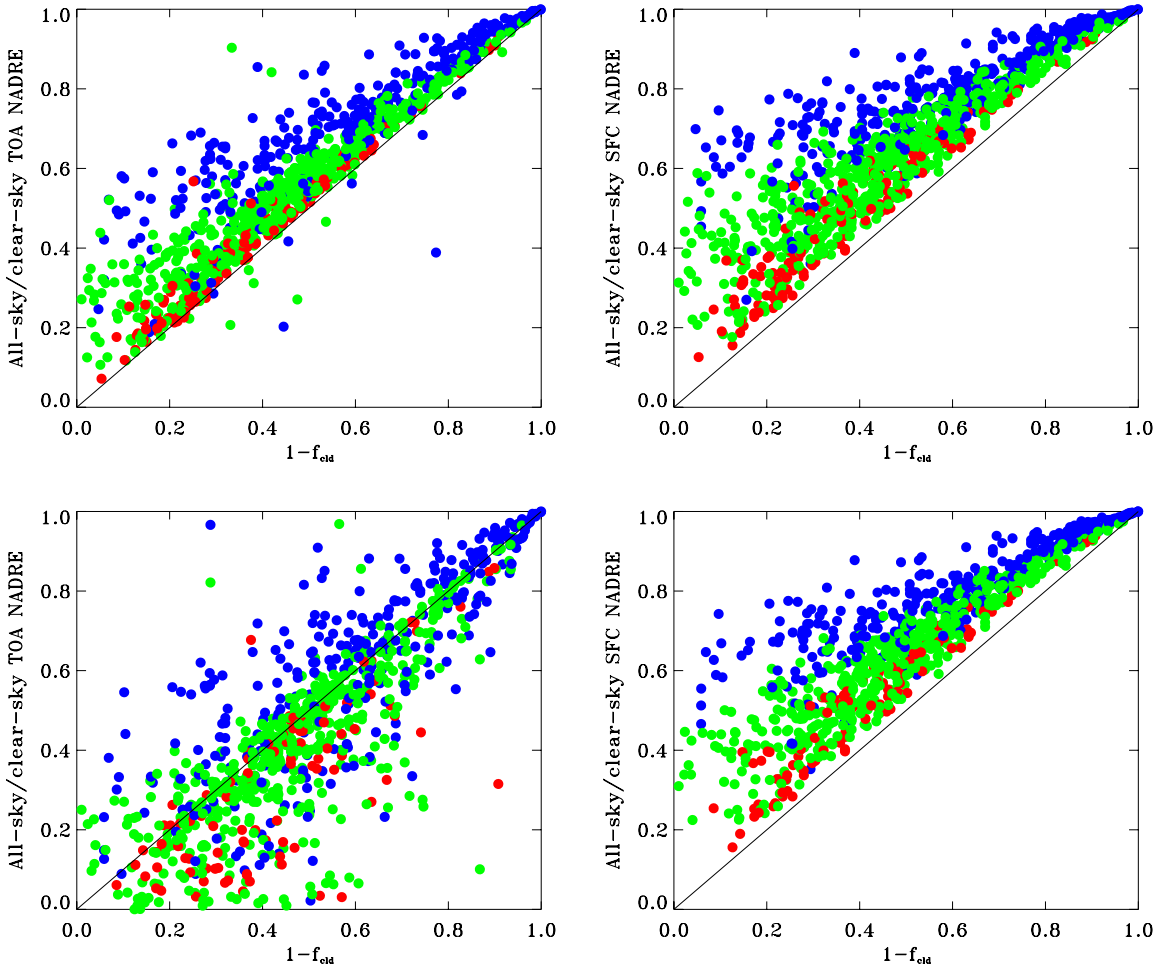

Figure 2.23 Correlation between the ratio of all-sky to clear-sky forcing efficiency and clear-sky fraction for all AERONET sites, for below-cloud (upper panel) and within-cloud (lower panel) cases. The data are stratified by cloud optical depth (COD), with blue, green, and red representing COD <10; COD ~ 10-20; and COD > 20, respectively.

2.3.5 Conclusion and Discussion for NADRE

The climatology of monthly aerosol direct radiative effect at both the TOA and the surface has been developed using the AERONET aerosol climatology covering a variety of aerosol regimes, in conjunction with MODIS retrievals of land surface albedo and clouds. The normalized ADRE with respect to optical depth removes much of the dependence of aerosol loading on the aerosol radiative effect; therefore it can flexibly serve as a baseline to evaluate estimates of aerosol direct radiative forcing using satellite observations, model simulations, and their combinations. The data can be provided at request. Yu et al. [2006] used such data to assess the regional aerosol direct radiative effect over land from five model simulations and four model-satellite integrations by compiling the AERONET site into different geographical zones (shown in Table 3). They found a modest correlation for weak cooling regimes (ADRE >-8 at the TOA or >-23 Wm^{-2} at the surface) and a very weak and even negative correlation in strong cooling regimes (ADRE <-8 at the TOA or <-23 Wm^{-2} at the surface) including South Africa and South America during the austral spring and winter, North Africa and mid-East year around, East Asia during non-summer season and Europe in winter. The possible reason for such discrepancies in strong cooling regimes include the uncertainties of model simulation and satellite retrievals, the inadequate regional representativeness of AERONET stations due to the limited number of sites, and the inconsistency of site-to-grid comparison.

Table 2.3 AERONET aerosol and ADRE climatology. Top panel: seasonal and zone averages of AOD (upper lines) and SSA (lower lines) at 550nm; Middle panel: seasonal and zone averages of clear-sky aerosol direct radiative effect (ADRE, Wm^{-2} at the TOA (upper lines) and the surface (lower lines). Bottom panel: blue dots indicate AEROENT stations. Light blue shadows the continents (Yu et al., 2006).

AOT (upper) and SSA (lower)

DJF/ MAM/ JJA/ SON	DJF/ MAM/ JJA/ SON	DJF/ MAM/ JJA/ SON	DJF/ MAM/ JJA/ SON
0.05/0.11/0.15/0.08 0.92/0.92/0.90/0.89	0.09/0.14/0.31/0.12 0.93/0.92/0.93/0.89	0.15/0.22/0.22/0.21 0.94/0.92/0.90/0.90	0.20/0.36/0.34/0.20 0.93/0.92/0.90/0.88
	0.26/0.34/0.33/0.28 0.96/0.96/0.94/0.94	0.39/0.38/0.38/0.32 0.92/0.94/0.93/0.93	
	0.14/0.11/0.32/0.47 0.91/0.90/0.89/0.92	0.11/0.10/0.27/0.43 0.89/0.88/0.85/0.88	

DRE (Wm^{-2}) at the TOA (upper) and surface (lower)

DJF/ MAM/ JJA/ SON	DJF/ MAM/ JJA/ SON	DJF/ MAM/ JJA/ SON	DJF/ MAM/ JJA/ SON
−1.9/−4.4/−5.2/−2.7 −3.6/−10.1/−14.4/−6.7	−2.8/−6.0/−11.1/−4.5 −5.2/−12.8/−23.9/−10.8	−5.0/−7.0/−6.1/−5.8 −8.4/−17.6/−21.0/−14.9	−6.4/−10.7/−8.1/−5.3 −11.9/−28.2/−30.4/−15.7
	−8.4/−10.7/−10.4/−9.2 −14.5/−20.0/−23.2/−18.1	−9.1/−9.8/−9.0/−8.1 −23.8/−23.8/−24.3/−20.1	
	−3.9/−3.4/−7.2/−11.2 −11.4/−9.4/−23.3/−30.9	−2.7/−3.0/−6.4/−9.8 −10.6/−9.0/−23.5/−33.9	

AERONET Sites

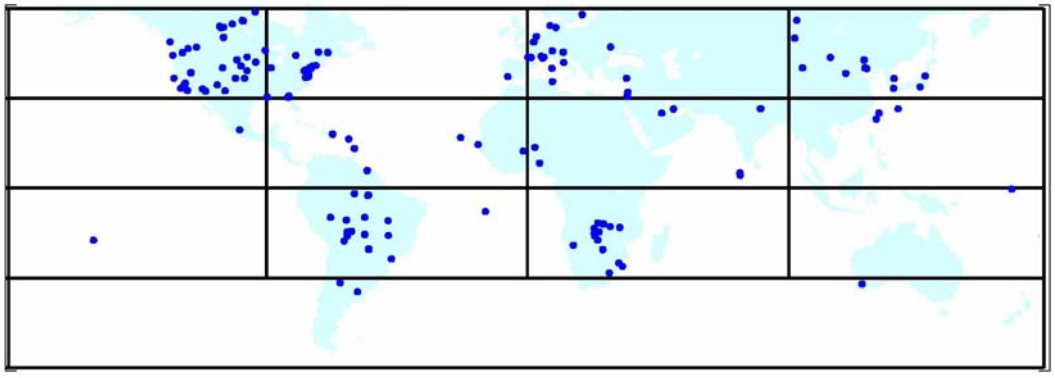

The variability of both aerosol types and surface albedos lead to a large range of clear-sky NADRE, varying from about -45 to -15 $Wm^{-2}\tau^{-1}$ at the TOA and from -90 to -50 $Wm^{-2}\tau^{-1}$ at the surface. Because of its much stronger absorption than that of Amazon smoke, South African smoke on average has a NADRE that is smaller in magnitude by ~35% at the TOA but larger in magnitude by ~38% at the surface. Dust storms in North Africa and Arabian Peninsula influence wide areas where surface albedos range from 0.1 or less to more than 0.3. Such large variations of surface albedo cause large differences in the dust NADRE. The NADRE is -44 and -80 $Wm^{-2}\tau^{-1}$ at TOA and surface over oceans, but it decreases respectively to -17 and -48 $Wm^{-2}\tau^{-1}$ over highly reflective deserts. The AERONET derived fine-mode aerosols have larger values of single-scattering albedo and smaller values of asymmetry factor than have the all-mode aerosols, resulting in a greater (more negative) effect at the TOA but smaller (less negative) effect at the surface. These AERONET derived fine-mode aerosol properties (e.g., absorption or single-scattering albedo) may be different from those of anthropogenic aerosol properties. More efforts are necessary to explore how the fine-mode fraction obtained recently from ground-based and satellite measurements could be used to optimally estimate the anthropogenic aerosol forcing.

The effect of clouds on the ADRE is usually not negligible for the observed cloud optical thickness but is not easily quantified because of its dependence on vertical profiles of aerosol and cloud. The surface NADRE is found to be less sensitive to the position of the cloud layer than that at the TOA. When a portion of aerosol is above the cloud layer, the TOA cooling by weakly absorbing aerosols is much reduced and can even be a positive value (TOA heating) for strongly absorbing aerosols. In particular, if

half of the highly absorbing smoke over South Africa were elevated above warm clouds, the TOA would be a heating with a magnitude that was over 50% of the clear-sky TOA cooling.

It is challenging to validate our calculations because of a lack of independent ground-based measurements and inconsistency in spatial coverage. Satellite measurements of fluxes such as those from CERES currently don't derive aerosol radiative forcing over land because of difficulties in quantifying large and heterogeneous surface reflection. We compare AERONET NADRE with some measurement-based estimates of pollutions over East US, Europe and East Asia, and dust over tropical North Atlantic. AERONET shows good agreement with 5-15% differences in estimations over the Mediterranean Area [Markowicz et al., 2002], rural East China at the TOA [Xu et al., 2003] and west coast of North Africa at the surface [Li et al., 2004], but relatively large discrepancies of ~30-60% in the East US [Kinne and Pueschel, 2001], rural East China at the surface [Xu et al., 2003] and west coast of North Africa at the TOA [Li et al., 2004]. A more thorough comparison with model simulations, model-satellite integrations and intensive field measurements is addressed in the review paper by Yu et al. [2006].

2.4 Application of High-resolution MODIS Land Albedo to Estimate Aerosol Direct Radiative Effect over North Africa and the Arabian Peninsula

2.4.1 Introduction to the Spatial Variation of MODIS Land Albedo

Surface albedo, as one of the key factors in solar energy budget, is an important factor in determining how aerosol perturbs solar radiation [Coakley et al., 1983; Haywood and Shine, 1995, 1997]. Further, multiple reflections between surface and aerosols extend and complicate the influence of surface albedo on the aerosol radiative effect. TOA forcing is particularly sensitive to surface albedo change because 1) the relatively small absolute value of TOA forcing results from partial cancellation of the surface cooling and the atmosphere heating; 2) Aerosols absorb as well as scatter back the surface-reflected solar energy through multiple reflections between surface and aerosols. Both contribute to reduce the outgoing solar radiation and thus increase the net downward radiation flux at the TOA. However, not much attention had been paid in aerosol radiative calculations to treatments of realistic surface albedos and the associated uncertainties.

MODIS acquires a global data set in seven spectral bands from visible to middle near-infrared, providing the first available global land surface albedo products at 1-km resolution for direct and diffuse radiation and its multispectral ability improves the quality of the retrieved data [Schaaf et al., 2002]. Of particular value to us is that the high-resolution MODIS land albedo provides a unique opportunity to better quantify the the aerosol direct radiative effect. MODIS data demonstrate considerable spatial variability in surface albedo over the arid areas of Northern Africa and Arabian Peninsula [Tsvetsinskaya et al., 2002], which has been also observed by other space borne

spectroradiometers [Strugnell et al., 2001; Pinty et al., 2000]. However, few coupled land-atmosphere models capture this observed spatial variability. Compared with land albedo from MODIS, the Common Land Model (CLM) considerably underestimates the surface albedo for the semi-arid and arid regions, especially in the near-infrared band, with the largest low bias of about 0.1 in the Sahara [Zhou et al., 2003; Oleson et al., 2003].

Here, we take advantage of the spatial and spectral high-resolution MODIS land surface albedo to study the clear-sky aerosol direct radiative effect (ADRE) over Northern Africa and the Arabian Peninsula for the summer of 2001. The aerosol optical properties on a T42 grid (2.8˚ × 2.8˚), as discussed in Section 2.2.2, are used. Aerosol optical depth at 550nm is obtained from assimilating MODIS retrievals and GOCART model simulations; other spectral aerosol optical parameters of Angstrom exponent, single-scattering albedo and asymmetry factor are derived from GOCART simulation. The goal of this study is to characterize the influence of such high spatial resolution land albedo on the ADRE spatial variability and to discuss the dependence of regionally averaged ADREs on the spatial and spectral resolution of surface albedo. The difference of ADRE derived from that of MODIS and CLM land albedo is also addressed. Note that we specifically account for how aerosols interact with surface albedos to impact their direct radiative effects; therefore the aerosol effect on the thermal infrared radiation is not considered.

2.4.2 MODIS and CLM-CCM3 Land Surface Albedo

We use the version 4 MOD43C1 MODIS surface albedo data with 0.05˚ × 0.05˚ resolution for seven MODIS spectral bands and three broadbands (0.3-0.7, 0.7-4.0, and

0.3-4.0 μm) of every 16-day period [Schaaf et al., 2002] for year 2001. The surface albedo is represented by white-sky albedo in this study, thus it is independent of solar zenith angle. Over Northern Africa and the Arabian Peninsula for summer 2001, the surface albedos are obtained from the average values of MODIS periods starting on days of 161, 177, 193, 209, 225 (i.e. approximately period of June-August) for the region of 20˚W ~ 50˚E and 10˚N ~ 40˚N. 0.05˚ × 0.05˚ resolution is then subsequently aggregated to 0.2˚ × 0.2˚, 1˚ × 1˚, and 2.8˚ × 2.8˚ (T42 grid) resolutions. As the aerosol contamination is a major concern on MODIS retrieved surface albedo over this region, we examine the annual time series of several sites with relatively high or low surface reflectivity. Because soil surface albedo changes little with season [Zhou et al., 2003] but the aerosol loading can be largely enhanced when influenced by dust outbreaks starting from spring, the observed albedo of low reflective surface will fluctuate more strongly in time than that of high reflective surface when the observation of the surface albedo is considerably contaminated by aerosols. Thus, the stable temporal trends for all examined sites increase our confidence in MODIS albedo data. MODIS spectral band albedos are interpolated or extrapolated to spectrum bands of the radiative transfer model based on solar energy spectrum distribution.

For comparison, the compatible white-sky surface albedos for visible (0.3-0.7 μm) and near-infrared (0.7-4.0 μm) broadbands of summer 2001 are also obtained from coupling of CLM with NCAR Community Climate Model version 3 (CCM3) at T42 grid [Zhou et al., 2003]. Figure 2.24 shows the broadband (0.3-4.0μm) white-sky albedo at T42 grid for CLM-CCM3 and MODIS retrieval, respectively. Note that we only study the land area over this region; hence any T42 grids that include both land and ocean during

the aggregation are eliminated. CLM-CCM3 land albedo differs from MODIS land albedo not only in its spatial variablity but in magnitude. CLM-CCM3 has a relatively homogenous land albedo, missing much spatial variation. On a regional average, CLM-CCM3 underestimates the mean value of white-sky surface albedo by ~ 0.05 in the visible band (0.3-0.7μm) and ~ 0.09 in the near-infrared band (0.7-4.0μm) over our study region.

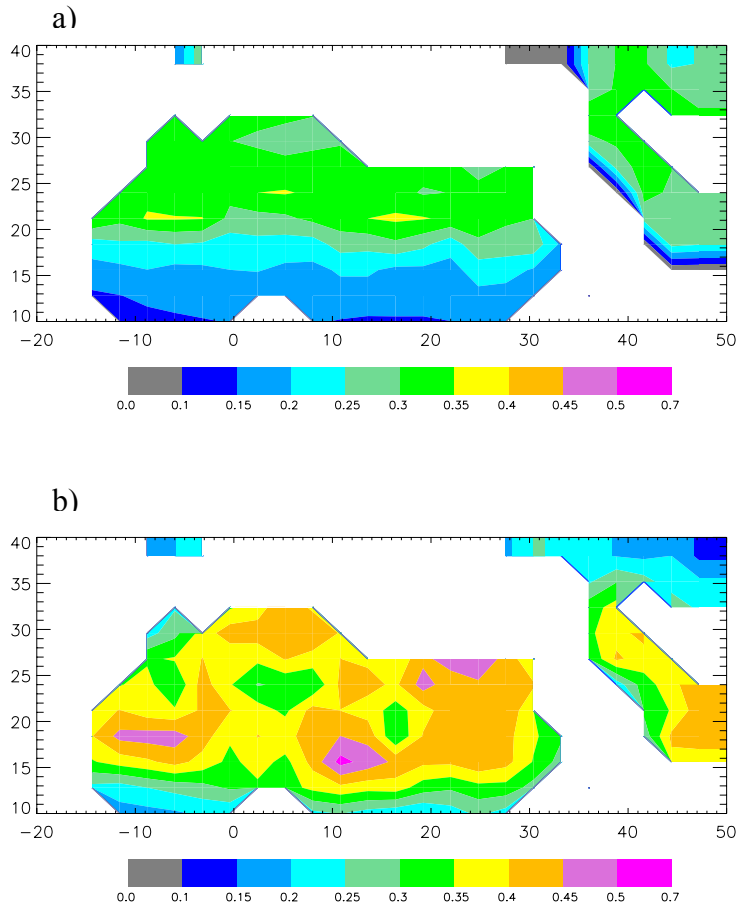

Figure 2.24 White-sky (0.3-4.0μm) land surface albedo at T42 grid over Northern Africa and the Arabian Peninsular (20˚W ~ 50˚E, 10˚N ~ 40˚N) in summer 2001 for a) CLM-CCM3 and b) MODIS retrieval (grids including both ocean and land are eliminated).

2.4.3 Results and Discussion

2.4.3.1 Spatial Variability of Aerosol Direct Radiative Effect

Comparisons of MODIS solar shortwave (0.3-4.0 μm broadband) white-sky albedos between 0.05˚ × 0.05˚ resolution and 0.2˚ × 0.2˚ resolution shows close spatial similarity, but some spatial variations are appreciably smoothed off at 1˚ × 1˚ resolution, suggesting that 0.2˚ × 0.2˚ resolution is sufficient for a study on spatial variation. MODIS land surface albedo and the integrated MODIS and GOCART aerosol optical properties discussed in Section 2.2.2 are used as inputs for the radiative transfer model to estimate the clear-sky aerosol direct radiative effect (ADRE) over the study region. We choose summer conditions to allow for high spatial variability of land surface albedo and heavy aerosol loading. Figure 2.25a shows the shortwave broadband white-sky albedo at 0.2˚ × 0.2˚ resolution with substantial spatial variability covering a range of 0.1 ~ 0.5. The geographical distribution of ADREs over Northern Africa and the Arabian Peninsula are shown in Figure 2.25b-d, based on seven spectral band and 0.2˚ × 0.2˚ spatial resolution MODIS albedo together with aerosol optical properties at a T42 grid resolution. The TOA ADRE shows high resolution spatial variability, following closely to that of surface albedo. Such high spatial variability of TOA ADRE can have important implication for the regional aerosol climatic effect. However, the spatial resolution of surface and atmosphere ADRE appears much coarser though that of surface albedo is high, indicating that they are more controlled by the resolution of aerosol optical properties.

Over most parts of the domain, the atmospheric absorption is more than the surface cooling, giving a positive TOA ADRE. There is always warming at TOA over the area when surface albedo above 0.3, while cooling over less reflective surfaces with albedo

below 0.25. Higher surface albedo mostly corresponds to larger TOA warming, which is partially contributed by the overall large aerosol loading. The largest TOA warming of ~ 20 Wm^{-2} results from a combination of high surface albedo (> 0.4) and heavy aerosol loading (i.e. large aerosol optical depth > 0.6) as the single-scattering albedo is relatively homogenous over this region (~ 0.9). However in Section 2.3.3.2, the dust ADRE at the TOA was found to be negative for surface albedo of 0.3 ~ 0.35 (shown in Figure 2.18), a result of differences in single-scattering albedo between GOCART simulations and AERONET measurements as discussed in Section 2.2.2. Notice that the two highest surface albedo (> 0.5) places are very close to the areas with largest aerosol optical depth over the Sahara, which may indicate that dust source is close to the most arid land surface. As expected, the heaviest aerosol loading with relatively small surface albedo cools the surface at most by -40 ~ -50 Wm^{-2} and with relatively high surface albedo heats the atmosphere at most over 50 Wm^{-2}.

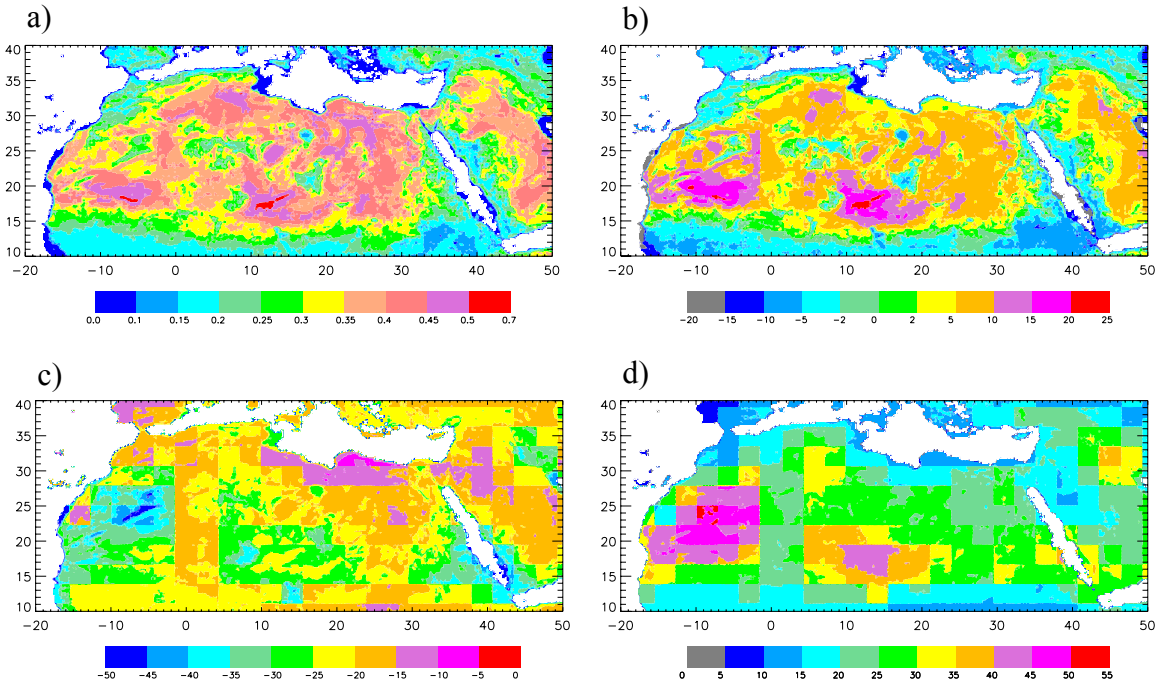

Figure 2.25 Aerosol direct radiative effect (ADRE, unit: Wm^{-2}) over Northern Africa and the Arabian Peninsula (20˚W ~ 50˚E, 10˚N ~ 40˚N) for summer 2001 using MODIS land surface albedo for seven spectral bands and on 0.2˚ × 0.2˚ resolution, and aerosol optical properties on T42 grid: a) 0.3-4.0μm broadband white-sky surface albedo; b) TOA ADRE c) surface ADRE; d) atmosphere ADRE.

2.4.3.2 Regional Mean Aerosol Direct Radiative Effect

In addition to the spatial variability, the mean values of ADRE are also significant for regional climate change of Northern Africa and the Arabian Peninsula. We present the regionally averaged ADREs derived from the MODIS land surface albedo for seven spectral bands at various spatial resolutions (Table 4). For seven-band and 0.2˚ × 0.2˚ MODIS albedo, the mean heating in the atmosphere (26.4 Wm^{-2}) is larger than surface cooling (22.3 Wm^{-2}), leading to 4.1Wm^{-2} warming at TOA. This can be explained by the overall effective 'albedo' of the aerosol layers being lower than that of the land surface below. Although the solar insolation at the TOA is only enhanced by about 1.3% by aerosols, this amount is comparable to greenhouse forcing of 2.4 Wm^{-2} since the anthropogenic portion is about 30~ 70% of total dust loading [Mahowald and Luo, 2003; Sokolik and Toon, 1996; Tegen and Fung, 1995]. The solar energy of the earth-atmosphere system is not only increased but also substantially redistributed from surface cooling to aerosol layer warming. The dominant effect is that the atmospheric solar heating is substantially increased by about 37.8% from what if would be without aerosols. At the same time, the surface solar radiation is decreased by about 8.9%. The significantly reduced surface-atmosphere solar flux gradient ~ 50W/m^2 by the absorbing haze has the potential to profoundly impact climate by stabilizing temperature profile, hence changing precipitation, atmospheric circulation and in turn dust loading. With the same spectral resolution, 2.8˚ × 2.8˚ spatial resolution differs from 0.2˚ × 0.2˚ resolution by 12.7%, 1.0% and 2.8% for ADREs at the TOA, surface and atmosphere, indicating TOA ADRE is the most sensitive but surface ADRE is the least sensitive to surface albedo resolution. The differences of aerosol forcing between 1˚ × 1˚ and 0.2˚ × 0.2˚ are

generally within 1%, suggesting 1˚ × 1˚ surface albedo resolution is adequate for studying regional mean aerosol direct effects in terms of the spatial variation of surface albedo. A Comparison of Table 4 with Table 5 shows that the ADRE changes little between that from seven spectral band and from two broadband (visible, near-infrared) MODIS albedos at 2.8˚ × 2.8˚ spatial resolution. This is likely a result from the spectral resolution limitation of the radiative transfer model used in present study.

As shown in Figure 2.24, it is difficult to compare the geographic pattern of MODIS surface albedos to that of CLM-CCM3 albedos. Therefore we address the difference between the mean ADRE derived from MODIS surface albedos and that from CLM-CCM3 surface albedos (Table 5). For comparison, we use MODIS albedos on the same T42 grid resolution as CLM-CCM3 albedos. Regionally, the lower CLM-CCM3 surface albedos increase the cooling at the surface by 17.5% and decrease the heating within the atmosphere by 5.6%, resulting in a sign change of aerosol forcing at TOA to negative ~ -2.0 Wm^{-2} from positive ~ 3.3 Wm^{-2} based on MODIS surface albedos. How the observed surface albedos compare with modeled is beyond the scope of this study.

Table 2.4 Regional mean aerosol direct radiative effect (ADRE) derived from MODIS land surface albedo for seven spectral bands and at various spatial resolutions

Spatial resolution	0.2˚× 0.2˚	1˚× 1˚	2.8˚× 2.8˚
TOA ADRE (Wm^{-2})	4.06	4.10	3.54
TOA ADRE difference (%)	Base	0.99%	12.73%
Surface ADRE (Wm^{-2})	-22.35	-22.36	-22.13
Surface ADRE difference (%)	Base	0.04%	0.98%
Atmosphere ADRE (Wm^{-2})	26.41	26.46	25.68
Atmosphere ADRE difference (%)	Base	0.18%	2.79%

Table 2.5 Regional mean aerosol direct radiative effect (ADRE) derived from MODIS and CLM-CCM3 surface albedos for two broadband (visible, near-infrared) at a T42 grid resolution

2.8˚× 2.8˚ broadband surface albedo	MODIS	CLM-CCM3
TOA ADRE (Wm^{-2})	3.32	-2.02
TOA ADRE difference (%)	base	**Sign change**
Surface ADRE (Wm^{-2})	-22.33	-26.24
Surface ADRE difference (%)	base	-17.50%
Atmosphere ADRE (Wm^{-2})	25.65	24.22
Atmosphere ADRE difference (%)	base	5.57%

2.4.4 Conclusion

Surface albedo, as one of the key components controlling solar energy budget in the earth-atmosphere system, is an important factor for determining direct radiative effects by aerosols. The multiple reflections between surface and aerosol layers further extend and complicate the influence of surface albedo. The TOA forcing is particularly sensitive to a change in surface albedo. For a high surface albedo, aerosol can enhance the atmosphere warming and reduce surface and TOA cooling, even change the sign of TOA forcing. Thus, an inadequate specification of heterogeneous surface albedos adds uncertainty to the characterization of aerosol direct radaitive effect. MODIS acquires high spatial resolution land surface albedos for seven spectral bands and for direct and diffuse radiation, providing an opportunity to improve quantification of aerosol direct radiative effect.

White-sky albedos are used in the present study to represent surface albedos of Northern Africa and the Arabian Peninsula. Over this region, the black-sky albedo at local solar noon is essentially identical to the white-sky albedo in term of spatial pattern and the difference between the black-sky and white-sky albedo is uniformly under 5% [Tsvetsinkaya et al., 2002]. The solar zenith angle dependence of black-sky albedos over bare soils or sparse vegetation is relatively small [Yu et al., 2004]. Consequently, incorporating of black-sky albedos would not introduce any considerable modification to our results. Further work can incorporate formulas for the dependence of desert albedo on solar zenith angle [Wang et al., 2005] to evaluate its influence.

MODIS-derived spatial and spectral high-resolution land surface albedos are used to present the clear-sky aerosol direct radiative effect over North Africa and the Arabian

Peninsula during the summer of 2001, where surface is high reflective with considerable spatial variability but is poorly described by modeling. Aerosol optical properties are obtained from integrated MODIS retrieval and GOCART model simulation. Based on MODIS surface albedos at 0.2˚ × 0.2˚ resolution together with aerosol optical properties on T42 grid resolution (2.8˚ × 2.8˚), the spatial pattern of the TOA ADRE shows high spatial variability with close similarity to that of surface albedo; however, the coarser spatial resolution of surface and atmosphere ADREs are more controlled by that of aerosol optical properties. In terms of surface albedo, a 0.2˚ × 0.2˚ resolution is sufficient to capture the spatial variability and 1˚ × 1˚ resolution is adequate for the regional mean aerosol direct radiative forcing. Regionally, vertical solar energy redistribution by the absorbing haze from the surface to the atmosphere significantly enhances atmospheric heating by ~ 38% due to the large surface albedos, and leads to net warming at TOA ~ 4 Wm^{-2}. CLM-CCM3 albedo changes positive TOA forcing (3 ~ 4 Wm^{-2}) based on MODIS albedo to negative (~ -2 Wm^{-2}), resulting from both contributions of larger surface cooling (~ 4 Wm^{-2}) and less atmospheric heating (~ 1.5 Wm^{-2}). Such differences are essential for aerosol climatic effect over the study region and emphasize the importance of a realistic specification of heterogeneous surface albedos in characterization of aerosol direct radiative effect.

The overall warming effect at the TOA over North Africa and the Arabian Peninsula is a result of both a relatively large surface albedo and a small single-scattering albedo (i.e. strong aerosol absorption). Dust from modeling studies (e.g. GOCART) has a significantly stronger absorption than shown by in situ measurements (e.g. AERONET) probably because of a lack of consideration of the mixing mechanism of hematite in dust

absorption simulation [Dubovik et al., 2002]. This explains the discrepancy in average TOA ADRE of positive (i.e. warming) in this section but of negative (i.e. cooling) in Section 2.3.2.2 for dust over regions of high surface albedo. Therefore, in addition to a more accurate characterization of surface albedo, also needed is a better characterization of the dust absorption and hence its influence on the aerosol direct radiative effect over North Africa and the Arabian Peninsula.

Aerosol increases solar absorption in the atmosphere (~ $25Wm^{-2}$) and decreases solar radiation at the surface (~ $-22Wm^{-2}$), hence significantly reducing the surface-atmosphere solar flux gradient. As suggested by some studies [e.g., Ramanathan et al., 2001; Hansen et al., 1997; Ackerman et al., 2000; Yu et al., 2002], such a change can increase atmospheric stability, suppress convection development, and hence impact the atmospheric circulation, hydrological cycles, and regional and global climate. The next chapter will contribute to an effort to improve our understanding of this issue by developing an explicit climatological convective boundary layer model.

CHAPTER 3

A CONCEPTUAL MODEL OF A DRY CLIMATOLOGICAL CONVECTIVE BOUNDARY LAYER

3.1 Introduction

As the lowest part of the atmosphere, the atmospheric boundary layer is directly influenced by the effects of surface (friction, heating and cooling) [e.g., Garratt, 1992]. Of particular importance is its interaction with the large scale atmosphere through transports of mass, momentum, heat and/or moisture and hence its influence on large-scale dynamics. Convection is a system with positive and/or negative buoyancy, which makes the lighter air move upward through surrounding air as forced by a pressure gradient force against gravity. A convective boundary layer (CBL) commonly develops during daytime under fair weather conditions over land, where the buoyant energy comes from the surface heating. Because of the small thermal capacity of the land surface, the diurnal cycle of the planetary boundary layer (PBL) over land is driven by the diurnal cycle of solar forcing at the land surface. In the morning, surface heat flux, driven by the solar radiation, warms up the shallow nocturnal stable layer. It then rapidly mixes with the above residual layer, which remains from the extend of the daytime boundary layer for the previous day and is maintained close to adiabatic. The growing buoyant thermals are suppressed by a capping inversion between the boundary layer and the above free atmosphere and reach a quasi-stationary CBL in the late morning or in the afternoon. In the late afternoon when the surface heating decreases, a CBL cannot be maintained

against viscous dissipation and so decays. At night, a surface inversion is developed due to surface cooling and a shallow nocturnal stable layer forms.

Convective boundary layers consist of an unstable surface layer, a nearly mixed middle layer and an overlying entrainment zone, sometimes approximated as an interface. Eddy mixing and buoyant plumes are commonly used concepts in climate models. A non-local term is added in eddy diffusivity to capture the counter-gradient term in the CBL. This term is made to depend on surface fluxes and appears to capture only the impacts of the buoyant plumes from below. Simple versions of the concept of a buoyant plume have been used in some boundary layer parameterizations, in particular that of Blackador [1979], and Zhang and Anthes [1982]. Lappen and Randall [2001] have shown that use of a mass-flux description of plumes could lead to improvement in the modeling of the CBL. Mass-flux alone is simply a statement of mass conservation that must be supplemented by a determination of the ratio of updraft to downdraft areas and a determination of lateral entrainment and detrainment mass flux. Their analysis relates mass flux to second and third moments of vertical velocity and uses higher order turbulence equations to infer these moments. Cheinet [2003] has developed a model where the initial statistics of buoyant plumes are prescribed as a probability distribution function and the convective boundary layer structure is recovered. All the existing turbulence and plume treatments suffer from their vagueness as to how air is heated at the surface. That is, they are driven by average heat fluxes as diagnosed by surface similarity. They do not reference the coherent structures that are known to move most of the heat from the surface and that may be the key to describe how the land surface impacts the convective boundary layer.

The maintenance of a nearly adiabatic "residual" layer at night over the depth to which the previous daytime convective boundary layer extended provides a climatological basis for convection over land and it happens over much of world. Convection can hence be described as an average condition of the atmosphere given the average surface conditions. The diurnal evolution of the CBL has been extensively investigated using large-eddy simulations (LES) with much less attention given to how the equilibrium climate near the land surface (on timescales longer than the diurnal) develops. Nevertheless, it is important to clarify the climate equilibrium over land surface in order to assess the feedbacks associated with climate changes [Betts, 2000]. Current climate models generally treat convection as a 1-D transient response to surface heating and this treatment may not be adequately realistic for examining various climate feedbacks, for instance how convection can be modified by the influence of aerosol radiative forcing. This thesis contributes to an effort to study the climatological role of convection as a component of the climate system as distinct from smaller scale transient turbulence.

A convective boundary layer exhibits a coherent structure of convective circulation composed of upward and downward draughts. Such could be more realistically described by using objects that have horizontal as well as vertical velocities, in which the mass intake would be viewed from the horizontal structure, not from turbulent lateral entrainment and detrainment. Our approach is to simulate climatological convection as two-dimensional (2-D) vortices in the framework of fluid dynamics and thermodynamics. Such 2-D vortices are much more attractive constructs from an

efficiency viewpoint. They provide the coherent object basis function that might be used to construct computational effective approaches for convection.

Recently, 2-D numerical modeling of 3-D atmospheric convection has become of interest because the 1-D convection parameterizations in climate models are believed to be at a "deadlock" [Randall et al., 2003] and 3-D LES are too computationally expensive to use for a relatively long timescale simulation. In an LES model, the governing equations are spatially filtered to derive the resolved-scale (or large-eddy) and subgrid-scale motions. There is no theoretical basis to rigorously derive the governing equations for 2-D LES; all y derivatives are assumed as zero for a 2-D description using the same governing equations as 3-D models [Moeng et al., 2004]. Thus, in their 2-D model, the velocity field still has three components: u, v, w for coordinates x, y, and z. We propose here a conceptual 2-D model without the y dimension.

In sum, our objective is to develop a simple 2-D description of convective cells that allows their superposition in a convective boundary layer so as to explicitly provide its transport properties with fewer degrees of freedom than the full system, while the smaller scale turbulence effects are parameterized. The first step of this effort is to develop a numerical solution for these elemental eddies. We start with dry convection and it can be extended to the moist convection of cumulus clouds. The totality of diabatic and adiabatic atmospheric processes are forced by surface heating. The atmosphere responds through various dynamic, radiative and latent heat releasing processes, to maintain a climatological boundary layer structure. By separating the balances between these terms into small scale turbulence, dry convection, and everything else, we seek to better clarify the distinct climatological role of dry convection within the boundary layer.

Given the nonlinear dynamical system, we are trying to simplify to get a dissipative forced system with stable attractors. We hope we can make this correspond to the coherent objects or strange attractor structures that are found in purely numerical models of large boundary layer eddies.

3.2 Conceptual Formulation

The purpose here is to develop the climatological basis for understanding convective boundary layers over a region (e.g. assumed to be a homogeneous surface with spatial scale of tens to hundreds km). For simplicity, the boundary layer is assumed to be dry, that is explicit moist processes are neglected, so it is most directly appropriate for a semi-arid land surface. Conservation of energy within a layer of atmosphere over some surface region is

$$C_p \rho \frac{\partial T}{\partial t} = Q, \tag{3.1}$$

where Q is formally the sum of all the diabatic and adiabatic heating terms averaged horizontally over the region and so depending only on z and all the other model parameters entering in to determine the average. Similarly, T is the spatially averaged potential temperature depending only on z. One component of Q is heating at the bottom of the atmosphere by energy transfer from the surface of energy absorbed there by radiative processes. Standard terms conventionally included in Q to address the response to such heating are the vertical advection of temperature $w\frac{\partial T}{\partial z}$ and cooling by adiabatic expansion $w\frac{g}{C_P}$ in the 1-D description. The simplest resulting description is that of "dry

adiabatic adjustment" with $T(z) = T(0) - (g / C_P)z$. This result is achieved by assuming that for lapse rates greater than g / C_P, convective turbulence will result and bring back the temperature profile to an adiabatic one.

The above description suffices for many purposes. However, it becomes insufficient in several contexts. The implied overturning will only occur if the lapse rate is to some degree unstable. The degree of instability will be determined by the most efficient mechanism for carrying heat vertically which involves the largest scale eddies that can exist within the unstable region. These necessarily have a distinct structure in both the vertical and horizontal. An average over a large number of such structures may give an average 1-D picture of convective boundary layers. This has commonly been done by simple similarity theories [e.g., Sorbjan, 1989; Garratt, 1992] or large eddy resolving numerical models [e.g., Holtslag and Moeng, 1991; Schumann and Moeng, 1991]. Our purpose is to develop an intermediate approach in which the convective eddies are treated as distinct 2-D simple quasi-stable entities separate from the smaller scale turbulence. A description of such eddies may be needed to best quantify the vertical transport of other quantities and is especially important for the description of the occurrence of convective clouds and their dependences on aerosols (e.g., in transport modeling for aerosols producing cloud, atmospheric chemistry and air pollution applications). Such has been done up to now by Lagrangian parcel models. However, we think what is going on would be much clearer if convective eddies could be described as circulation systems, rather than parcels.

The simplest approach to take is to model climatological convection as a forced dissipative system – such will likely have steady state solutions that can change on slow

time scales. This is done by using a vorticity equation for large eddies, the mixing by the smaller eddies parameterized with boundary layer scaling arguments, and a prescribed forcing. We initially leave out any large scale wind and assume a 2-D x, z structure. The forcing of convection is from sensible fluxes of surface heating linked to an equation for transport of buoyancy. Although there are many interesting "interaction" questions deriving from the known attraction and repulsion properties of multiple vortices, it is probably best first to establish what the single vortices look like in the context of an atmospheric boundary layer. Keeping this context is important or otherwise results may have less usefulness than existing boundary layer parameterizations. In other words, to be useful, we must be able to reproduce Monin-Obukhov similarity theory [Monin and Obukhov, 1954] and other properties of the ABL as revealed by LES simulations or observations. We expect that anything useful will require numerical solution by partial differential equations, but they should be intrinsically simpler ones than used for LES. What makes them simpler is that they are non-turbulent, since the turbulence is to be parameterized and thus they should require much less computer time than LES simulation. The convective-scale motion is explicitly resolved for a Boussinesq fluid (density is assumed to be constant except for buoyancy term) while the turbulence, including shear effects, is parameterized.

3.2.1 Thermal Balance

To proceed, the term Q in Eq. (3.1) is divided into 3 distinct components:

$$Q = Q_C + Q_S + Q_L, \tag{3.2}$$

where Q_C is the contribution of the large scale convective eddies, Q_S that of small scale turbulence and Q_L everything else including large scale radiative cooling and evaporative cooling. For a steady state, all of these terms must balance.

The net effect of surface heating is to warm the near surface layers to higher temperatures until a new equilibrium is established. The Q_L will adjust to give some new T. In general, this may be quite complicated. However, it is simply illustrated by assuming that $Q_L(T) = Q_L(T_0) + \Delta T\, d/dT\,(Q_L(T_0))$, where T_0 is the temperature before the added surface heating, so that we assume a balance:

$$Q = Q_S + Q_C + C\Delta T = 0, \tag{3.3}$$

where C is the coefficient of the Taylor expansion. We assume that (3.3) is not only an area average description but also a local description of balances and for non-equilibrium. Thus, we can represent Q_S by surface heating and a turbulent parameterization, and Q_C by the explicit convective dynamics in Eq. (3.1).

The thermodynamic equation for the atmospheric boundary layer is governed by the first law of thermodynamics and written in terms of potential temperature for convective-scale θ as a deviation from background potential temperature θ_0:

$$\frac{\partial\theta}{\partial t} = -u\frac{\partial(\theta+\theta_0)}{\partial x} - w\frac{\partial(\theta+\theta_0)}{\partial z} + \frac{\partial}{\partial x}(K_h\frac{\partial(\theta+\theta_0)}{\partial x}) + \frac{\partial}{\partial z}(K_h\frac{\partial(\theta+\theta_0)}{\partial z}) + C_\theta\theta, \tag{3.4}$$

where u, w denotes horizontal and vertical velocity for explicit convective motion respectively as a function of the coordinates x, z and of time t, K_h is the eddy diffusivity coefficient for heat and assumed to be the same for vertical and horizontal, and C_θ is a cooling coefficient. The first two terms on the right-hand side of Eq. (3.4) are

temperature advection components by resolved convective-scale motion in x and z. The third and fourth terms are small-scale temperature mixing parameterized by eddy diffusivity, in which the turbulence flux is proportional to local gradient of mean fields. The last term is the integrated response of the large scale background fields to the forced surface heating parameterized as a cooling effect; and it is expected to balance surface heating so as to reach an equilibrium climatological steady-state. The cooling term is approximated as a linear function of temperature perturbation as $C_\theta \theta$ from large scale equilibrium derived from Eq. (3.3), where C_θ is a restoring term with a time scale of 1 day. For simplicity, C_θ is taken to be a constant of 4 day^{-1} ~ -4.0×10^{-5} s^{-1} [Betts, 2000]. The background potential temperature is prescribed as a function of z.

Rewriting Eq. (3.4) in flux form by using the 2-D continuity equation $\frac{\partial u}{\partial x} + \frac{\partial w}{\partial z} = 0$, and then taking horizontal average gives, together with $\overline{w\theta_0(z)} = \theta_0 \overline{w(z)} = 0,$

$$\frac{\partial \overline{\theta}}{\partial t} = -\frac{\partial \overline{w\theta}}{\partial z} + \frac{\partial}{\partial z}(K_h \frac{\partial(\overline{\theta + \theta_0})}{\partial z}) + C_\theta \overline{\theta}, \tag{3.5}$$

where overbar stands for horizontal average. Integrating Eq. (3.5) from surface to convective boundary layer top gives

$$\int_0^{top} \frac{\partial \overline{\theta}}{\partial t} dz = -\overline{w\theta}\Big|_0^{top} + K_h \frac{\partial(\overline{\theta + \theta_0})}{\partial z}\Big|_0^{top} + \int_0^{top} C_\theta \overline{\theta} dz. \tag{3.6}$$

For a steady state $\frac{\partial \theta}{\partial t} = 0$, and for zero convective perturbation in velocity and temperature fields at the bottom and top of CBL, Eq (3.4) reduces to

$$K_h \frac{\partial(\overline{\theta + \theta_0})}{\partial z}\Big|_0^{top} = H_s - H_{ent} = -\int_0^{top} C_\theta \bar{\theta} dz\,, \tag{3.7}$$

where H_s is the surface heat flux and H_{ent} is the entrainment heat flux at the top of convective boundary layer. In other words, for a climatological equilibrium CBL, the surface heating (i.e. the driver of convection) and the entrainment heat flux forced by the surface heating need to be balanced by the vertical integration of the cooling term. Eq. (3.7) is equivalent in terms of thermal balance to the zero-order hypothetical steady-state mixed layer model for an equilibrium convective boundary layer over land [Betts, 2000].

3.2.2 The 2-D Vortex Structure Described by Fluid Dynamics

We first assume background geostrophic wind to be zero for simplicity and hence a free convective boundary layer. By the definition of vorticity,

$$\eta = \nabla \times V = \frac{\partial u}{\partial z} - \frac{\partial w}{\partial x}\,, \tag{3.8}$$

the vorticity equation is obtained by differentiating vertical and horizontal momentum equations with respect to x and z, respectively, and the pressure term is eliminated. The dynamic equation for vorticity is

$$\frac{\partial \eta}{\partial t} = -u\frac{\partial \eta}{\partial x} - w\frac{\partial \eta}{\partial z} + \frac{\partial}{\partial x}(K_m \frac{\partial \eta}{\partial x}) + \frac{\partial}{\partial z}(K_m \frac{\partial \eta}{\partial z}) - \frac{\partial b}{\partial x}, \tag{3.9}$$

where u, w denotes horizontal and vertical velocity associated with convective-scale circulation, K_m is the momentum eddy diffusivity, and b is the buoyancy,

$$b = g\frac{\theta}{\theta_0}\,, \tag{3.10}$$

as the ratio of resolved eddy potential temperature θ to background values θ_0 when the humidity contribution is neglected, and where g is the gravitational acceleration. The buoyancy force results from the density difference between the parcel and surrounding environment, which can be expressed as the potential temperature difference.

An eddy-diffusivity approach is feasible to parameterize small scale motions in terms of resolved convective-scale fields as an analogue to molecular diffusion, with K_m for momentum and K_h for heat. Such an approach is appropriate when the transfer is dominated by small eddies in a neutral or moderately stably stratified ABL whose length scale is relatively small comparing to the length scale of vertical variations of mean fields. The eddy viscosity K acts in both dimensions and is to be parameterized. The important point will be that K does not include motions on the scale of our large convective eddies but rather only the smaller motions that act to dissipate the large eddies and are generated by them. We assume the same diffusivity coefficient for vertical as that for horizontal in that small scale motions are usually more isotropic. We also assume that mixing is applied to vorticity, a conservative quantity.

The stream function ψ is a parameter usually used for two-dimensional and nondivergent flow, with a value that is constant along each streamline. A streamline is the line with its tangent at any point in a fluid parallel to the instantaneous velocity of the fluid at that point. The difference between the values of the stream function at any two points gives the mass or volumetric flux through a line connecting the two points. For an incompressible flow, it is connected to vorticity through a Poisson equation,

$$\frac{\partial^2 \psi}{\partial x^2} + \frac{\partial^2 \psi}{\partial z^2} = \eta \,. \tag{3.11}$$

The vorticity-stream function form of the Navier-Stokes equations is attractive for study of 2-D incompressible flow and provides better physical insight to the physical mechanisms than the formulation in terms of velocity u, w and pressure p. Such a formulation and its implementation eliminate the pressure field and ensure the mass continuity $\frac{\partial u}{\partial x}+\frac{\partial w}{\partial z}=0$ automatically; hence it avoids some numerical problems arising from discretization of continuity equations [Ferziger and Peric, 1996]. The velocity components in the x- and z- directions at a given point are given by the partial derivatives of the stream function at that point:

$$V=(u,w)=\hat{j}\times\nabla\psi=(\frac{\partial\psi}{\partial z},-\frac{\partial\psi}{\partial x}). \tag{3.12}$$

3.2.3 Closures

The above equations can be resolved when the eddy diffusivity coefficients K_m and K_h are parameterized. We follow a parameterization derived by Toren and Mahrt [1986], which was also used in the National Center for Atmospheric Research (NCAR) Community Atmosphere Model version 3 [Holtslag and Boville, 1993]. The application of such a parameterization in this study represents only small scale eddies and is different from that in climate models, where the parameterization covers all scales of eddies. The K-profile momentum diffusivity is given according to the formula

$$K_m=ku_*z\Phi_m^{-1}(1-\frac{z}{z_i})^p, \tag{3.13}$$

where $p=2.0$, u_* is the surface friction velocity, k is the von Karman constant taken to be 0.4, z is the height above the ground, and z_i is the boundary layer height. z_i is

computed as the height of minimum horizontally averaged heat flux. The stability function is taken as $\Phi_m = 1$ for neutral conditions in that the convective circulation is explicitly simulated. For convective motion free of shear, the large eddy for small z look locally like a large scale wind, which relates u_* to convective velocity scale w_* following Moeng [2004] as

$$u_* = 0.1 w_* = 0.1 \times (\frac{g}{\theta_0} H_s z_h)^{1/3}, \tag{3.14}$$

where w_* is the convective velocity scale, g is the gravitational acceleration, θ_0 is the background temperature, and H_s denotes the surface heat flux. When z is small, this parameterization reduces to

$$K_m = k u_* z \qquad \text{for} \quad z << h, \tag{3.15}$$

which matches the diffusivity coefficient based on surface layer similarity under neutral stability. Again, no stability correction is applied for surface layer eddy diffusivity as we expect all the effects of unstable stratification is established through the explicit eddies. The eddy diffusivity for heat K_h is taken to be proportional to K_m for unstable stratification [Deardroff, 1980; Moeng, 1984; Cuijpers and Duynkerke, 1993],

$$K_h = 3 K_m . \tag{3.16}$$

With the factor $(1 - \frac{z}{h})^2$ in Eq. (3.13), the eddy mixing approaches zero at the top of the boundary layer. Free atmosphere turbulent diffusivities of $K_m = 0.1$ m^2 s^{-1} and $K_h = 0.3$ m^2 s^{-1} are applied above the boundary layer to maintain numerical stability.

3.2.4 Initial and Boundary Conditions

The initial potential temperature θ, velocity u and w for explicit convective-scale motion, are set to be zero everywhere in the computational domain. Unless otherwise mentioned, the background potential temperature profile represents a constant-temperature mixed layer topped by a layer of stably stratified, where $d\theta_0/dz$ is a positive constant. It is only a function of z and typical values are selected: 300 K throughout lowest 1 km and $d\theta_0/dz = 0.005$ K m^{-1}above 1 km.

A constant and homogenous surface heat flux H_s is specified as a bottom boundary condition, e.g., 0.05 K ms^{-1} (or about 60 Wm^{-2}) as a representative global average for H_s. For summer dry conditions, this can double to about 0.1, and for oceanic or winter-like conditions can go as small as 0.01~0.02. Thus, the range of parameter space of most interest is 0.01 to 0.1 K ms^{-1}. Sensitivity tests on surface flux will be conducted in Section 3.5.3. In principle, H_s also determines an equilibrium surface temperature T_s but this term is not needed unless we also add a prognostic equation for T_s. A surface layer from similarity theory [Monin and Obuhkov, 1954] is used to handle the constant flux boundary condition. As eddy diffusivity defined in Eq. (3.13) is consistent with surface-layer similarity, it is specified that the constant heat flux goes into the lowest atmospheric layer above the surface through the relationship (it cannot go anywhere else)

$$-K_h \frac{\partial \theta}{\partial z} = H_s, \text{ i.e. } \theta(1) = \theta(2) + H_s dz / K_h, \tag{3.17}$$

with K_h defined in Eq. (3.16). Here $\theta(1)$ is the temperature at the lowest model layer, $\theta(2)$ is the temperature of the layer above the lowest layer, and dz is vertical space interval. Eq. (3.17) thus gives the bottom boundary condition for temperature. The unique property of surface layer is that the turbulent fluxes are little changed with height (a "constant-flux" layer). A typical surface layer has a height of about 10% of the boundary layer height. We simply take the first 100 m as the surface layer and the eddy diffusivities defined by Eq. (3.13) and Eq. (3.16).

Surface homogeneous heating across the domain cannot initiate convection unless small random perturbations are superimposed. A random perturbation is introduced as random numbers equally distributed between -0.5 and 0.5 for the first model hour and then shut down. A perturbation of temperature field is applied with amplitude of 0.1 K in the lowest 1 km every 600 s. Moreover, a random perturbation of surface heat flux is applied at every time step with a 10% amplitude of the flux value.

At the surface, a no-slip boundary condition is applied to velocities of u and w. The no-penetrate, no-slip boundary condition can be written in terms of the stream function ψ with

$$\psi = C\,,\ \frac{\partial \psi}{\partial n} = 0\,, \tag{3.18}$$

where C is a constant and taken as 0, $\frac{\partial}{\partial n}$ is the normal derivative to the boundary at a given point. One of the main difficulties in numerical simulation of 2-D Navier-Stokes equations in vorticity-stream function formulation is that when the vorticity is updated in time by the momentum equation (3.9), there is no definite boundary condition for vorticity [Quartapelle, 1983]. The approach to overcome the difficulty is to solve the

stream function with a Dirichlet boundary condition $\psi = 0$, then to apply the no-slip boundary condition of $\frac{\partial \psi}{\partial n} = 0$ to calculate the vorticity at the bottom boundary by Eq. (3.11). Thus, $\frac{\partial \psi}{\partial n} = 0$ is enforced through the vorticity boundary condition [Wang and Liu, 2002]. The numerical implementation of such a method will be discussed in Section (3.3.2).

No mass flow through the top gives the upper boundary condition of zero stream function $\psi = 0$. The absence of a convective circulation at the model top results in the boundary conditions of convective velocity ($u = w = 0$), vorticity $\eta = 0$ and temperature $\theta = 0$. However, the reflection of gravity waves for rigid-lid boundary conditions of $\eta = 0$ and $\theta = 0$ can cause numerical instability and therefore Neumann boundary conditions are specified instead as $\frac{\partial \eta}{\partial z} = 0$ and $\frac{\partial \theta}{\partial z} = 0$. A radiative upper boundary condition [e.g. Klemp and Durran, 1983] would be better to allow the transmission of gravity waves.

At the lateral boundaries, Neumann boundary conditions are assumed for velocities and temperature: $\frac{\partial u}{\partial x} = \frac{\partial w}{\partial x} = \frac{\partial \theta}{\partial x} = 0$; vorticity is set to be equal to zero: $\eta = 0$. Symmetry planes have a constant stream function, and the absolute value of stream function is not important in that only the gradient of stream function decides the velocity. In order to eliminate background large scale flow, the side boundary conditions for ψ needs to be chosen as the same value on both sides; for simplicity, $\psi = 0$ is imposed.

3.3 Numerical Methods

We use an efficient and simply implemented scheme on a non-staggered grid. As it is not an objective to develop an improved numerical scheme, anything that works is satisfactory provided it is not too slow to get anywhere. This means in particular, that any codes we initially develop should be done with simple finite-difference schemes and not very many grid-points. A non-staggered (colocated) uniform grid (all variables are stored at the same set of grid points) is chosen because it is the easiest to implement. Earlier work has suggested that a non-staggered grid can be numerically unstable for computing incompressible Navier-Stokes flow [Harlow and Welch, 1965; Ferziger and Peric, 1996; Dormy, 1999]. Chiam et al. [2003] have applied a non-staggered mesh to study incompressible Rayleigh-Benard convection and proved its numerical stability to integrate Navier-Stokes equation for simple geometries [Chiam et al., 2003]. We use the numerical approaches suggested in Chiam et al. [2003], including semi-implicit second-order-accurate finite-difference scheme, operator-splitting method and fast direct methods for elliptic equations. Such a simple finite-difference method is more directed toward a local cell representation than would be a spectral scheme. Operator-splitting reduces the algorithm at each time step to separable elliptic equations. Such equations can be solved by a fast direct method, in particular cyclic reduction, which is more computationally efficient and more accurate than general iterative methods in the sense that it contains no convergence error.

3.3.1 Time Integration Method

An operator-splitting method, also called a fractional step method, is used for time integration. To facilitate our discussion for numerical methods, we rewrite the Eqs. (3.4) and (3.9) using that θ_0, K_m and K_h are only functions of z as

$$\frac{\partial \theta}{\partial t} = [-(v.\nabla)(\theta + \theta_0) + C_\theta \theta + \frac{\partial K_h}{\partial z}\frac{\partial \theta_0}{\partial z}] + K_h \nabla^2 \theta + \frac{\partial K_h}{\partial z}\frac{\partial \theta}{\partial z}, \tag{3.19}$$

$$\frac{\partial \eta}{\partial t} = [-(v.\nabla)\eta - \frac{\partial b}{\partial x}] + K_m \nabla^2 \eta + \frac{\partial K_m}{\partial z}\frac{\partial \eta}{\partial z}. \tag{3.20}$$

First, the terms grouped in brackets in Eqs (3.19) and (3.20) are integrated explicitly to an intermediate field, which are linear terms and non-linear terms with low-spatial derivatives. Second, the remaining two diffusion-related terms in Eqs. (3.19) and (3.20) are added to the intermediate fields by implicit integration. The numerical method implementation below is demonstrated by temperature equation (3.19) as an example, as vorticity equation (3.20) is treated in a similar fashion. Let's assume at the n'th time step $t_n = n\Delta t$, fields θ^n and η^n are advanced to the next time step θ^{n+1} and η^{n+1} at time $t_{n+1} = t_n + \Delta t$ as follows:

(1) The explicit steps advance the field θ^n and η^n to an intermediate field θ^* and η^* using an Adams-Bashforth method of second-order accuracy. Denote the expressions in brackets of Eq. (3.19) by $N[\theta, V]$,

$$\theta^* = \theta^n + \frac{\Delta t}{2}(3N[\theta^n, V^n] - N[\theta^{n-1}, V^{n-1}]). \tag{3.21}$$

For the first time step, a second-order-accurate Runge-Kutta method [Ferziger and Peric, 1996] is used, which is self-starting, i.e. it doesn't require data prior to the current time step, to avoid unavailable values at time $t = -\Delta t$ in (3.21).

(2) The intermediate field θ^* is then advanced to the temperature field θ^{n+1} by applying an implicit Crank-Nicolson method to the terms outside the brackets for using θ^n as initial data

$$\frac{\theta^{n+1}-\theta^*}{\Delta t}=\frac{K_h}{2}(\nabla^2\theta^{n+1}+\nabla^2\theta^n)+\frac{1}{2}\frac{\partial K_h}{\partial z}(\frac{\partial\theta^{n+1}}{\partial z}+\frac{\partial\theta^n}{\partial z}).$$

Rearrange above equation as

$$\nabla^2\theta^{n+1}+\frac{1}{K_h}\frac{\partial K_h}{\partial z}\frac{\partial\theta^{n+1}}{\partial z}-\frac{2}{K_h\Delta t}\theta^{n+1}=-\frac{2}{K_h\Delta t}\theta^*-\nabla^2\theta^n+\frac{1}{K_h}\frac{\partial K_h}{\partial z}\frac{\partial\theta^n}{\partial z}. \quad (3.22)$$

Eq. (3.22) is an elliptic equation and separable with its boundary conditions. Such can be resolved by the cyclic reduction method using a fast direct solver sepx4 from the FISHPACK library provided by NCAR [Swarztrauber and Sweet, 1973; Swarztrauber et al.; http://www.cisl.ucar.edu/css/software/fishpack/], which solves a separable elliptic equation in the form of

$$a(x)\frac{\partial^2 u}{\partial x^2}+b(x)\frac{\partial u}{\partial x}+c(x)u+\frac{\partial^2 u}{\partial y^2}=F(x,y)$$

on a rectangle region. In our case, the coefficients are specified as

$$a(z)=1,\ b(z)=\frac{1}{K_h}\frac{\partial K_h}{\partial z},\ c(z)=-\frac{2}{K_h(z)\Delta t}, \text{ and}$$

$$F(z,x)=-\frac{2}{K_h\Delta t}\theta^*-\nabla^2\theta^n+\frac{1}{K_h}\frac{\partial K_h}{\partial z}\frac{\partial\theta^n}{\partial z}.$$

3.3.2 Space Discretization Method

The space-differencing is carried out on an equidistant non-staggered grid with (i,k) denoting $(i\Delta x,k\Delta z)$, where Δx and Δz are horizontal and vertical spatial resolution.

The first and second-order spatial derivatives are approximated by second-order centered differences, such as,

$$\frac{\partial\theta(i,k)}{\partial x}=\frac{\theta(i+1,\,j)-\theta(i-1,\,j)}{2\Delta x} \tag{3.23}$$

$$\frac{\partial^2\theta(i,k)}{\partial x^2}+\frac{\partial^2\theta(i,k)}{\partial z^2}=\frac{\theta(i+1,k)-2\theta(i,k)+\theta(i-1,k)}{\Delta x^2}+\frac{\theta(i,k+1)-2\theta(i,k)+\theta(i,k-1)}{\Delta z^2} \tag{3.24}$$

Neumann boundary condition is implemented as a one-sided approximation of 1st order at the top and 2nd order at the lateral boundaries, for example,

$$\frac{\partial\theta(i,N_z)}{\partial z}=\frac{\theta(i,N_z)-\theta(i,N_z-1)}{\Delta z}=0 \text{ gives } \theta(i,N_z)=\theta(i,N_z-1),$$

where N_z denotes the top layer;

$$\frac{\partial\theta(1,k)}{\partial z}=\frac{-\theta(3,k)+4\theta(2,k)-3\theta(1,k)}{\Delta z}=0 \text{ gives } \theta(1,k)=(-\theta(3,k)+4\theta(2,k))/3,$$

where 1 denotes the left side of the simulation domain.

As mentioned in Section (3.2.4), the no-slip condition $\frac{\partial\psi}{\partial n}=0$ is implemented by the vorticity boundary condition. Eq. (3.11) is approximated at the surface, i.e. $k=1$, as $\eta(i,1)=\frac{\psi(i+1,1)-2\psi(i,1)+\psi(i-1,1)}{\Delta x^2}+\frac{\psi(i,2)-2\psi(i,1)+\psi(i,0)}{\Delta z^2}$. Combining with the boundary condition $\psi(i,1)=0$ in (3.18), we have

$$\eta(i,1)=\frac{\psi(i,2)+\psi(i,0)}{\Delta z^2}, \text{ together with } \frac{\partial\psi}{\partial n}=\frac{\partial\psi}{\partial z}=\frac{\psi(i,2)-\psi(i,0)}{2\Delta z}=0,$$

leading to the bottom boundary condition for vorticity as $\eta(i,1)=\frac{2\psi(i,2)}{\Delta z^2}$ [Wang and Liu, 2002].

The equations (3.4) and (3.9)-(3.12) are solved with the following sequence at each time step:

1) Given an initial temperature field, the temperature at next time step is updated by Eq. (3.4) using numerical methods of (3.21) and (3.22);

2) Eq. (3.10) is used to compute the buoyancy at the new time step;

3) The dynamic vorticity equation is then used to update the vorticity by Eq. (3.9) and numerical methods (3.21) and (3.22);

4) The Poisson equation (3.11) is solved to compute the stream-function at the new time step by the cyclic reduction method using fast direct solver hwscrt from FISHPACK library [http://www.cisl.ucar.edu/css/software/fishpack/], which solves the Helmholtz equation $\frac{\partial^2 u}{\partial x^2} + \frac{\partial^2 u}{\partial y^2} + \lambda u = F(x, y)$ approximated by standard five-point difference (3.24), where λ is a constant, for Poisson equation, $\lambda = 0$;

5) Finally, having the stream-function, the velocity components are easily obtained by Eq. (3.12) and spatial differentiation (3.23); at this point the calculation for the next time step is begun.

3.4 Model Validation

In this section, we discuss two tests to quantify the accuracy of the dynamic framework and numerical implementation of our conceptual model.

3.4.1 Validation by Analytical Solution for a Reduced Problem

The numerical treatment of the diffusion term is tested by an analytical solution to the 1-D unsteady thermal diffusion equation. The diffusion term is differentiated from

current time to next time by an implicit Crank-Nicolson scheme and solved by fast direct methods (see Section 3.3.1 for details). The 1-D heat diffusion equation is:

$$\frac{\partial \theta}{\partial t} - K \frac{\partial^2 \theta}{\partial z^2} = 0 , \tag{3.25}$$

subject to uniform initial condition $\theta = \theta(0)$, constant thermal diffusivity K, constant flux boundary condition at $z = 0$, $H = -K \frac{\partial \theta}{\partial z}$, and a semi-infinite body can be solved analytically using a Laplace transform as [e.g., Incropera and DeWitt, 2002]:

$$\theta = \theta(0) + \frac{H}{K}[2\sqrt{\frac{Kt}{\pi}} \exp(-\frac{z^2}{4Kt}) - z(1 - erf(\frac{z}{2\sqrt{Kt}}))], \tag{3.26}$$

where semi-infinite requires $\frac{L}{2\sqrt{Kt}} \geq 2$, L is the thickness of the fluid, and $erf(z)$ is error function defined by $erf(z) \equiv \frac{2}{\sqrt{\pi}} \int_0^z e^{-t^2} dt$. The horizontal average of the thermodynamic equation of our model Eq. (3.4) for constant eddy heat diffusivity K_h, zero background temperature and absence of large scale cooling effect reduces to

$$\frac{\partial \overline{\theta}}{\partial t} = -\frac{\partial \overline{w\theta}}{\partial z} + K_h \frac{\partial^2 \overline{\theta}}{\partial z^2}, \tag{3.27}$$

where an overbar denotes horizontal mean.

How can we define an analogous problem so as to best compare with the analytical solution? Set K_h in Eq. (3.27) to be 1000 m^2 s^{-1}. A large value of eddy diffusivity suppresses the development of explicit convection and leads to a typical scale of vertical velocity w on an order of 10^{-2} m s^{-1}. To satisfy the semi-infinite criterion for $t = 1$ h and $K = 1000$ m^2 s^{-1}, the condition is $L \geq 7.6$ km and hence the depth scale is 10^3

m. Scaling analysis of Eq. (3.27) thus suggests the term $K_h \frac{\partial^2 \overline{\theta}}{\partial z^2}$ is dominant relative to term $\frac{\partial \overline{w\theta}}{\partial z}$ for those conditions. A model run of grid number of 300 × 160 with spatial resolution of $\Delta x = 100\,\text{m}$ and $\Delta z = 50\,\text{m}$, covering 8 km in vertical coordinate, is made for 1 hour. The prescribed constant flux boundary condition at $z = 0$ is $H = 0.5\,\text{K m s}^{-1}$. The modeled temperature profile is compared to analytical solution in Figure 3.1. The simulation results (solid line) largely overlap with analytical solution (dotted line), indicating an accurate numerical treatment for the diffusion term.

The other run is the same as the last simulation except $K = 100\ \text{m}^2\ \text{s}^{-1}$. In this case, the explicit convection is on the same order as thermal diffusion in Eq. (3.27). Figure 3.2 shows the temperature profiles for both numerical simulation (solid line) for Eq. (3.27) and analytical solution for Eq. (3.25). The difference of solid and dotted line can be regarded as the explicitly resolved convective-scale influence by the term $\frac{\partial \overline{w\theta}}{\partial z}$, which represents the intrinsically non-local effect of the convective boundary layer. Such a non-local effect mixes the heat upward more efficiently and results in a nearly well mixed layer for temperature except near the boundaries at a result of forced boundary condition. This result is consistent with a quasi-steady analytical analysis of a planetary boundary layer model by Stevens [2002].

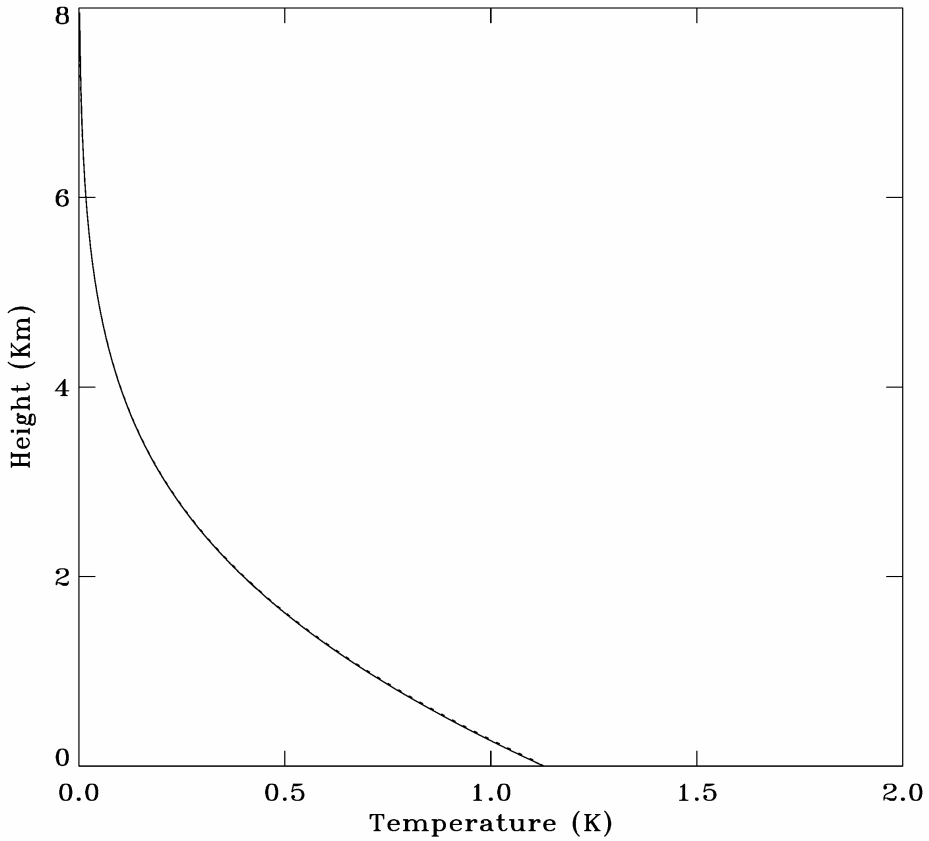

Figure 3. 1 Comparison in temperature profiles between numerically modeled (solid line) and analytical solved (dotted line) 1-D heat diffusion equation for constant boundary flux condition of 0.5 K m s^{-1} at height zero and constant thermal diffusivity of 1000 m^2 s^{-1}.

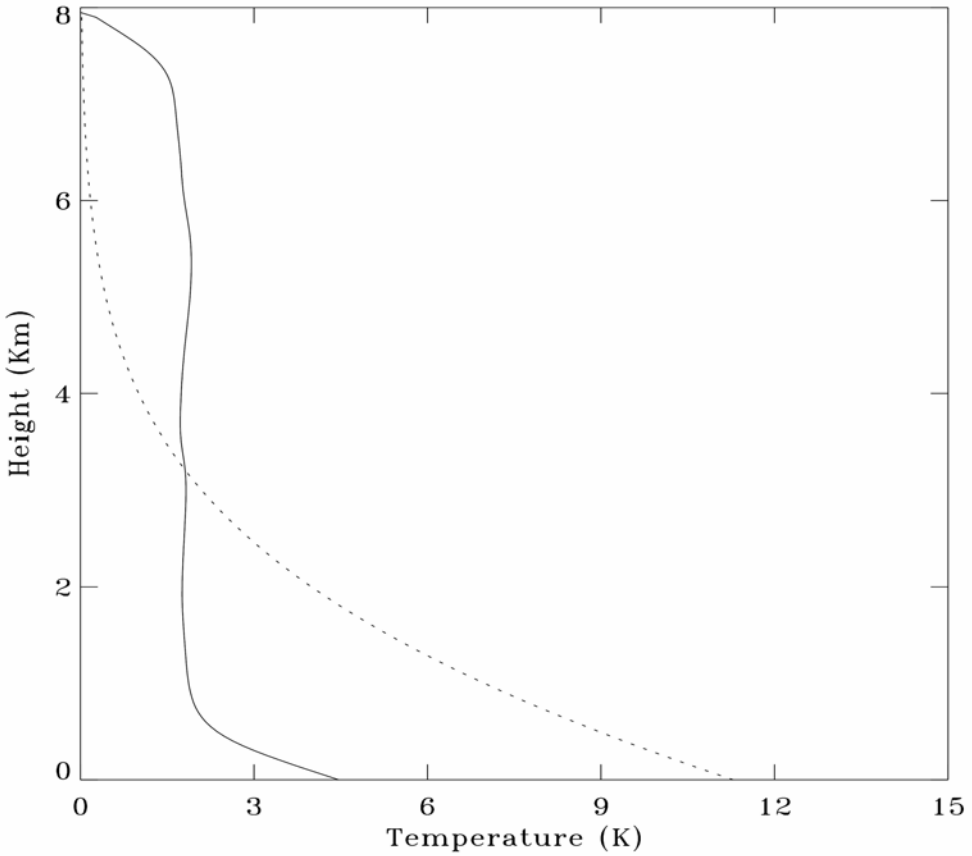

Figure 3.2 Temperature profiles of numerically modeled (solid line) 1-D heat convection-diffusion equation and analytical solved (dotted line) 1-D heat diffusion equation for constant boundary flux condition of 0.5 K m s^{-1} at height zero and constant thermal diffusivity of 100 m^2 s^{-1}.

3.4.2 Validation by Large-Eddy Simulation

Large-eddy simulation (LES) is an attractive approach to study the atmospheric boundary layer given the difficulties and limitations of direct measurement of atmospheric turbulence [Wyngaard, 1992]. The name of LES comes from the fact that it explicitly simulates the large eddies but parameterizes small ones. In LES, Navier-Stokes equations are filtered to separate resolved and subgrid-scale motions, where the filter length is taken proportional to the numerical grid size. The general idea is that the sub-scale motion carries much weaker energy than the resolvable motion, and therefore it is less important than large eddies. This technique was first applied to the atmospheric boundary layer by Deardroff [1972] and has been extensively used since then [e.g. Moeng, 1984; Schmidt and Schumann, 1989; Mason, 1989]. In this section, the model is checked by a free convective PBL case against LES results. The statistics of such flow are well documented from observations [Willis and Deardroff 1974; 1979] and LES community [Moeng, 1984; Schmidt and Schumann, 1989; Nieuwstadt et al., 1993].

3.4.2.1 Reference Case Description

The model is tested for a free convective PBL with a 3-D NCAR LES run and compared to its 2-D runs in the same case as described in Moeng [2004]. The initial profile of potential temperature θ is fixed as 300 K below 1 km, linearly increases by 5 K over the next 100 m, and then increases with a free-atmospheric lapse rate of 0.003 K m^{-1}. The 5 K temperature jump of capping inversion is imposed to make sure that the PBL wouldn't grow to near the top of the numerical domain, and it should affect the PBL growth rate but not the overall turbulence statistics [Moeng, personal communication].

The surface heat flux was set to 240 Wm^{-2} and the large scale geostropic wind is set to be 0 [Moeng, 2004].

The 3-D LES run used 200 × 200 × 100 grid points in a numerical domain of 7.5 km × 7.5 km × 2 km. The 2-D LES uses the same 3-D LES codes except all y derivatives are set to 0. The 2-D LES covers a 7.5 km × 3 km domain with 200 × 100 grid points and two runs are conducted with subgrid-scale viscosity parameter taken as 0.1 (same as the 3-D LES) and 1.0 (tenfold of that in the 3-D LES), denoting them by 2-D-A and 2-D-B, respectively. They found that 2-D-B agrees better with the 3-D LES because of the tuned viscosity and hence the thermal diffusivity. For the LES runs, the grid size in vertical direction of $\Delta z = 20\,\mathrm{m}$ is the same for 2-D and 3-D runs. In order to compare with LES, the cooling term in Eq. (3.4) of our model is turned off and two experiments are carried out: one with 75 × 40 grid points covering a 7.5 km × 2 km domain (denoted as Experiment A); the other with 75 × 60 grid points covering a 7.5 km × 3 km domain (denoted as Experiment B). For our model simulation, spatial resolutions of $\Delta x = 100\,\mathrm{m}$ and $\Delta z = 50\,\mathrm{m}$ and a time step $\Delta t = 1$ s are used. The following discussion will mainly focus on comparisons between our model results and LES from 3-D and 2-D-A runs.

3.4.2.2 Mean Profiles

We first compare the vertical profiles simulated by our model with the LES simulation of Moeng [2004]. The model outputs are averaged horizontally, including PBL height, temperature profile, heat fluxes and momentum variance. The temperature profile is then averaged over a time period of hour 3 to hour 6. The heat flux and momentum variance are averaged in time from hour 2 to hour 6, and then mapped to the normalized vertical coordinate z / z_i, where z_i is the boundary layer height. Figure 3.3

compares the time evolution of the PBL depth z_i, which is determined as the height of minimum (negative) horizontally averaged heat flux in our model. In comparison to 3-D LES model, the PBL development is considerably faster for the 2-D LES runs while moderately slower for our 2-D model. This is a consequence of the less vigorous entrainment process of our model for the same forcing and can be corroborated by a smaller entrainment heat flux in Figure 3.4c and d than that in Figure 3.4a and b. Entrainment is the process that the rising boundary layer air with initial momentum can overshoot a certain distance to the warmer free atmosphere though they are negatively buoyant, and then mix with less turbulent free atmosphere and pulling some downwards into boundary layer. The entrainment heating moves the PBL height upward at a rate of 30-40% faster than would happen without the entrainment. Our results produce a minimum entrainment heat flux at the PBL top of about -0.07 of the surface heat flux, which is about half of that by the 3-D LES (about -0.16 of the surface heat flux); on the other hand, the entrainment heat flux of 2-D LES is found to be twice as large as that of 3-D LES [Moeng, 2004].

Figure 3.4 also decomposes the total heat flux into a resolvable and a smaller scale contribution. The overall shape of total heat flux of our model is close to a linear decrease versus height and agrees well with the LES model. However, the small scale motions play a more important role in our model than that in LES due to the different consideration and treatments, which affects heat flux transport until a height of 0.4 z_i but disappears in LES at a height of 0.1 z_i. At the surface, our resolved velocities vanish from the non-slip boundary condition and therefore all the flux is transported by small scale motion, whose effect decreases with height above this level. The entrainment heat flux is

entirely contributed from the resolved-scale. In other words, the entrainment process can be explicitly simulated.

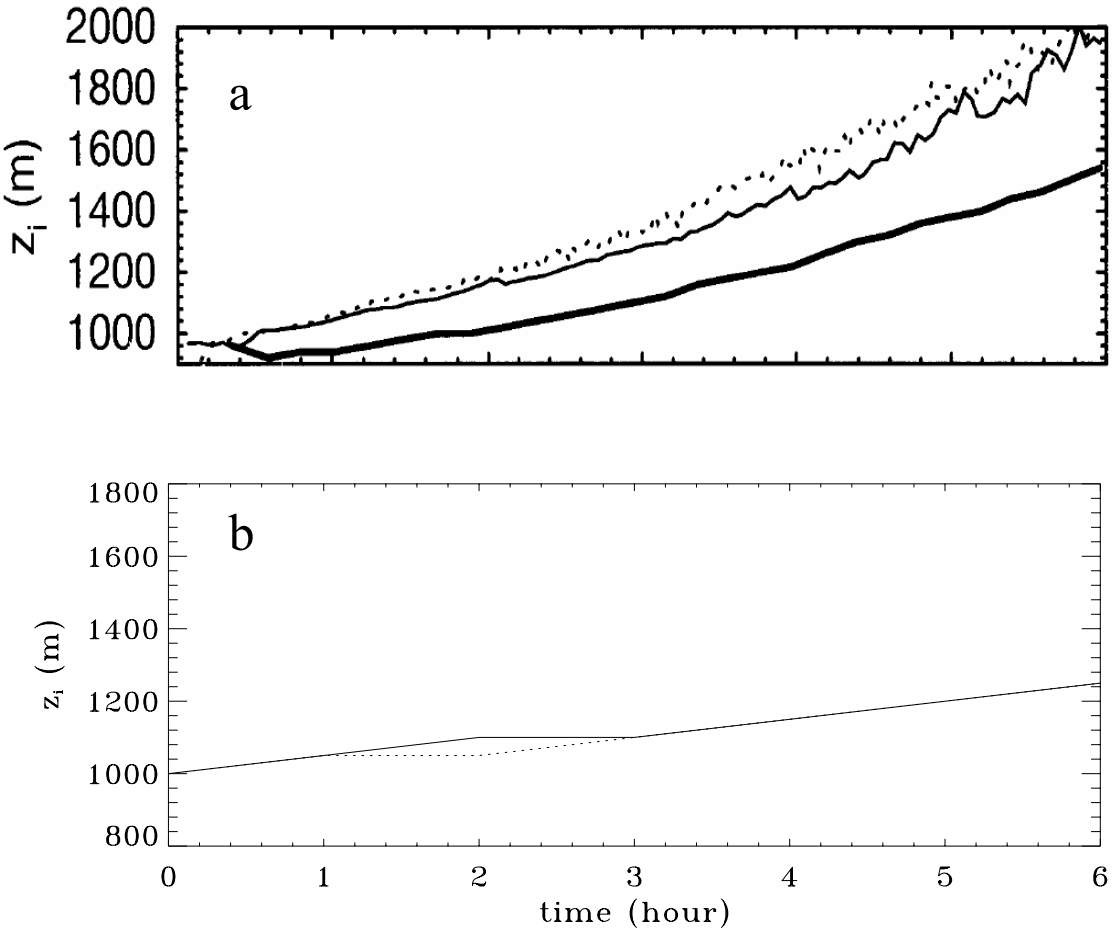

Figure 3.3 Time evolution of PBL height from a) LES with thick line for 3-D, dotted line for 2-D-A and thin solid lines for 2-D-B (Meong et al., 2004); b) our model with solid line for Experiment A and dotted line for Experiment B.

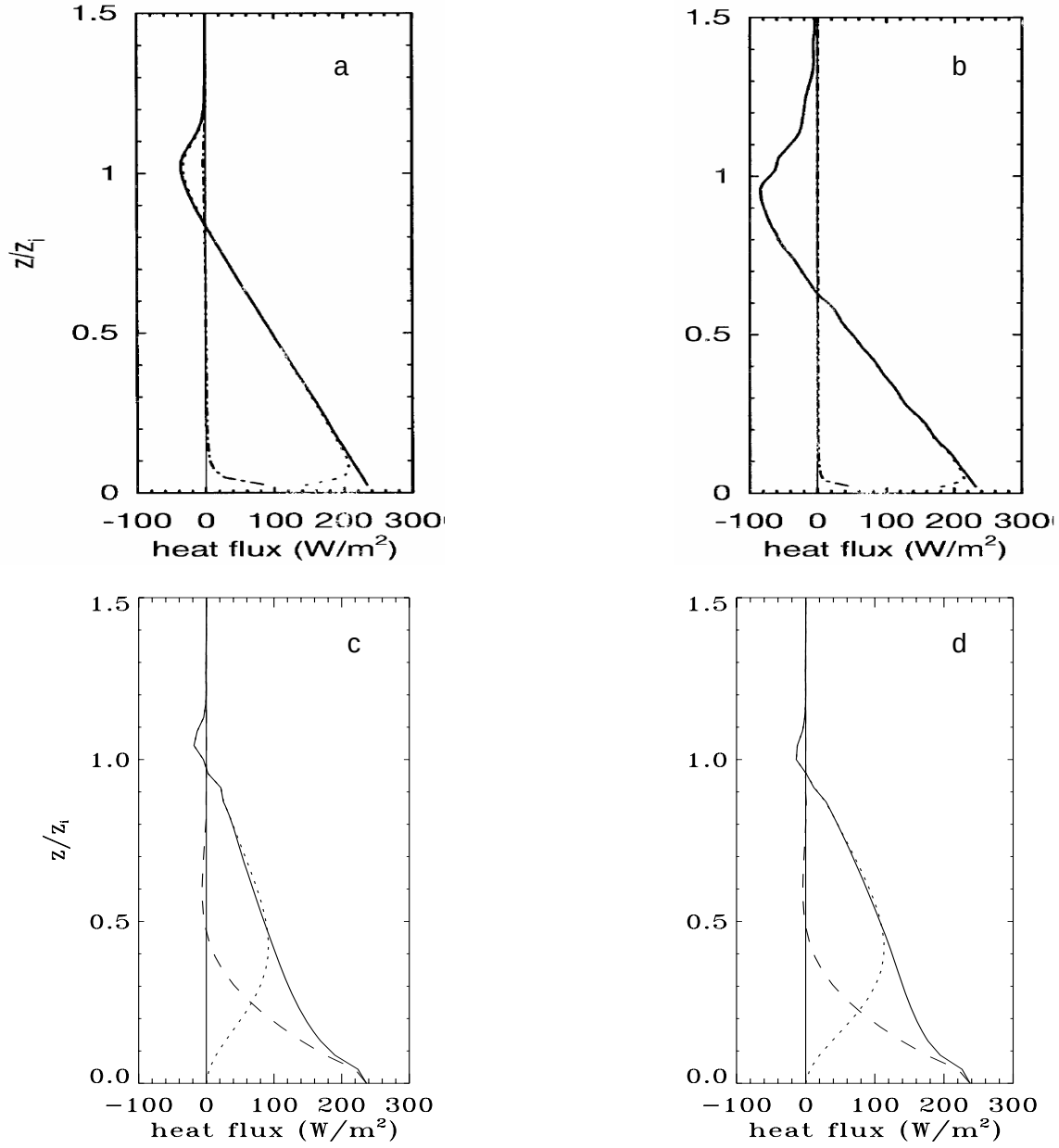

Figure 3.4 Vertical profiles of the mean heat flux from a) 3-D LES (Meong et al., 2004); b) 2-D-A LES (Meong et al., 2004); c) Experiment A of our model; d) Experiment B of our model (total as solid line, resolved scale as dotted line and small scale as dashed line).

The mean potential temperature profile is reasonably predicted by our model compared with the LES with an unstable surface layer, a nearly mixed middle layer and an overlying entrainment zone (Figure 3.5). The initial profile is shown as the dotted line in Figure 3.5b. Although the lower part of the boundary layer is heated faster by our model, the well-mixed layer is heated by approximately 4 K during the course of time integration and is in good agreement with LES. This well-mixed temperature profile can be explained by the linear decrease of total heat flux profile for quasi-steady state, which means the mean potential temperature profile does not change with time, i.e. $\frac{\partial}{\partial t}(\frac{\partial \overline{\theta}}{\partial z}) = 0 = \frac{\partial^2}{\partial z^2}(-\overline{w\theta} + K_h \frac{\partial(\overline{\theta + \theta_0})}{\partial z})$, where the terms in the rightmost bracket denotes the total heat flux (see Eq. (3.5) in Section 3.2.1 for derivation). The warmer and less well-mixed lower boundary layer may result from the smaller thermal diffusivity for small scale motions within this layer.

Figure 3.6 shows the vertical distribution of velocity variances. In comparison to 3-D LES, the u and w variances of 2-D LES are much larger and those of our model are much smaller in magnitude. The possible reasons for this discrepancy include: 1) the less energetic convective circulation produced by our model, which will be seen in Section 3.4.2.3; 2) the neglect of small scale velocity variance in our model. Our model generates a similar tendency of velocity variances as 2-D LES, in particular, the w variance peaks at mid-PBL and decreases symmetrically from that level and the u variance has two peaks. However, 3-D LES shows a maximum of w variance closer to 0.3-0.4 z_i as demonstrated by field data [Caughey and Palmer 1979; Lenschow et al., 1980].

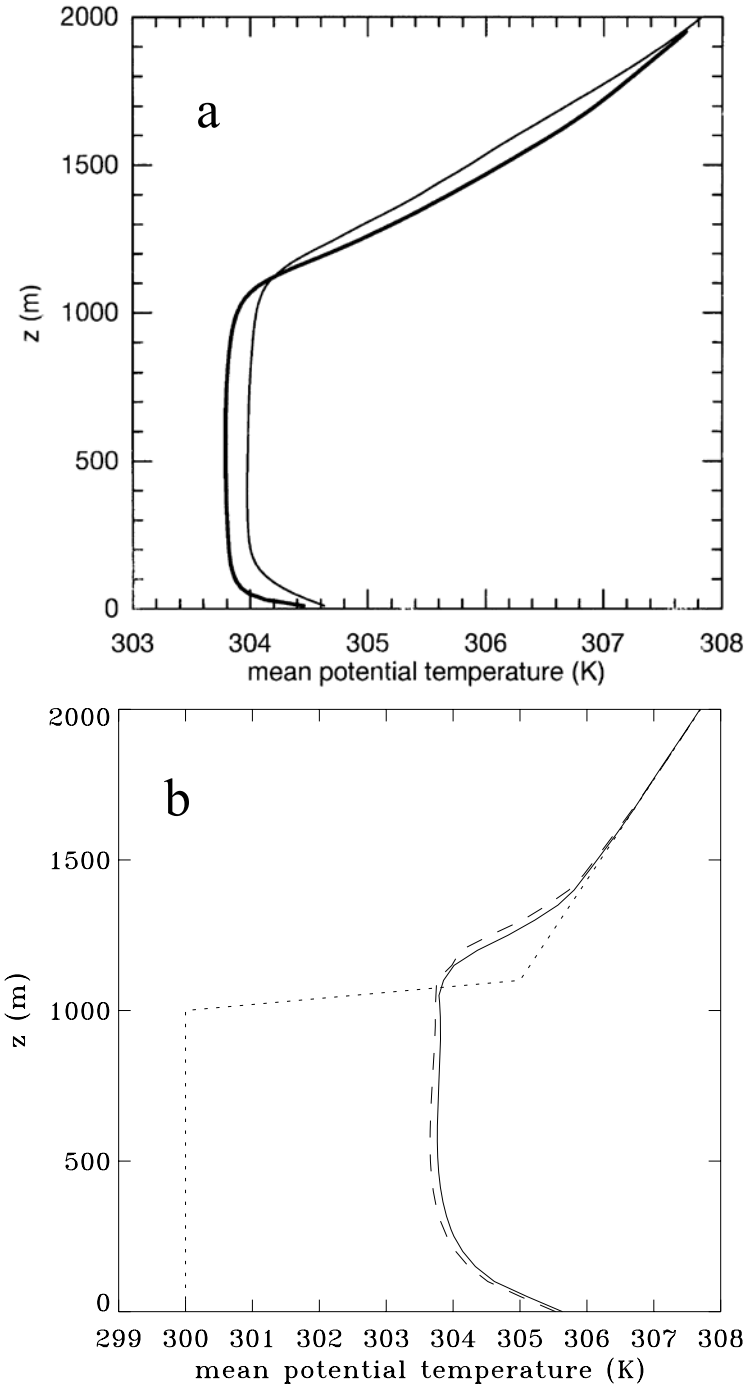

Figure 3.5 Vertical profiles of the mean potential temperature averaged over between hour 3 – 6 for initial profile as the dotted line in b from a) LES with thick line for 3-D and thin solid lines for 2D-B (Meong et al., 2004); b) our model with dashed line for Experiment A and solid line for Experiment B.

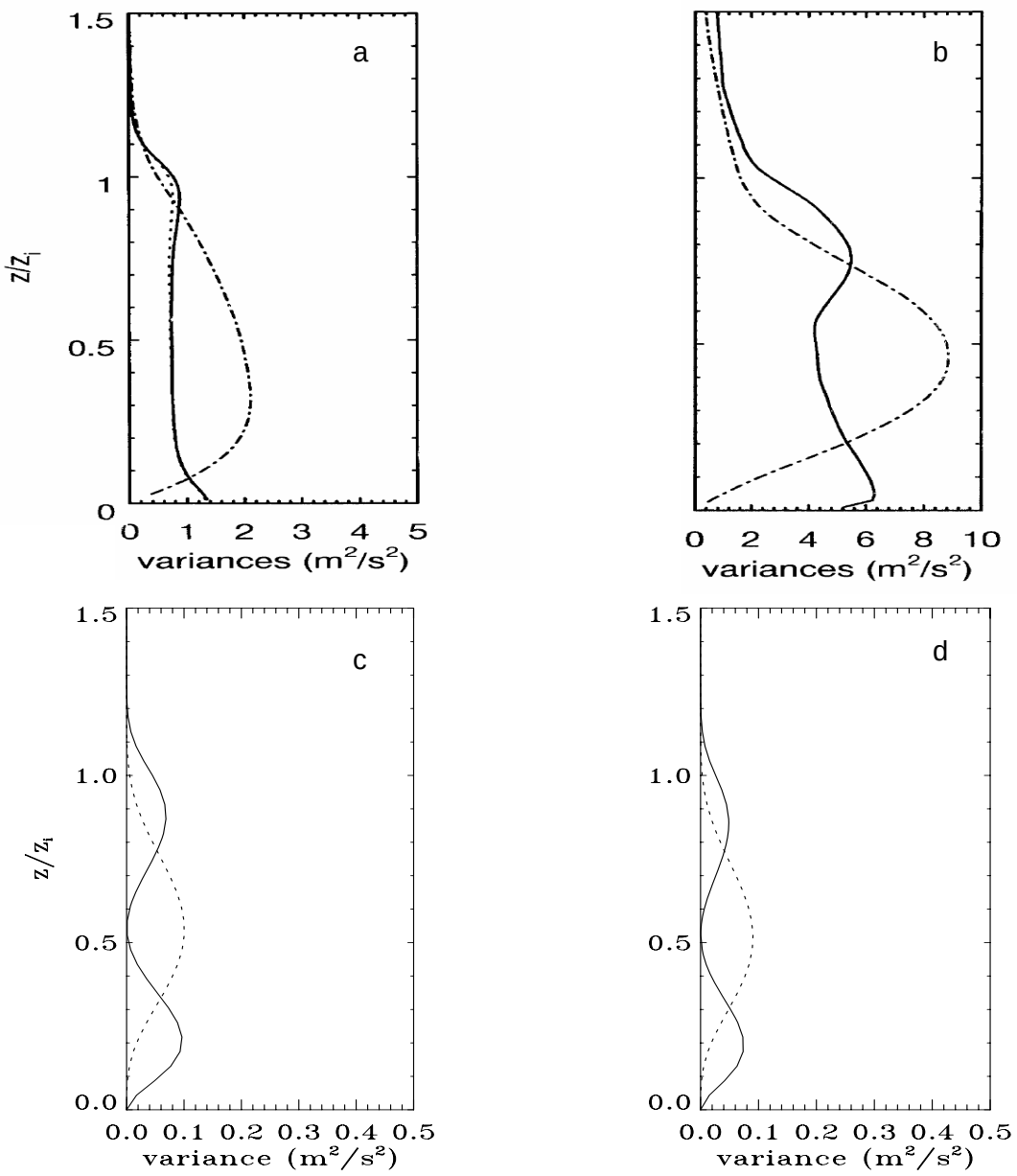

Figure 3.6 Vertical profiles of the resolved-scale velocity variance from a) 3-D LES and b) 2-D-A LES for $\overline{u^2}$ as solid line, $\overline{v^2}$ as dotted line and $\overline{w^2}$ as dotted-dashed line (Meong et al., 2004); c) Experiment A of our model and d) Experiment B of our model ($\overline{u^2}$ as solid line and $\overline{w^2}$ as dotted-dashed line).

3.4.2.3 2-D Structure

The vertical cross section of flow fields at hour 4 are shown for 3-D LES (Figure 3.7), 2-D-A LES (Figure 3.8) and our model for Experiment A (Figure 3.9). The results from Experiment B of our model are similar to those of Experiment A and thus are not shown here. At this time, the PBL depth is about 1.2 km for the 3-D LES and our model, while it is about 1.5 km for the 2-D-A LES. The three figures agree with the following properties: 1) As expected for free convection, there is no correlation between the horizontal velocity u and vertical velocity w [Moeng et al., 2004]; 2) Strong and narrow updrafts extend throughout the whole PBL, between which are weaker and broader downdrafts; 3) A characteristic eddy size is on the order of PBL depth.

It is interesting that each rising plume extends over the whole PBL in our simulation; however, only the strongest updrafts extend over the whole PBL in the LES simulation. Moreover, The LES shows several local maxima within strong updrafts but our model results show one maxima for each updraft, suggesting the updrafts contain smaller scale bubbles in LES but not for our model. In sum, it is likely that convection cells from our model are more smooth and regular because the small scale motion is parameterized and thus our model is non-turbulent as to be expected. Such single convection cells can help advance our understanding for convective boundary layers. Also, the difference lies in the magnitude of velocity. Comparing to the 3-D LES counterparts, the 2-D-A LES develops a stronger but our model produces a weaker and less energetic convection. Such also contributes to the differences in magnitudes of entrainment rates and velocity variances among those three cases. The reason why our modeled velocities are considerately smaller than those by the LES needs further

investigation. The different dynamic treatment of our model from the LES in ignoring the interaction between explicit eddies could be one reason for this difference.

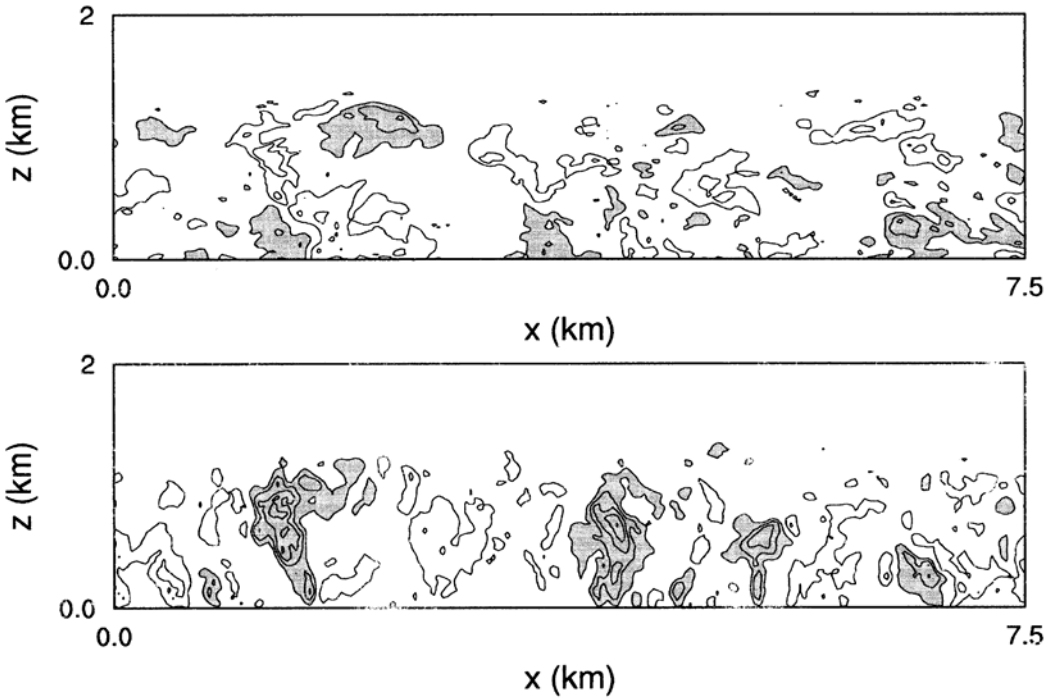

Figure 3.7 Contours of u (top) and w (bottom) velocity in an x-z cross section at hour 4 of 3-D LES with contour interval of 1 m s-1 and the gray area for positive values (Meong et al., 2004).

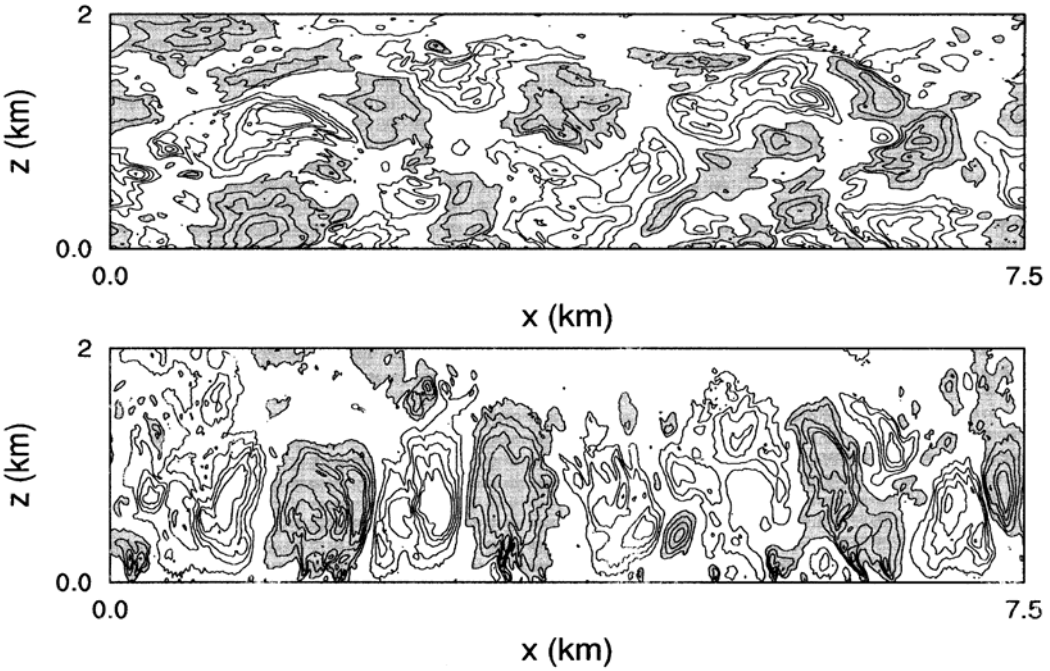

Figure 3.8 Contours of u (top) and w (bottom) velocity in an x-z cross section at hour 4 of 2-D-A LES with contour interval of 1 m s^{-1} and the gray area for positive values (Meong et al., 2004).

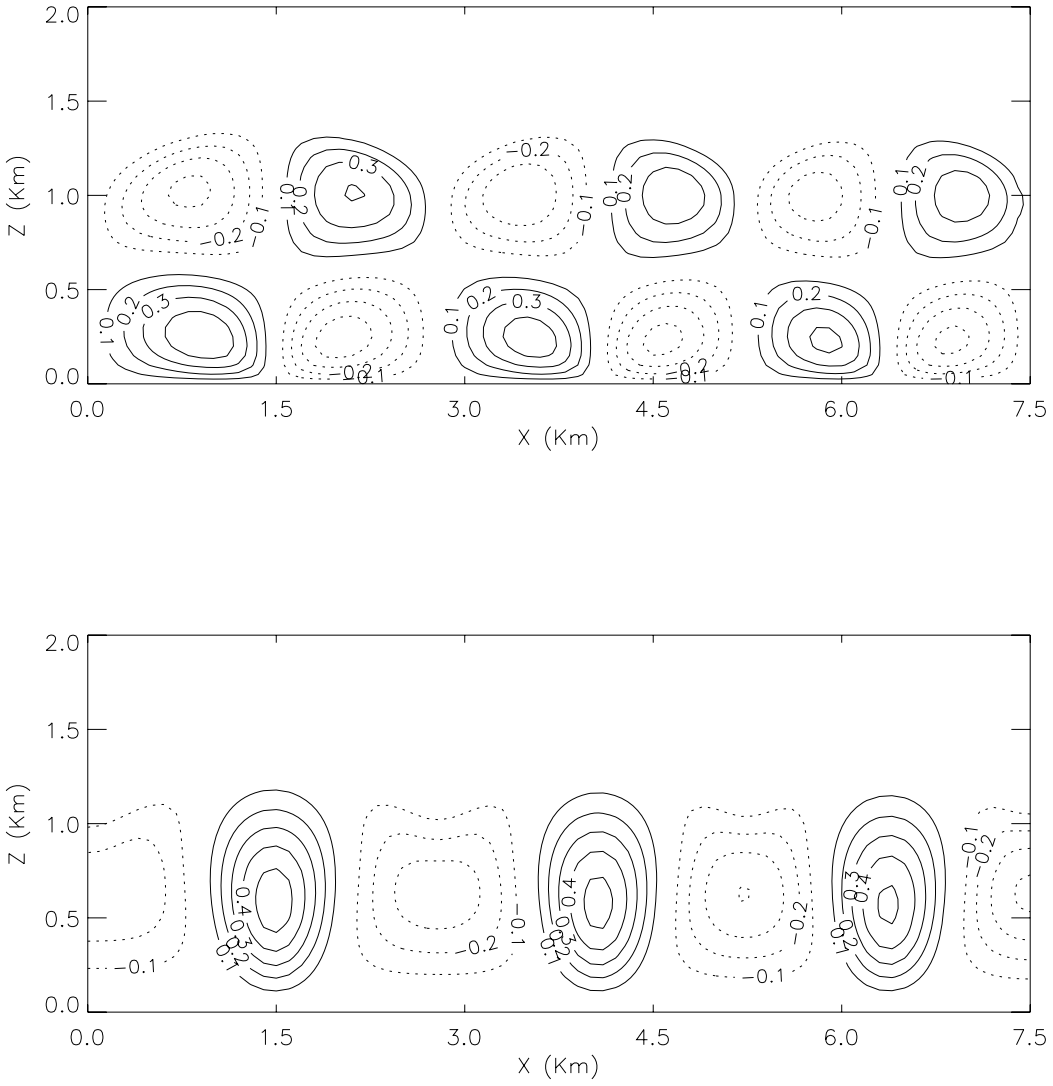

Figure 3.9 Contours of u (top) and w (bottom) velocity in x-z cross section at hour 4 for Experiment A of our model with contour interval of 0.1 m s^{-1}, where the solid line for positive values and dotted line for negative values.

3.5 Climatological Convective Boundary Layer Simulation

This section discusses the simulation results for a reference climatological convective boundary layer: a constant and homogenous surface heat flux H_s of 0.05 K m s^{-1} and a cooling coefficient C_θ of -4.0×10^{-5} s^{-1}. As mentioned in Section 3.2.4, the initial temperature profile is a function of z with 300 K throughout lowest 1 km and $d\theta_0/dz = 0.005$ K m^{-1} above 1 km. The computational domain extends horizontally and vertically over a domain size of 30 km × 4 km, where spatial resolutions are $\Delta x = 100\,\text{m}$ and $\Delta z = 50\,\text{m}$. The time step is used as $\Delta t = 1\,\text{s}$.

The targeted variables in our model are the convective scale potential temperature, vorticity, stream function and hence velocities. The model is run over 24 hours and the time average of outputs is used to approximate the climatological equilibrium state. Without the cooling term in thermodynamic equation, the PBL height will keep deepening with time for a forced constant heat flux. However, a forced dissipative system, with large scale background cooling effect to balance the surface flux, can reach a nearly steady state that changes on a very slow time scales. The PBL height will be nearly stabilized after about 6 hours of simulation and there is only a 50 m increase in PBL height for the next 18 hours.

3.5.1 2-D Spatial Structure

Figure 3.10 shows stream function contours for the convective scale field averaged over the simulation period. The contours of stream function are streamlines, which are tangent to the flow velocity at any point. The average PBL height is about 1.25 km as will be illustrated from the vertical potential temperature profile later. The flow

field shows the concentric nature of the streamlines and is composed of several similar convective cells with horizontal and vertical scales comparable with the PBL height. The convective circulation changes its direction from cell to cell. The solid and dotted lines represents positive and negative values of the stream function, respectively, corresponding to counterclockwise and clockwise circulations seen from the front. The average velocity vector field is shown in Figure 3.11, where the directed arrows are showing the direction and relative magnitude. Since the grid density is too high to show clear velocity vectors for the entire simulation domain and also the flow consists of similar spatial patterns, only part of the computational domain is shown for a horizontal range of 0-5 km, which accommodates three convective roll structures. The velocity vectors show the same cell structure as the corresponding stream function fields. The more concentrated streamlines correspond to the upward motion, indicating updrafts are more intense and narrow. When the strong ascending draught reaches near the PBL height, it is spread out and then goes downwards on both sides of it, forming counterclockwise and clockwise convective cells. Convergence occur at the lower part of the upward motion and divergence at the upper part. The descending draughts are relatively weak and broad. Here we focus on the flow spatial structure and the velocity magnitude will be discussed later.

The corresponding climatological vorticity contour lines are shown in Figure 3.12. Vorticity can be considered as the circulation per unit area at a point in the flow field, which describes the amount of spin or rotation. The faster it spins, the greater the vorticity. The direction of vorticity is perpendicular to the flow plane for 2-D flows. In Figure 3.12, the positive values denote its direction into the paper and negative values

denote the direction out of the paper. Combining Figure 3.11 and 3.12, we see an increase in vorticity (spinning faster) relates to flow convergence and a decrease in vorticity (spinning slower) relates to divergence. Concentrations of high vorticity occur in rising draughts. Coherent vortical structures are seen throughout the numerical domain. The major part of the convective boundary layer is occupied by a series of vortices with alternating directions from cell to cell. This primary structure corresponds to that seen from streamlines (Figure 3.10). The other two secondary cell lines are associated with bottom and top boundary conditions.

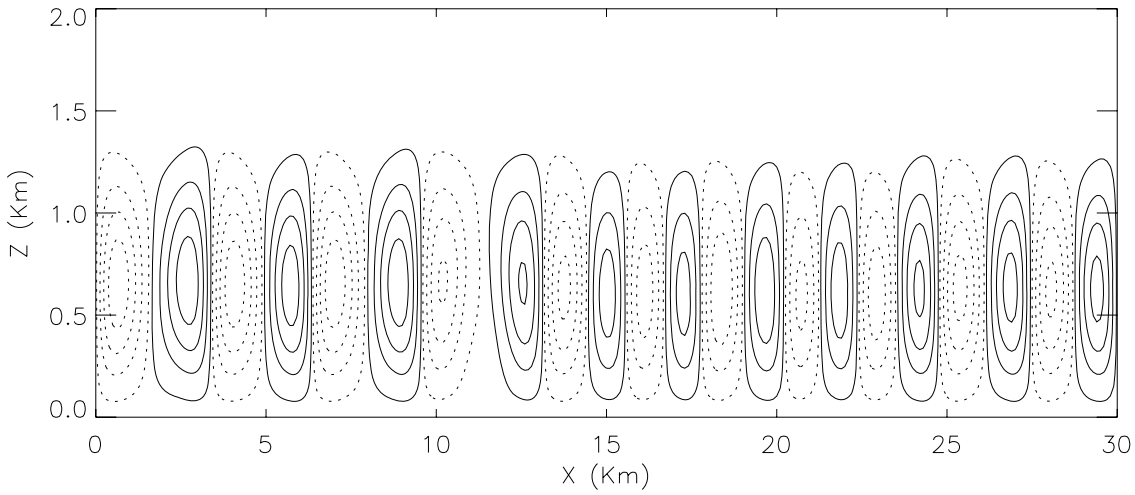

Figure 3.10 Stream function contours for the 2-D reference climatological convective boundary layer with starting value of ±5 and contour interval of 20, i.e. contours of ±5, ±25, ±45…, where the solid line for positive values and dotted line for negative values (units: m^2s^{-1}).

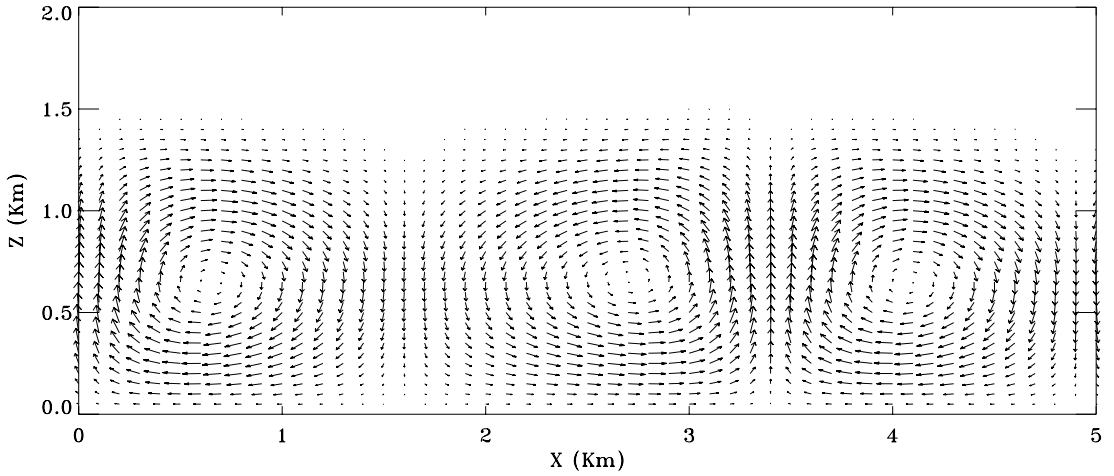

Figure 3.11 Vector plot of convective velocity for the 2-D reference climatological convective boundary layer with the directed arrows showing the direction and relative magnitude.

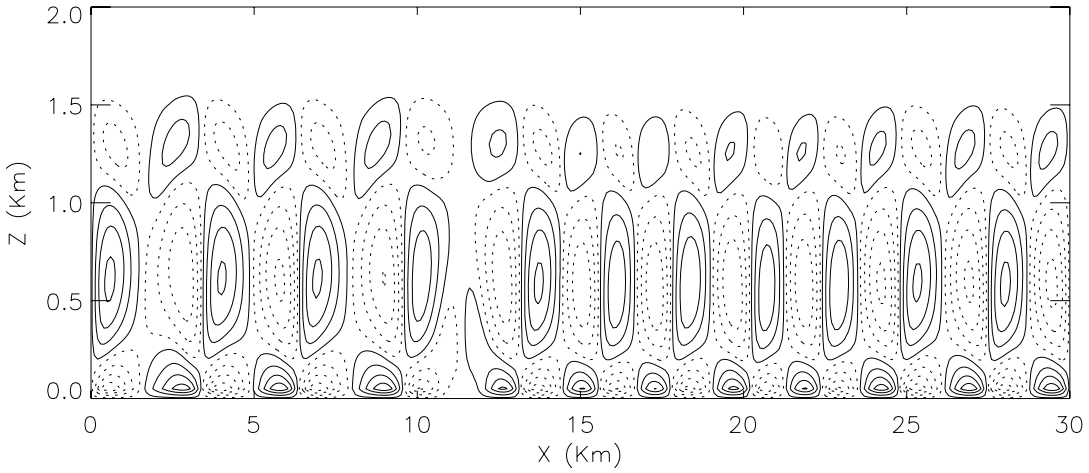

Figure 3.12 Vorticity contours for the 2-D reference climatological convective boundary layer with starting value of $\pm 1.0\times10^{-4}$ and contour interval of 3.0×10^{-4}, i.e. contours of $\pm 1.0\times10^{-4}$, $\pm 4.0\times10^{-4}$, $\pm 7.0\times10^{-4}$…, where the solid line for positive values and dotted line for negative values (units: ms^{-2}).

We now turn to the spatial structure of the convective temperature perturbation and convective velocity components for the climatological case. Figure 3.13 and 3.14 show contour plots of mean vertical velocity and temperature fields for the simulation period. Relatively strong and narrow updrafts are clearly seen extending throughout the PBL. The maximum velocity for the updrafts is about 0.2 m/s, and about -0.15 m/s for the downdrafts. The ascending motions with warmer air penetrate into the stable layer, and the cooler flows sink back on both sides of each rising draft. Some sinking motions have a horizontal scale twice as large as that of rising flow, but the others have a horizontal scale close to that of rising flow. The strongest warming happens near the land surface as a consequence of the constant bottom heating. There is a strong correlation between convective vertical velocity and potential temperature. The updrafts correspond to the upwelling isothermal lines in the temperature contour plot. There corresponds a negative temperature perturbation above each upwelling branch. This decrease in temperature results from the entrainment process when air from the surface moves up into the warmer free atmosphere and mixes with it.

The contour plot of time-averaged horizontal velocity field is shown in Figure 3.15. The maximum horizontal velocity is about 0.18 m/s for both positive and negative values. Therefore, the convective horizontal velocity is of the same order as the vertical velocity. Such can be easily understood from the continuity equation and the close horizontal and vertical length scales for the convective cells. Comparing with vertical velocity plot (Figure 3.13), it can be seen that the convergence occurs at the lower part of the upward motion and divergence at the upper part. This also explains how one vertical velocity cell is associated with two horizontal velocity cells in opposite directions.

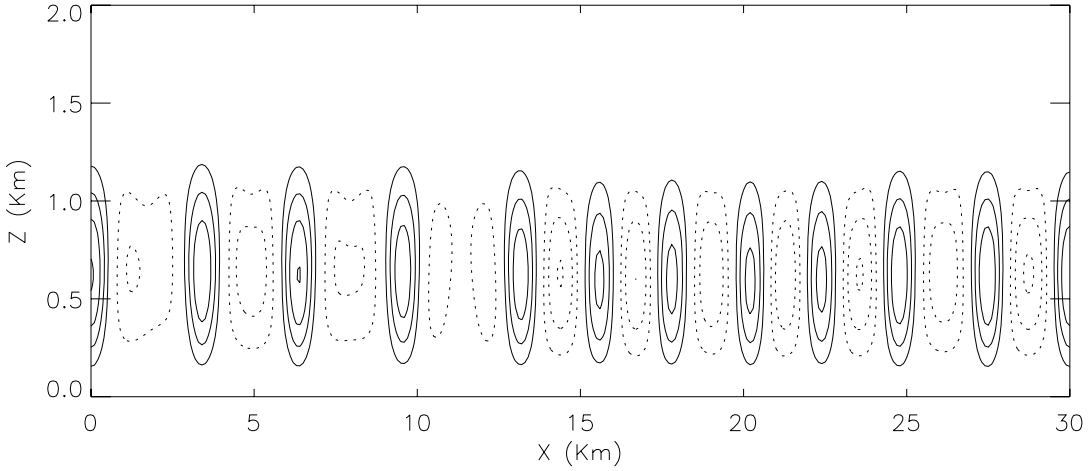

Figure 3.13 Contour plot of convective vertical velocity for the 2-D reference climatological convective boundary layer with starting value of ±0.05 and contour interval of 0.05, i.e. contours of ±0.05, ±0.1, ±0.15…, where the solid line for positive values and dotted line for negative values (units: ms^{-1}).

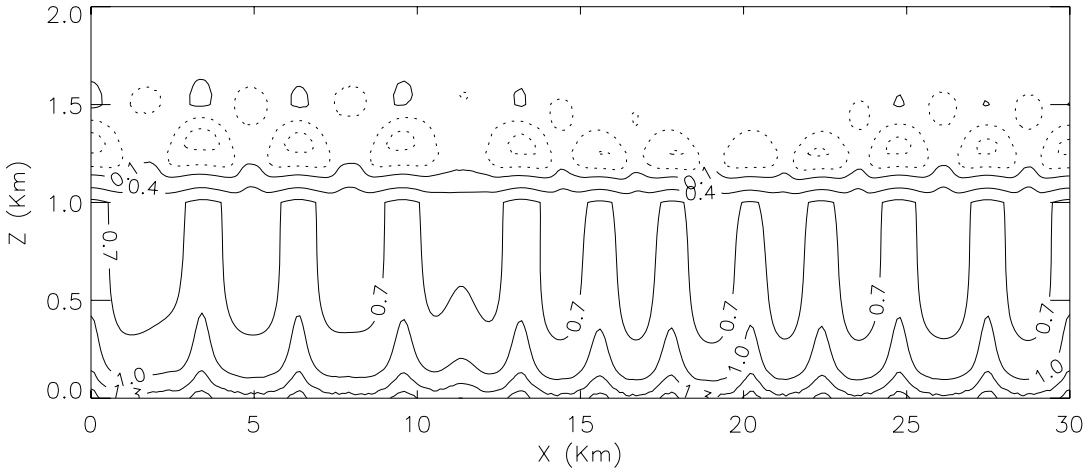

Figure 3.14 Contour plots of convective temperature fluctuation for the 2-D reference climatological convective boundary layer with starting value of ±0.1 and contour interval of 0.3, i.e. contours of ±0.1, ±0.4, ±0.7…, where the solid line for positive values and dotted line for negative values (units: K).

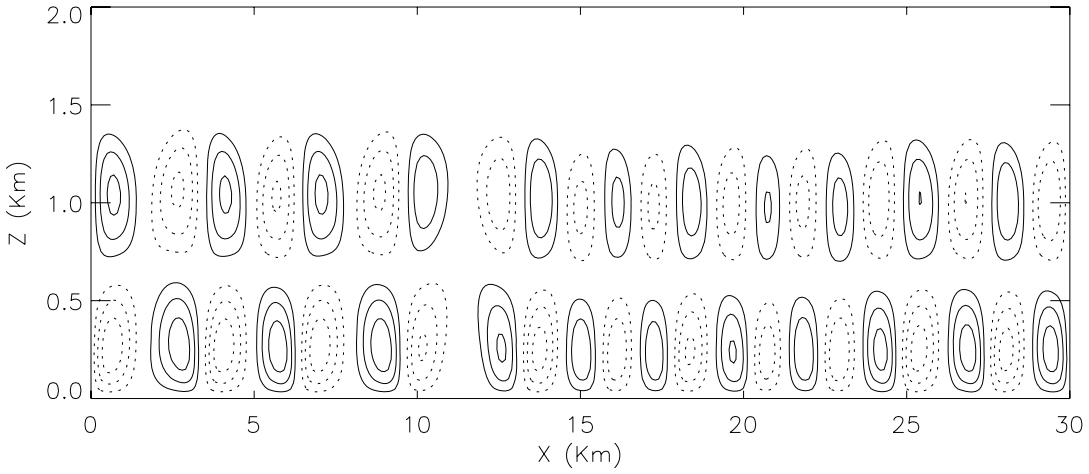

Figure 3.15 Contour plot of convective horizontal velocity for the 2-D reference climatological convective boundary layer with starting value of ±0.05 and contour interval of 0.05, i.e. contours of ±0.05, ±0.1, ±0.15…, where the solid line for positive values and dotted line for negative values (units: ms^{-1}).

3.5.2 Mean Vertical Profile

In this section, we discuss the results in terms of vertical profiles for our reference climatological convective boundary layer case. The time-averaged fields are averaged horizontally to generate the mean vertical profiles. The convective scale potential temperature profile is shown in Figure 3.16a. The ensemble potential temperature, i.e. the sum of convective scale and background potential temperatures, is shown in Figure 3.16b, where the dotted line is the initial as well as background potential temperature. The PBL height is 1250 m and can be identified from the minimum convective temperature and the well-mixed ensemble potential temperature. A well- mixed conservative scalar, e.g. potential temperature, is an important property of the convective boundary layer. Our climatological CBL carries this characteristic. With a homogenous and constant bottom heat flux of 0.05 K m s^{-1}, the major part of the CBL is warmed by about 0.7 K with a strong unstable layer near the surface. The warmed air penetrates into the background free atmosphere and mixes with it, leading to a convective cooling layer near the PBL top. Such entrainment process moves some free atmosphere air into the convective boundary layer and pushes the PBL height further upward.

The entrainment process is also demonstrated in the negative heat flux in Figure 3.17, where the total heat flux (solid line) is divided into convective scale (dotted line) and the parameterized small scale (dashed line) fluxes. The overall shape of total heat flux is nearly linear and decreases versus normalized height, where the minimum negative heat flux corresponds to the PBL top. At the surface, in absence of the resolved convective velocities due to the non-slip bottom boundary condition, the heat flux transport is completely contributed by the parameterized small scale motion, whose effect

decreases with height until a height of 0.5 z_i. Above that level, the small scale effect disappears and only the convective transport takes effect. The negative entrainment heat flux is contributed solely by explicitly resolved convective scale motion. The largest convective heat flux occurs at the height of 0.5 z_i. The minimum entrainment heat flux is about 2.5% of the forced surface heat flux.

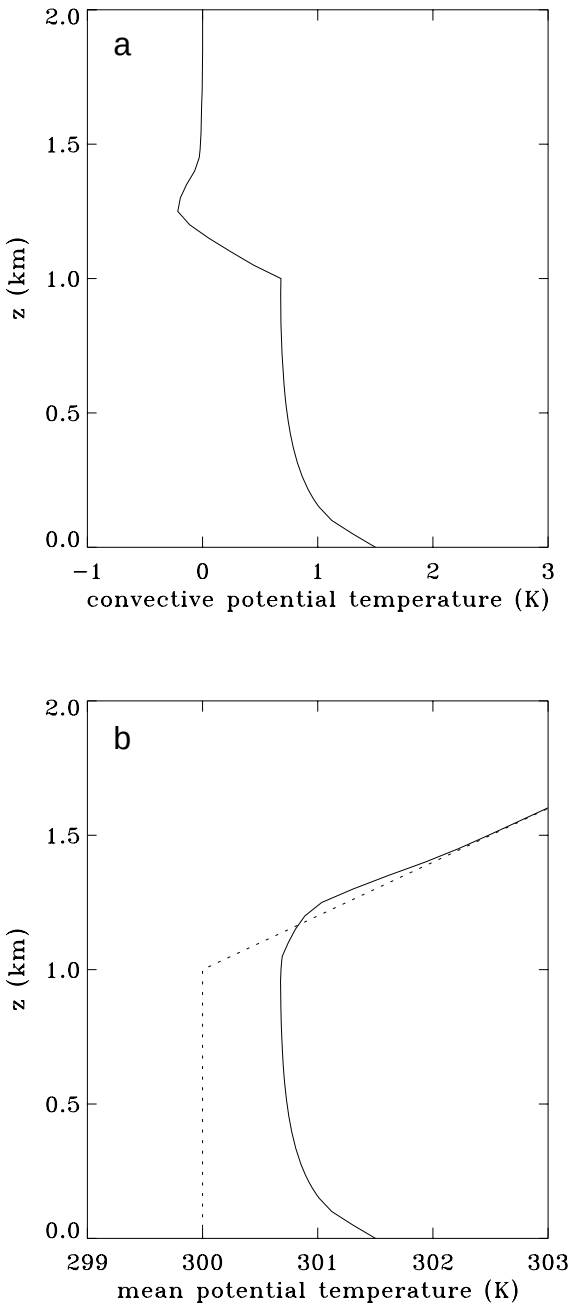

Figure 3.16 Vertical profiles of mean potential temperature for the 2-D climatological convective boundary layer for a) convective scale perturbation; b) ensemble mean state with initial profile as the dotted line in b (units: K).

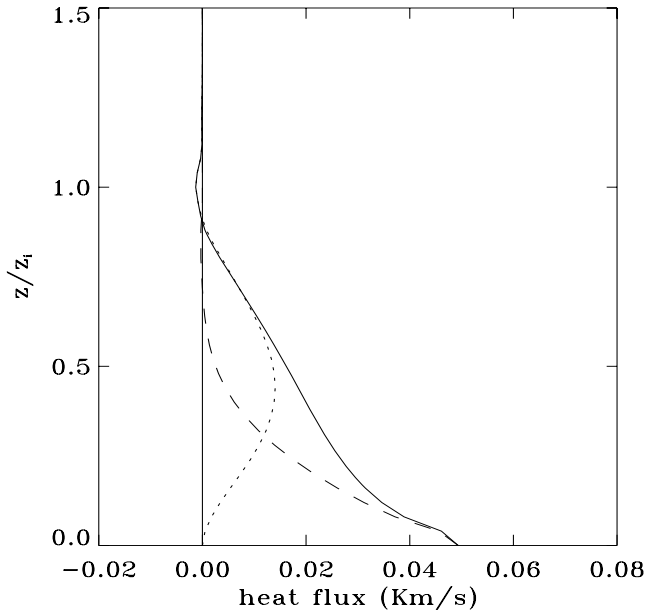

Figure 3.17 Vertical profiles of mean heat flux versus normalized height for the 2-D reference climatological convective boundary layer, where solid, dotted and dashed lines represent total, resolved scale and small scale respectively (units: K m/s), where z_i is the PBL height.

The statistics of higher–order moments statistics in velocity fields are shown for variance and vertical velocity skewness. As the horizontal averages of convective vertical and horizontal velocity components are zeros, the velocity variance is thus the same as the velocity fluctuation variance. Figure 3.18a shows the velocity variances versus normalized height. The w variance peaks at 0.5 z_i for about 0.015 m^2 s^{-2}, suggesting the largest magnitude of vertical velocity with opposite signs. It decreases symmetrically from that level. The u variance shows two nearly symmetrical bell shapes about 0.5 z_i. Two peaks of u variance indicate that a relative large magnitude of horizontal velocity occurs in the lower and upper parts of PBL simultaneously. The maximum values of u variance are close to that of w variance. The symmetrical profiles of velocity variance suggest our climatological convective boundary layer is well organized.

The vertical velocity skewness, $\overline{(w')^3}/[\overline{(w')^2}]^{3/2}$ (prime denotes the local deviation from the horizontal mean value), is a measure of asymmetry for the vertical velocity probability distribution function as it eliminates the compensation perturbation from the mean in the second order moments. If the distribution is symmetrical, the skewness is zero. If the right tail (larger value end) about the mean is more pronounced that the left tail (smaller value end), the distribution is positively skewed. It is generally agreed that typical CBL heated from below has positive values of skewness, reflecting the existence of strong but narrow updrafts and weak but broad downdrafts. However, discrepancies in the vertical profile remain between LES and observations. Observations suggest that skewness increases with height until 0.3 z_i then becomes relatively constant, whereas the LES shows a continuing increase of skewness with height with a peak near the PBL top [Lenschow et al., 1980; Wyngaard, 1988, Moeng and Rotunno, 1990]. Our

simulated skewness profile shows the positive value everywhere except its absence at the bottom boundary due to the no-slip condition. The skewness increases with height until about 0.4 z_i then becomes decrease relatively slow with height upwards. The difference between our model and LES may result from that each updraft penetrating into the free atmosphere above the inversion in our model simulation while only the few strongest updrafts do such in the LES. The maximum skewness is around 0.05, which is smaller than that predicted by LES by about an order of magnitude.

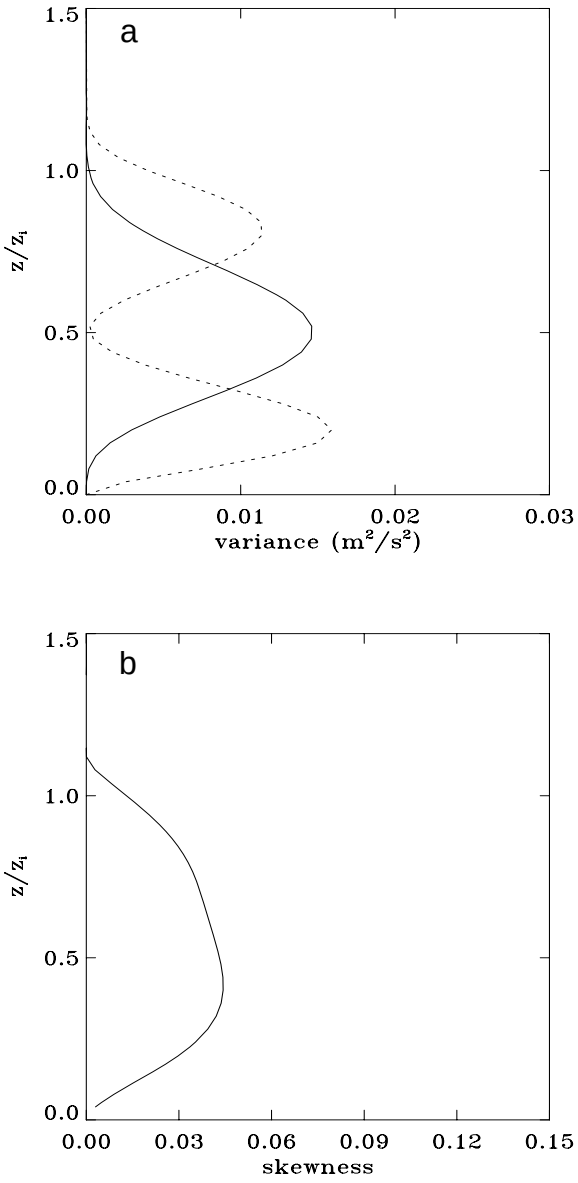

Figure 3.18 Vertical profiles of velocity moments statistics versus normalized height for the 2-D reference climatological convective boundary layer for a) velocity component variance ($\overline{u^2}$ as solid line and $\overline{w^2}$ as dotted-dashed line); b) vertical velocity skewness.

3.5.3 Sensitivity to External and Model Parameters

We have conducted sensitivity experiments for external parameters including surface heat flux H_s, cooling coefficient C_θ, and free atmosphere stratification $d\theta_0/dz$; as well as model parameters of eddy diffusivity K_m, K_h, and time step Δt. The results show a similar 2-D cellular spatial pattern and 1-D vertical profile shapes. Therefore, we will focus on their influences on PBL depth, mixed layer temperature increase, magnitudes of velocities and velocity variances. To facilitate comparison, the velocities and their variances are normalized by the convective vertical velocity scale.

Table 3.1 summarizes the simulation results for variations in the external parameters. The maximum downward velocities are generally 70-80% of the corresponding upward maximum. Decreasing the cooling coefficient C_θ increases the PBL depth, mixed layer temperature, normalized velocity fields and entrainment ratio because more added heat is utilized for the convection system but not dissipated to balance the background cooling. Increasing capping inversion strength decreases PBL depth and velocity fields because more energy is employed to overcome the stronger stable stratification, whereas it slightly increases the mixed layer temperature and entrainment flux consistently with LES analysis [Sorbjan, 1996]. As surface heat flux increases, PBL depth and velocity fields are enhanced by more vigorous convective motion; particularly, the normalized velocity magnitude is increased in a square root relationship. The mixed-layer temperature is also increased proportionally to surface heat flux increase.

As shown in Table 3.2, PBL depth and temperature field is not sensitive to a factor 2 change in eddy diffusivities. The magnitude of velocities and velocity variances

decrease with increasing eddy diffusivities because thermal diffusion will suppress the temperature fluctuation by causing the rising warm air to equilibrate with surrounding environment, destroying the buoyancy force. Varying time step leads to a slight change in PBL depth and temperature field but a large change in velocity fields. Increasing time step tenfold, the maxima of velocities and their variances are increased by about three to four times and an order of magnitude, respectively. Moreover, vertical velocity skewness maximum is also increased by an order. This might imply there exists relatively large numerical diffusion in our model. Such may be one possible reason for the smaller values of velocity fields from our simulations than those from LES discussed in Section 3.4. Therefore, our simulated spatial structure, profile shape and relative magnitude are more valuable at this point. Further studies needs to be performed before drawing conclusions regarding the velocity magnitude.

Table 3.1 Sensitivity experiments for the external parameters of surface heat flux H_s, cooling coefficient C_θ, and free atmosphere stratification $d\theta_0/dz$, where w_* is convective velocity scale. Bold characters refer to the reference simulation.

Forcings			Results						
H_s (K ms^{-1})	$d\theta_0/dz$ (10^{-3} K m^{-1})	C_θ (10^{-5} K s^{-1})	z_i (m)	$\overline{\theta}$ (K)	Max $\frac{\overline{w}}{w_*}$	Max $\frac{\overline{u}}{w_*}$	Max $\frac{\overline{w^2}}{w_*^2}$	Max $\frac{\overline{u^2}}{w_*^2}$	Entrainment ratio (%)
0.05	**5**	**4**	**1250**	**0.72**	**0.16/-0.12**	**±0.15**	**0.010**	**0.010**	**-3.4**
0.05	5	2	1320	1.05	0.18/-0.14	±0.17	0.012	0.012	-3.6
0.05	5	0	1440	1.72	0.23/-0.18	±0.20	0.018	0.017	-5.2
0.05	10	4	1170	0.75	0.15/-0.12	±0.14	0.008	0.010	-4.4
0.05	3	4	1350	0.68	0.18/-0.13	±0.16	0.011	0.011	-2.8
0.10	5	4	1400	1.35	0.22/-0.17	±0.21	0.016	0.016	-2.9
0.025	5	4	1160	0.36	0.11/-0.09	±0.11	0.005	0.006	-4.0

Table 3.2 Sensitivity experiments for the model parameters of eddy diffusivities K (including both K_m and K_h) and time step Δt. Bold characters refer to the reference simulation.

Parameter change	Results						
	z_i (m)	$\overline{\theta}$ (K)	Max $\frac{\overline{w}}{w_*}$	Max $\frac{\overline{u}}{w_*}$	Max $\frac{\overline{w^2}}{w_*^2}$	Max $\frac{\overline{u^2}}{w_*^2}$	Entrainment ratio (%)
Reference case	**1250**	**0.72**	**0.16/-0.12**	**±0.15**	**0.010**	**0.010**	**-3.4**
$2 \times K$	1230	0.71	0.10/-0.07	±0.10	0.003	0.004	-2.6
$0.5 \times K$	1260	0.69	0.17/-0.14	±0.17	0.012	0.012	-3.2
$10 \times \Delta t$	1290	0.74	0.76/-0.30	±0.50	0.104	0.111	-4.0
$5 \times \Delta t$	1260	0.74	0.44/-0.28	±0.34	0.058	0.058	-2.8

3.6 Summary and Conclusions

The motivation for constructing such a conceptual model for a climatological convective boundary layer was for its potential application in climate models. The maintenance of a nearly adiabatic "residual" layer at night over the depth to which the previous daytime convective boundary layer extended provides a climatological basis for the convective system over land. Improving understanding of the climate change and further the associated feedbacks invites the need to establish a climate equilibrium system over land. We refer to the 2-D coherent structures to describe the climatological role of convective circulation as a distinct and persistent component in climate models. In particular, turbulence is assumed to come from shear alone for a neutral condition and all the effects of unstable stratification is realized through the explicit convective eddies, which are resolved by fluid dynamics and thermal dynamics. The explicit convection and small scale turbulence are balanced by an imposed cooling effect from a large scale background field to achieve steady state solutions.

A semi-implicit second-order-accurate finite-difference method is applied on a non-staggered grid. Operator-splitting procedure reduces the differentiated Navier-Stokes and thermodynamic equations into a few separable elliptic equations at each time step, which can be solved by cyclic reduction. Because of the high nonlinearities and strong couplings inherent in the Navier-Stokes and thermodynamic equations, the development of numerical models has proven difficult. The numerical treatment is first successfully tested by an analytical solution to the 1-D heat diffusion equation. The model is then evaluated by large eddy simulations for a dry convective PBL case. The model reproduces some essential features of convective boundary layer, including a well-mixed

potential temperature profile below the PBL top; a linearly decreasing heat flux that becomes negative due to entrainment at the PBL top; relatively strong and narrow updrafts throughout the PBL depth; and characteristic eddy size on the order of PBL depth. The major difference lies in the different considerations for small scale effects. Our model parameterizes the small scale motion in terms of the explicit convective motion and thus it is likely non-turbulent. Such a treatment results in a better organized spatial distribution with coherent convective cells. Other differences include a smaller entrainment ratio, smaller magnitude of velocity fields and the corresponding variances, and a larger small scale heat transport in the lower part of PBL. Our vertical distribution of velocity variance compares better with the 2-D LES than the 3-D LES.

We present the results for a climatological convective boundary layer with a prescribed constant and homogenous surface heat flux and a specified cooling term representing the background large scale thermal balance. The coherent structure of 2-D convective cells is on the horizontal and vertical scales comparable with PBL height and is shown clearly in the spatial distributions of streamlines, vorticity and velocity fields. Such convective circulation changes its direction from cell to cell. The relatively intense updrafts correspond to the more concentrated streamlines and high vorticity contours. The maximum downward velocities are found to be 70-80% of the corresponding upward maximum. The convective vertical velocity is strongly correlated with the temperature field with updrafts corresponding to upwelling isothermal lines. The bulk properties of convective boundary layers remain; this includes vertical profiles of constant potential temperature and linearly decreasing heat fluxes. The negative entrainment heat flux is explicitly resolved by the convective-scale motion but it is relatively small. We also

discuss the vertical distribution of higher-order moments statistics for velocity variance and skewness. The model results are realistically sensitive to changes in surface heat flux, cooling coefficient, free atmosphere capping inversion and eddy diffusivity. Increasing surface heat flux increases the mixed-layer temperature proportionally and the normalized velocity magnitude in a square root relationship. Varying time step leads to a large change in the magnitude of velocity related fields, which needs further investigations. Although the model describes the conceptual physics for these elemental eddies, the next step must be establishing their dependence on various relevant boundary layer structure parameters and converting it into efficient computational algorithm for use in climate models.

CHAPTER 4

CONCLUSIONS

Despite the significant progress has been made for determining the magnitudes and understanding the mechanisms of aerosol radiative effects in recent decades, substantial uncertainties remain for characterizing direct effects and much larger for indirect effect [IPCC, 2001; Anderson et al., 2003a; Yu et al., 2006]. The overall objective of this thesis is to improve assessments on aerosol radiative effects and efforts are made for two specific aspects. One is to estimate aerosol direct radiative effect by taking advantage of advanced measurement data to provide a baseline for evaluating and constraining satellite retrievals and model simulations [Zhou et al., 2005; Yu et al., 2006]. The other is to develop a conceptual model to explicitly describe the distinct role of convective boundary layer on a climatological basis. Such model helps us to understand the fundamental basis of convective processes in response to aerosol radiative effects and to construct a dynamic circulation system of aerosol producing clouds in a climate models.

4.1 Research Review and Major Results

The first part of this thesis attempted to assess the aerosol direct radiative effects by utilizing advanced measurement data. The aerosol direct radiative effects are determined by a combination of aerosol properties (i.e. types), surface properties (i.e. albedo) and clouds. Significant improvements have recently been achieved in observational characterization of those determining factors. In particular, the ground-base aerosol network of AERONET has collected quality-assured aerosol optical properties for

up to the last 10 years and for distinct aerosol regimes over the world; MODIS, an advanced satellite sensor, is measuring aerosol optical depth, land surface albedo and cloud properties on a global scale.

The AERONET aerosol climatology is used, in conjunction with surface albedo and cloud products from MODIS, to calculate a climatology of aerosol direct radiative effect (ADRE) and its normalized form (NADRE) for distinct aerosol regimes. The NADRE is defined as the ADRE normalized by optical depth at 550 nm and is mainly determined by internal aerosol optical properties and geographical parameters. These terms are evaluated for cloud-free and cloudy conditions and for all-mode and fine-mode aerosols. Single-scattering albedo is an important variable determining ADRE of biomass burning. Because of stronger absorption by the smoke over South Africa, the average NADRE over South America is ~35% larger at the TOA but ~38% smaller at the surface than that over South Africa. The surface albedo is another important factor in determining ADRE, especially for mineral dust. As the surface albedo varies from ~0.1 to ~0.35, it is observed that the dust NADRE ranges from -44 to -17 $Wm^{-2}\tau^{-1}$ at the TOA and from -80 to -48 $Wm^{-2}\tau^{-1}$ at the surface over the Saharan deserts, Arabian Peninsula, and their surrounding oceans. We also find that the NADRE of fine-mode aerosol is larger at the TOA but smaller at the surface in comparison to that of all-mode aerosol because of its larger single-scattering albedo and smaller asymmetry factor. Cloudy-sky ADRE is usually not negligible for the observed cloud optical thickness but the TOA ADRE with clouds is sensitive to the relative location of aerosols and cloud layer.

MODIS-derived high-resolution land surface albedo is applied to study the clear-sky ADRE over North Africa and the Arabian Peninsula for summer 2001, where the

land surface is highly reflective with considerable spatial variability but poorly described by land models. In terms of the spatial resolution of surface albedos, 0.2˚ × 0.2˚ is sufficient to capture the spatial variability of ADREs and a 1˚ × 1˚ resolution is adequate for the regional mean ADREs. With MODIS surface albedo at 0.2˚ × 0.2˚ spatial resolution and integrated MODIS retrieved and GOGART simulated aerosol optical properties at 2.8˚ × 2.8˚ resolution, the TOA ADRE shows high spatial variability following that of surface albedo; however, the spatial resolution of surface and atmosphere ADREs are more controlled by that of aerosol optical properties. Regionally, the absorbing aerosols vertically redistribute solar energy from the surface (-22 Wm^{-2}) to the atmosphere (26 Wm^{-2}), and lead to a net warming at the TOA (4 Wm^{-2}). CLM-CCM3 modeled surface albedos can change positive TOA forcing (4 Wm^{-2}) based on MODIS albedos to negative (~ -2 Wm^{-2}), suggesting the need to realistically specifying land surface albedo in ADRE estimation.

The objective of the second part of this thesis is to develop a climatological convective boundary layer model as an initial step to potentially improve its parameterization in climate models. In existing climate models, standard concepts describe convection as transient 1-D structure but have been considered as at a "deadlock" [Randall et al., 2003]. Because of the maintenance of a nearly adiabatic "residual" layer at night over the depth to which the previous daytime convective boundary layer extended, the convective boundary layer over land exists on a climatological basis and should be describable as an average atmosphere condition. Improving understanding of the climate change and further the associated feedbacks invites the need to establish a climate equilibrium system over land [Betts, 2000]. Our

conceptual model explicitly describes the 2-D convective-scale motion in the framework of fluid dynamics and thermodynamics, and the small scale turbulence is parameterized for a neutral stratification. The emphasis of our approach is the climatological role of the coherent structure of convections described with simple multidimensional eddies and distinct from small scale turbulence.

The model reasonably reproduces some essential features of convective boundary layer from large eddy simulations and observations: a well-mixed potential temperature profile in the PBL; a linearly heat flux that decrease with height and becomes negative at the PBL top; relatively strong and narrow updrafts throughout the PBL depth; and characteristic eddy size on the order of PBL depth. The major difference is that our model produces better organized spatial distribution with coherent convective cells. It is such single convection cells that we hope can advance our understanding of convective boundary layer and improve its parameterization. Further investigations will be required to discuss the physical aspects of other differences such as relatively small entrainment ratio and magnitudes of velocity fields.

A climatological convective boundary layer is simulated for a prescribed constant and homogenous surface heat flux and a specified cooling term representing the background large scale thermal balance. The results show the 2-D coherent structure of convective cells with horizontal and vertical scales comparable with PBL height. The relatively intense and narrow rising motion corresponds to the more concentrated streamlines and high vorticity contours. It is observed that the maximum downward velocities are 70-80% of the accompanying upward maximum. The positive convective vertical velocity strongly correlates with the upwelling isothermal lines. There remain

some statistical properties of a well-mixed potential temperature profile and a nearly linear decreasing heat fluxes with height, where a small negative entrainment heat flux is explicitly resolved by the convective-scale motion. Sensitivity tests show nearly a proportional increase in the mixed-layer temperature and a square root increase in the normalized velocity magnitude with increasing surface heat flux.

4.2 Future Research

As presented in Chapter 2, the aerosol direct radiative effects represent the influences from both anthropogenic and natural components. Quantifying the aerosol radiative perturbation by anthropogenic aerosols is of primary concern for climate change research and requires distinguishing the anthropogenic portion from natural aerosols. In our study, the fine-mode fraction is used to estimate the anthropogenic aerosol direct forcing as suggested by Kaufman et al. [2002]. However, the AERONET-derived fine-mode aerosol properties may not well represent those of anthropogenic aerosols, because only one retrieved refractive index is assumed for particles of all sizes [Dubovik et al., 2000b]. Moreover, most fine-mode particles are not necessarily anthropogenic. Improved measurement capability on aerosol size distribution, absorption and chemical composition will be needed to determine anthropogenic contribution of aerosols.

The aerosol direct radiative effects under a cloudy sky are found not negligible for the observed cloud optical depths and sensitive to the relative vertical distribution of aerosol and cloud layer. Quantification of cloud impacts on aerosol direct radiative effects is limited by two major difficulties: 1) a lack of observational information on aerosol and cloud vertical profiles; 2) incapacity of passive satellite for measuring

aerosols in the presence of highly reflective clouds. Satellite-borne and surface-based lidar systems would provide a potential solution.

In Chapter 3, we develop a conceptual model for a climatoloigcal convective boundary layer. In comparison to large eddy simulations, several differences need to be addressed: a small entrainment ratio; small velocity magnitudes; and the relatively strong dependence of velocity magnitude on time step. Further studies could improve the physical understanding for those issues. Our numerical objective is to make the interaction of the modeled eddies with the mean flow as a function of large scale parameters – that is the essence of a parameterization. Thus, the next step must be establishing the model dependence on various relevant boundary layer structure parameters and converting it into efficient computational algorithm for use in a climate model. It is useful to describe what might be needed in general to implement a computational algorithm as a lookup table. Such a table gives the numbers needed to determine a required model parameter from other available model parameters. It would require a very large lookup table if it were simply related to model layer parameters through a numerical sampling procedure. However, boundary layer similarity theory can constrain and reduce the number of dimension that need be considered.

The parameterization proposed above can be extended to parameterization of cloud formation. However, the details of the latent heat generated buoyancy depend on the mechanics of the cloud-drop production. These can be initiated through a prescribed distribution of aerosol properties, but quantitative application within a climate model requires a dynamically more realistic representation of the circulation systems generating clouds [Nenes and Seinfeld 2003]. The boundary layers will formulate the dynamic

properties of clouds and this dynamical system can further be developed as a unified parameterization including boundary layer turbulence, shallow and deep cumulus convection.

REFERENCES

Ackerman, A.S., O.B. Toon, D.E. Stevens, A.J. Heymsfield, V. Ramanathan, and E.J. Welton, Reduction of tropical cloudiness by soot, *Science*, 288, 1042-1047, 2000.

Albrecht, B.A., Aerosols, cloud microphysics, and fractional cloudiness, *Science*, 245, 1227-1230, 1989.

Anderson, T.L., R.J. Charlson, S.E. Schwartz, R. Knutti, O. Boucher, H. Rodhe and J. Heintzenberg, Climate forcing by aerosols - A hazy picture, *Science*, 300, 1103-1104, 2003a.

Anderson, T L., R.J. Charlson,, D.M. Winker, J.A. Ogren, and K. Holmén, Mesoscale variations of tropospheric aerosols, *J. Atmos. Sci.*, 60, 119-136, 2003b.

Anderson, T.L., et al., An "A-Train" strategy for quantifying direct aerosol forcing of climate, *Bull. Am. Met. Soc.*, 86(12), 1795-1809, 2005.

Arakawa, A., and W.H. Schubert, The interaction of a cumulus cloud ensemble with the large-scale environment, Part I, *J. Atmos. Sci.*, 31, 674-701, 1974.

Betts, A.K., Idealized model for equilibrium boundary layer over land, *J. Hydromet.*, 1, 507-523, 2000.

Blackador, A.K., High Resolution models of the planetary boundary layer, *Adv. Environ. Sci. Eng.*, J. Pfafflin and E. Ziegler, Eds., 1, Gordon and Breach, 50-85, 1979.

Bohren, C.F., and D.R. Huffman, *Absorption and Scattering of Light by Small Particles*, John Wiley, Hoboken, N.J., 1983.

Boucher, O., et al., Intercomparison of models representing direct short-wave radiative forcing by sulfate aerosols, *J. Geophys. Res.*, 103, 16979-16998, 1998.

Boucher, O., On aerosol direct shortwave forcing and Henyey-Greenstein phase function, *J. Atmos. Sci.*,55, 128-134, 1998.

Boucher, O., and D. Tanre, Estimation of the aerosol perturbation to the Earth's radiative budget over oceans using POLDER satellite aerosol retrievals, *Geophys. Res. Lett.*, 27, 1103-1106, 2000.

Caughey, S., and S. Palmer, Some aspects of turbulence structure through the depth of the convective boundary layer, *Q. J. R.. Meteorol. Soc.*, 105, 811–827, 1979.

Chameides, W.L., et al., A case study of the effects of atmospheric aerosols and regional haze on agriculture: An opportunity to enhance crop yields in China through emission controls? *Proc. Natl. Acad. Sci.*, 96, 13,626-13,633, 1999.

Charlson, R.J., and M.J. Pilat, Climate: The influence of aerosols, *J. Appl. Meteorol.*, 8, 1001-1002, 1969.

Charlson, R.J., S.E. Schwartz, J.M. Hales, R.D. Cess, J.A. Coakley, J.E. Hansen, and D.J. Hofmann, Climate forcing by anthropogenic aerosols, *Science*, 255, 423-430, 1992.

Cheinet, S., A multiple mass-flux parameterization for the surface-generated convection, Part I: Dry plumes, *J. Atmos. Sci.*, 60(18), 2313-2327, 2003

Chiam, K.-H., M.-C. Lai, and H.S. Greenside, Efficient algorithm on a nonstaggered mesh for simulating Rayleigh-Bénard convection in a box, *Phys. Rev. – E*, 68, 026705, 2003.

Chin, M., et al., Tropospheric aerosol optical thickness from the GOCART model and comparisons with satellite and Sun photometer measurements, *J. Atmos. Sci.*, 59, 461-483, 2002.

Chou, M.–D., P.–K. Chan, and M. Wang, Aerosol radiative forcing derived from SeaWiFS-retrieved aerosol optical properties, *J. Atmos. Sci.*, 59, 748-757, 2002.

Chu, D. A., Kaufman, Y. J., Ichoku, C., Remer, L. A., Tanré, D., and Holben, B., Validation of MODIS aerosol optical depth retrieval over land, *Geophys. Res. Lett.*, 29(12), doi:10.1029/2001/GL013205, 2002.

Coakley, J.A., R.D. Cess, and F.B. Yurevich, The effect of tropospheric aerosols on the Earth's radiation budget: a parameterization for climate models, *J. Atmos. Sci.*, 40, 116-138, 1983.

Collins, W.D., et al., Simulation of aerosol distributions and radiative forcing for INDOEX: Regional climate impacts, *J. Geophys. Res.*, 107, 8028, doi:10.1029/ 2000JD000032, 2002.

Crum, T.D., R.B. Stull, and E.W. Eloranta, Coincident Lidar and aircraft observations of entrainment into thermals and mixed layers, *J. Clim. Appl. Met.*, 26, 774-778, 1987.

Cuijpers J.W.M., and P.G. Duynkerke, Large-eddy simulation of trade-wind cumulus clouds, *J. Atmos. Sci.*, 50 (23): 3894-3908, 1993.

Deardorff, J.W., Numerical investigation of neutral and unstable planetary boundary layers, *J. Atmos. Sci.*, 29, 91-115, 1972.

Deardorff, J.W., Stratocumulus-capped mixed layers derived from a three-dimensional model, *Bound.-Layer Meteor.*, 18, 495–527, 1980.

Dickinson, R.E., Land surface processes and climate-surface albedos and energy balance, *Adv. Geophys.*, 25, 305-353, 1983.

Dickinson, R.E., A. Henderson-Seller, and P.J. Kennedy, Biosphere-Atmosphere Transfer Scheme (BATS) version 1e as Coupled to the NCAR Community Model, Tech. Note NCAR/TN-387+STR, 72pp., *Natl. Cent. of Atmos. Res.*, Boulder, Colo., 1993.

Dormy, E., An accurate compact treatment of pressure for collocated variables, *J. Comput. Phys.*, 151(2), 676-683, 1999.

Dubovik, O. and M.D. King, A flexible inversion algorithm for retrieval of aerosol optical properties from Sun and sky radiance measurements, *J. Geophys. Res.*, 105, 20,673-20,696, 2000a.

Dubovik, O., et al., Accuracy assessments of aerosol optical properties retrieved from AERONET Sun and sky-radiance measurement, *J. Geophys. Res.*, 105, 9791-9806, 2000b.

Dubovik, O., et al., Variability of absorption and optical properties of key aerosol types observed in worldwide locations, *J. Atmos. Sci.*, 59, 590-608, 2002.

Eck, T.F., et al., High aerosol optical depth biomass burning events: A comparison of optical properties for different source regions, *Geophys. Res. Lett.*, 30, 2035, doi: 10.1029/2003GL017861, 2003.

Ferziger, J.H., and M. Peric, *Computational methods for fluid dynamics*, Springer-Verlag, New York, 356pp., 1996.

Fu, Q., and K.N. Liou, On the correlated k-distribution method for radiative transfer in nonhomogenous atmospheres, *J. Atmos. Sci.*, 49, 2139-2156, 1992.

Fu, Q., and K.N. Liou, Parameterization of the radiative properties of cirrus clouds, *J. Atmos. Sci.*, 50, 2008-2025, 1993.

Garratt, J.R., *The atmospheric boundary layer*, Cambridge University Press, New York, 316pp., 1992.

Giorgi, G., X. Q. Bi and Y. Qian, Direct radiative forcing and regional climatic effects of anthropogenic aerosols over East Asia: a regional coupled climate-chemistry/aerosol model study, *J. Geophys. Res.*, 107, 4439, doi:10.1029/2001JD001066, 2002.

Grabowski, W.W., X. Wu, and M.W. Moncrieff, Cloud-resolving modeling of tropical cloud systems during phase III of GATE Part I: Twodimensional experiments, *J. Atmos. Sci.*, 53, 3684–3709, 1996.

Hansen, J., M. Sato, and R. Ruedy, Radiative forcing and climate response, *J. Geophys. Res.*, 102, 6831-6864, 1997.

Harlow, F.H., and J.E. Welch, Numerical calculation of time-dependent viscous incompressible flow of fluid with free surface, *Phys. Fluids*, 8(12), 2182, 1965.

Haywood, J.M., and K.P. Shine, The effect of anthropogenic sulfate and soot on the clear-sky planetary radiation budget, *Geophys. Res. Lett.*, 22, 603-606, 1995.

Haywood, J.M., and K.P. Shine, Multi-spectral calculations of the radiative forcing of tropospheric sulfate and soot aerosols using a column model, *Q. J. R.. Meteorol. Soc.*, \123, 1907-1930, 1997.

Haywood, J., and O. Boucher, Estimates of the direct and indirect radiative forcing due to tropospheric aerosols: A review, *Rev. Geophys.*, 38, 513-543, 2000.

Hess, M., et al., Optical properties of aerosols and clouds: The software package OPAC, *Bull. Am. Met. Soc.*, 79, 831-844, 1998.

Holben B.N., et al., AERONET - A federated instrument network and data archive for aerosol characterization, *Rem. Sens. Environ.*, 66, 1-16, 1998.

Holben, B.N., et al., An emerging ground-based aerosol climatology: Aerosol Optical Depth from AERONET, *J. Geophys. Res.*, 106, 12,067-12,097, 2001

Holtslag, A.A.M., and C.-H. Moeng, Eddy diffusivity and countergradient transport in the convective atmospheric boundary layer, *J. Atmos. Sci.*, 48, 1690-1698, 1991.

Holtslag, A.A.M., and B.A. Boville, Local versus nonlocal boundary-layer diffusion in a global climate model, *J. Clim.*, 6, 1825-1842, 1993.

Huang Y., W. L. Chameides and R. E. Dickinson, 2006: The assessment of direct and indirect effect of anthropogenic aerosols on regional precipitation over East Asia, *J. Geophys. Res.*, revised, 2006.

Incropera, F.P., and D.P. DeWitt, *Fundamentals of Heat and Mass Transfer*, 5th Edition, John Wiley and Sons, New York, NY, 981pp, 2002.

Intergovernmental Panel on Climate Change (IPCC), Radiative forcing of climate change, in *Climate Change 2001*, Cambridge Univ. Press, New York, 2001.

Jin, Z., T.P. Charlock, and K. Rutledge, Analysis of broadband solar radiation and albedo over the ocean surface at COVE, *J. Atmos. Oceanic. Technol.*, 19, 1585-1601, 2002.

Jin, Z., et al., A parameterization of ocean surface albedo, *Geophys. Res. Lett.*, 31, L22301, doi:10.1029/2004GL021180, 2004.

Kaufman, Y.J., D. Tanre, L.A. Remer, E.F. Vermote, A. Chu, and B.N. Holben, Operational remote sensing of tropospheric aerosol over land from EOS moderate resolution imaging spectroradiometer, *J. Geophys. Res.*, 102, 17051-17067, 1997.

Kaufman, Y.J., D. Tanre, and O. Boucher, A satellite view of aerosols in the climate system, *Nature*, 419, 215-223, 2002.

Keil, A., and J.M. Haywood, Solar radiative forcing by biomass burning aerosol particles during SAFARI 2000: A case study based on measured aerosol and cloud properties, *J. Geophys. Res.*, 108(D13), 8467, doi:10.1029/2002JD002315, 2003.

King, M.D., et al., Cloud and aerosol properties, precipitable water and profiles of temperature and water vapor from MODIS, IEEE Trans. *Geosci .Remote Sens.*, 41, 442-458, 2003.

Kinne, S., and R. Pueschel, Aerosol radiative forcing for Asian continental outflow, *Atmos. Environ.*, 35, 5019-5028, 2001.

Klemp, J.B., and D.R. Durran, An upper boundary condition permitting internal wave radiation in numerical mesoscale models, *Mon. Wea. Rev.*, 111, 430-444, 1983.

Koepke, P., M. Hess, I. Schult, and E.P. Shettle, *Global aerosol data set*. MPI Meteopologie Hamburg Rep. 243, 44pp, 1997.

Koren, I.Y., Y.J. Kaufman, L.A. Remer, and J.V. Martins, Measurement of the effect of Amazon smoke on inhibition of cloud formation, *Science*, 303, 1342, 2004.

Krueger, S.K., Numerical simulation of tropical cumulus clouds and their interaction with the subcloud layer, *J. Atmos. Sci.*, 45, 2221–2250, 1988.

Lappen, C-L., and D.A. Randall, Toward a unified parameterization of the boundary layer and moist convection. Part I: A new type of mass-flux model. *J. Atmos. Sci.*, 58(15), 2021-2036, 2001.

Lenschow, D., and P. Stephens, The role of thermals in the convective boundary layer, *Bound.-Layer Meteor.*, 19, 509–532, 1980.

Li, F., A. M. Vogelmann and V. Ramanathan, Dust aerosol radiative forcing measured from space over the Western Africa, *J. Clim.*, 17(13), 2558-2571, 2004.

Liao, H., and J.H. Seinfeld, Effect of clouds on direct aerosol radiative forcing of climate, *J. Geophys. Res.*, 103, 3781-3788, 1998.

Lorenz, E.N., Deterministic non-periodic flow, *J. Atmos. Sci.*, 20, 130-141, 1963.

Lucht, W., A.H. Hyman, A.H. Strahler, M.J. Barnsley, P. Hobson, and J.-P. Muller, A comparison of satellite-derived spectral albedos to groundbased broadband albedo measurements modeled to satellite spatial scale for a semi-desert landscape, *Remote Sens. Environ.*, 74, 85–98, 2000.

Mace, G.C., Y.Y. Zhang, S. Platnick, M.D. King, P. Minnis and P. Yang, Evaluation of cirrus cloud properties derived from MODIS data using cloud properties derived from ground-based observations collected at the ARM SGP site, *J. Appl. Meteorol.*, 44, 221-240, 2005.

Mahowald N.M. and C. Luo, A less dusty future, *Geophys. Res. Lett.*, 30(17), 1903, 2003.

Markowicz, K.M., P.J. Flatau, R.V. Ramana, P.J. Crutzen, and V. Ramanathan, Absorbing mediterranean aerosols lead to a large reduction in the solar radiation at the surface, *Geophys. Res. Lett.*, 29, 1968, doi:10.1029/2002GL015767, 2002.

Martonchik, J. V., D. J. Diner, K. A. Crean, and M. A. Bull, Regional aerosol retrieval results from MISR, IEEE Trans, *Geosci. Remote Sens.*, 40, 1520-1531, 2002.

Martins, J. V., D. Tanré, L.A. Remer, Y. J. Kaufman, S. Mattoo, R. Levy, MODIS Cloud screening for remote sensing of aerosol over oceans using spatial variability, *Geophys. Res. Lett.*, 29(12),10.1029/2001GL013252, 2002.

Mason, P. J., Large eddy simulation of the convective atmospheric boundary layer, *J. Atmos. Sci.*, 46, 1492–1516, 1989.

McClatchey, R.A., et al., Optical properties of the atmosphere 3rd ed., Rep. *AFCRL-72-0497*, Air Force Cambridge Res. Lab., Hanscom Air Force Base, 1972.

McCormick, R.A., and J.H. Ludwig, Climate modification by atmospheric aerosols, *Science*, 156(3780), 1358-1359, 1967.

Mellor, G.L., and T. Yamada, A hierarchy of turbulence closure models for planetary boundary layers, *J. Atmos. Sci.*, 31, 1791-1806, 1974.

Menon, S., A. D. Del Genio, D. Koch and G. Tselioudis, GCM simulations of the aerosol indirect effect: Sensitivity to cloud parameterization and aerosol burden, *J. Atmos. Sci.*, 59, 692-713, 2002.

Moeng, C.-H., A large-eddy-simulation for the study of planetary boundary layer turbulence, *J. Atmos. Sci.*, 41, 2052–2062, 1984.

Moeng, C.-H., and R. Rotunno, Vertical-velocity skewness in the buoyancy-driven boundary layer, *J. Atmos. Sci.*, 47, 1149-1162, 1990.

Moeng, C.-H., and P.P. Sullivan, Large eddy simulation, Encyclopedia of Atmospheric Sciences, *J. Holton, J. Pyle, and J. Curry, Eds.*, Academic Press, 1140–1150, 2002.

Moeng, C.-H., J.C. McWilliams, R. Rotunno and P.P. Sullivan, Investigation 2D modeling of atmospheric convection in the PBL, *J. Atmos. Sci.*, 61, 889–903, 2004.

Monin, A.S., and A.M. Obukhov, Basic laws of turbulent mixing in the ground layer of the atmosphere (in Russian), *Tr. Geofiz. Inst. Akad. Nauk.* SSSR, 151, 163-187, 1954.

Nemesure, S., R. Wagener, and S. E. Schwartz, Direct shortwave forcing of climate by anthropogenic sulphate aerosol: Sensitivity to particle size, composition, and relative humidity, *J. Geophys. Res.*, 100, 26,105-26,116, 1995.

Nenes, A., and J.H. Seinfeld, A new parameterization of aerosol activation appropriate for climate models, *J. Geophys. Res.*, 108 (D7), 4415, doi:10.1029/2002JD002911, 2003.

Nieuwstadt, F. T. M., P. J. Mason, C.-H. Moeng, and U. Schumann, Large-eddy simulation of the convective boundary layer: A comparison of four computer codes, *Turbulent Shear Flows 8*, F. Durst et al., Eds., Springer-Verlag, 343–367, 1993.

Oleson, K.W., G.B. Bonan, C. Schaaf, F. Gao, Y.F. Jin and A. Strahler, Assessment of global climate model and land surface albedo using MODIS data, *Geophys. Res. Lett.*, 30(8), 1443, 2003.

Pinty, B., F. Roveda, M. M. Verstraete, N. Gobron, Y. Govaerts, J. V. Martonchik, D. J. Diner, and R. A. Kahn, Surface albedo retrieval from Meteosat-2. Applications, *J. Geophys. Res.*, 105, 18,099– 18,112, 2000.

Platnick, S., et al., The MODIS cloud products: Algorithms and examples from Terra, IEEE Trans. *Geosci.Remote Sens*., 41, 459-473, 2003.

Quartapelle, L.: *Numerical solution of the incompressible Navier-Stokes equations*, Berlin: Birkhauser, 1983.

Ramanathan, V., P.J. Crutzen, J.T. Kiehl, and D. Rosenfeld, Aerosols, climate, and the hydrological cycle, *Science*, 294, 2119-2124, 2001.

Randall, D. A., M. Khairoutdinov, A. Arakawa, and W. W. Grabowski, Breaking the cloud parameterization deadlock, *Bull. Amer. Meteor. Soc.*, 84, 1547–1564, 2003.

Remer, L.A., Y.J. Kaufman, D. Tanre, S. Mattoo, D.A. Chu, J.V. Martins, R.-R. Li, C. Ichoku, R.C. Levy, R.G. Kleidman, T.F. Eck, E. Vermote, and B.N. Holben, The MODIS aerosol algorithm, products and validation, *J. Atmos. Sci.*, 62(4), 947-973, 2005.

Renno , N.O., P.H. Stone, and K.A. Emanuel, Radiative-convective model wit h an explicit hydrological cycle 2. Sensitivity to large changes in solar forcing, *J. Geophys. Res.*, 99(D8), 17 001-17 020, 1994.

Renno , N.O. and A.P. Ingersoll, Natural convection as a heat engine: a theory for CAPE, *J. Atmos. Sci.*, 53(4), 572-585, 1996.

Rosenfeld, D., and I.M. Lensky, Satellite-based insights into precipitation formation processes in continental and maritime convective clouds, *Bull. Am. Met. Soc.*, 79, 2457-2476, 1998.

Schaaf C.B., et al., First operational BRDF, albedo and nadir reflectance products from MODIS, *Remote Sens. Environ.*, 83, 135-148, 2002.

Schmidt, H., and U. Schumann, Coherent structure of the convective boundary layer derived from large-eddy simulation, *J. Fluid Mech.*, 200, 511–562, 1989.

Schumann, U., and C.-H. Moeng, Plume fluxes in clear and cloudy convective boundary layers, *J. Atmos. Sci.*, 48, 1746-1757, 1991.

Sellers, P.J., S.O. Los, C.J. Tucker, C.O. Justice, D.A. Dazlich, C.J. Collatz and D.A. Randall, A revised land surface parameterization (SiB2) for atmospheric GCMs, Part II, The generation of global fields of terrestrial biospheric parameters from satellite data, *J. Clim.*, 9, 706-737, 1996.

Smirnov A., B.N. Holben, T.F. Eck, O. Dubovik, and I. Slutsker, Cloud screening and quality control algorithms for the AERONET database, *Rem. Sens. Env.*, 73, 337-349, 2000.

Sokolik, I.N., O.B. Toon, and R.W. Bergstrom, Modeling the radiative characteristics of airborne mineral aerosols at infrared wavelengths, *J. Geophys. Res.*, 103 (D8), 8813-8826, 1998.

Sorbjan,Z., *Structure of the Atmospheric Boundary layer*, Prentice Hall, Englewood Cliffs, N. J., 317pp., 1989.

Sorbjan, Z., Effects caused by varying the strength of the capping inversion based on a large eddy simulation model of the shearfree convective boundary layer, *J. Atmos. Sci.*, 53, 2015–2024, 1996.

Stevens, B., Entrainment in stratocumulus-topped mixed layers. *Q. J. R.. Meteorol. Soc.*, 128, 2663-2690, doi:10.1256/qj.01.202, 2002.

Strugnell, N. C., W. Lucht, and C. Schaaf, A global albedo data set derived from AVHRR data for use in climate simulations, *Geophys. Res. Lett.*, 28(1), 191–194, 2001.

Swarztrauber, P.N., and R.A. Sweet, Direct solution of discrete Poisson equation on a disk, *SIAM (Soc. Ind. Appl. Math.) J. Numer. Anal.*, 10(5), 900-907, 1973. 1973.

Swarztrauber, P.N., R.A. Sweet and J.C. Adams, Fishpack: Efficient FORTRAN subprograms for the solution of elliptic partial differential equations, *NCAR*, http://www.cisl.ucar.edu/css/software/fishpack/technote.ps, unpublished.

Taconet O., and A. Weill, Convective plumes in the atmospheric boundary layer as observed with an acoustic Doppler sodar, *Bound.-Layer Meteor.*, 25, 143-158, 1983.

Takemura, T., T. Nozawa, S. Emori, T. Y. Nakajima, and T. Nakajima, Simulation of climate response to aerosol direct and indirect effects with aerosol transport-radiation model, J. *Geophys. Res.*, 110, D02202, doi:10.1029/2004JD005029, 2005.

Tanré, D., J. Haywood, J. Pelon, J. F. Léon, B. Chatenet, P. Formenti, P. Francis, P. Goloub, E. J. Highwood, and G. Myhre, Measurement and modeling of the Saharan dust radiative impact: Overview of the Saharan Dust Experiment (SHADE). *J. Geophys. Res.*, Vol. 108, No. D18, 8574, doi:10.1029/2002JD003273, 2003.

Tegen I. and I. Fung, Contribution to the atmospheric mineral aerosol load from land-surface modification, *J. Geophys. Res.*, 100(D9), 18,707-18,726, 1995.

Troen, I., and L. Mahrt, A simple model of the atmospheric boundary layer: sensitivity to surface evaporation, *Bound.-Layer Meteor.*, 37, 129-148, 1986.

Tsvetsinskaya, E.A., et al., Relating MODIS-derived surface albedo to soils and rock types over Northern Africa and the Arabian peninsula, *Geophys. Res. Lett.*, 29, 2002.

Twomey, S., The influence of pollution on the shortwave albedo of clouds, *J. Atmos. Sci.*, 34, 1149-1152, 1977.

Vermote, E.F., N.E. El Saleous, and C.O. Justice, Atmospheric correction of MODIS data in the visible to middle infrared: first results, *Rem. Sens. Env.*, 83, 97-111, 2002.

Wang, C., and J.-G. Liu, Analysis of finite difference schemes for unsteady Navier-Stokes equations in vorticity formulation, *Numer. Math.*, 91(3), 543-576; doi10.1007/ s002110100311, 2002.

Wang, S., and B. Albrecht, A mean gradient of the convective boundary-layer, *J. Atmos. Sci.*, 47, 126-138, 1990.

Wang, Z., M. Barlage, X. Zeng, R. E. Dickinson, and C. B. Schaaf, The solar zenith angle dependence of desert albedo, *Geophys. Res. Lett.*, 32, L05403, doi:10.1029/ 2004GL021835, 2005.

Webb, E.K., Convection mechanisms of atmospheric heat transfer from surface to global scales, *Proc. Second Australasian Conf. on Heat and Mass Transfer*, Sydney, 523-539, 1977.

Williams, A., and J. Hacker, Interactions between coherent eddies in the lower convective boundary layer, *Bound.-Layer Meteor.*, 64, 55–74, 1993.

Willis, G. E., and J. W. Deardorff, A laboratory model of the unstable planetary boundary layer, *J. Atmos. Sci*., 31, 1297–1307, 1974.

Willis, G. E., and J. W. Deardorff, Laboratory observations of turbulent penetrative-convection planforms. *J. Geophys. Res.*, 84, 295–302, 1979.

Wyngaard, J.C., Structure of the PBL, Lectures on Air Pollution Modeling, A. Venkatram and J.C. Wyngaard, Eds., *Americ. Meteor. Soc.*, Boston, pp 385, 1988.

Wyngaard, J. C., Atmospheric turbulence, *Annu. Rev. Fluid Mech.*, 24, 205–233, 1992.

Xu, J., M.H. Bergin, R. Greenwald, and P.B. Russell, Direct aerosol radiative forcing in the Yangtze delta region of China: Observation and model estimation, *J. Geophys. Res.*, 108(D2), 4060, doi: 10.1029/2002JD002550, 2003.

Xu, K.-M., and D.A. Randall, Explicit simulation of cumulus ensembles with the GATE phase III data: Comparison with observations, *J. Atmos. Sci.*, 53, 3710–3736, 1996.

Yu, H., S.C. Liu, and R.E. Dickinson, Radiative effects of aerosols on the evolution of the atmospheric boundary layer, *J. Geophys. Res.*, 107, 4142, 2002.

Yu, H., R.E. Dickinson, M. Chin, Y.J. Kaufman, B.N. Holben, I.V. Geogdzhayev, and M.I. Mishchenko, Annual cycle of global distributions of aerosol optical depth from integration of MODIS retrievals and GOCART model simulations, *J. Geophys. Res.*, 108, 4128, 2003.

Yu, H., R.E. Dickinson, M. Chin, Y.J. Kaufman, M. Zhou, L. Zhou, Y. Tian, O. Dubovik, and B.N. Holben, Direct radiative effect of aerosols as determined from a combination of MODIS retrievals and GOCART simulations, *J. Geophys. Res.*, 109, D03206, doi:10.1029/2003JD003914, 2004.

Yu, H., et al., A review of measurement-based assessment of aerosol direct radiative effect and forcing, *Atmos. Chem . Phys.*, 6, 613-666, 2006.

Zhang, D.-L., and R.A. Anthes, A high-resolution model of the planetary boundary layer – Sensitivity tests and comparisons with SESAME-79 data. *J. Appl. Meteor.*, 21, 1594-1609, 1982.

Zhang, J., S.A. Christopher, L.A. Remer, and Y.J. Kaufman, Shortwave aerosol radiative forcing over cloud-free oceans from Terra. II: Seasonal and global distributions, *J. Geophys. Res.*, 110, D10S24, doi:10.1029/2004JD005009, 2005.

Zhou, L., et al., Comparisons of seasonal and spatial variations of albedos from MODIS and Common Land Model, Res., *J. Geophys. Res.*, 108(D15), 4488, doi:10.1029/ 2002JD003326, 2003.

Zhou, M., H. Yu, R.E. Dickinson, O. Dubovik, B.N. Holben, A normalized description of the direct effect of key aerosol types on solar radiation as estimated from AERONET aerosols and MODIS albedos, *J. Geophys. Res.*, 110, D19202, doi:10.1029/ 2005JD005909, 2005.